Title
Transient-Liquid-Phase (TLP) Bonding of Al2O3 Using Nb-based Multilayer Interlayers

Author
Hong, Sung Moo

Publication Date
2009

Peer reviewed|Thesis/dissertation

Transient-Liquid-Phase (TLP) Bonding of Al_2O_3 Using Nb-based Multilayer Interlayers

by

Sung Moo Hong

A dissertation submitted in partial satisfaction of the

Requirements for the degree of

Doctor of Philosophy

in

Engineering-Materials Science and Engineering

in the

Graduate Division

of the

University of California, Berkeley

Committee in charge:

Professor Andreas M. Glaeser, Chair
Professor Ronald Gronsky
Professor Ivo Souza

Fall 2009

Transient-Liquid-Phase (TLP) Bonding of Al_2O_3 Using Nb-based Multilayer Interlayers

by Sung Moo Hong

Abstract

Transient-Liquid-Phase (TLP) Bonding of Al_2O_3
Using Nb-based Multilayer Interlayers

by

Sung Moo Hong
Doctoral of Philosophy in Engineering, Materials Science and Engineering

University of California, Berkeley

Professor Andreas M. Glaeser, Chair

Transient-liquid-phase (TLP) bonding was used to join high-strength, high-purity Al_2O_3 ceramic. This method uses a multilayer interlayer (B/A/B sandwich structure), which forms thin transient-liquid layers between the Al_2O_3 and the refractory core layer (A), then isothermally solidifies through a diffusive mechanism. The presence of thin liquid layers allow interfacial gaps and voids to be filled, while allowing bonding times comparable to those used for conventional brazing. It was shown that TLP bonding produces high-strength joints with re-melt temperatures that are significantly higher than the bonding temperatures used. This study explores the interrelationships between the processing conditions, fracture strengths of the joints, wetting behavior of the TLP, and the diffusion/isothermal solidification kinetics. In particular, when Ni/Nb/Ni interlayers were utilized, four-point bend tests revealed that the fracture strengths of the joints matched those of the monolithic Al_2O_3, even after a 5-min holding time at 1400°C, the bonding temperature. The resulting interlayer consists of >99% Nb, which has a melting point >2000°C. Sessile-drop wetting experiments revealed that the Ni-Nb liquid alloy formed during bonding exhibits relatively low contact angles (≈90°) on Al_2O_3, which enables the formation of nearly flaw-free interfaces. An analytical diffusion calculation model was also used to describe the isothermal-solidification and homogenization kinetics, and will be used in future studies to aid new interlayer designs.

To my family.

Contents

List of Figures

Chapter 4

Acknowledgements

I would like to take this opportunity to thank my parents and my family, who have gone through so much to support me over the years. I would also like to thank my advisor, Professor Glaeser, from whom I've learned so much and I am truly grateful for the opportunity to have worked for him. I have also had the support and love from many great friends – really too many of you to name. I do want to especially thank my two best friends Elim and Michelle for being there for me all these years.

I also cannot thank everyone in our research group enough for being great friends and co-workers. Josh and Joe were great mentors – I've learned so much from them, and Chris and Tom have been fantastic to work with. Thank you to the rest of the group, Mark, Mary, Melissa, Robert, and Karen, for all your support.

1. Introduction

Nearly all engineered structures and devices are assembled by joining an array of parts with various shapes, dimensions, and material types. Each part is designed to perform specific tasks and must be joined to other components effectively for the entire assembly to function properly. Although a wide range of materials has been joined to fabricate numerous structures and devices since the Stone Age, when some of the earliest man-made tools were created, most failures still occur along joints. There are several well-established joining methods currently available but, some materials, such as high-temperature structural ceramics, are very difficult to join using these conventional methods. In this study, a novel joining process using a multilayer interlayer is applied to produce strong, reliable Al_2O_3-Al_2O_3 joints, and the relationships among processing conditions, mechanical, and thermal properties of the joints are studied.

Regardless of the joining method and the processing conditions used, there is a set of common desired joint properties. It is highly desirable to produce a bond that does not contain any interfacial flaws or voids, which function as crack-initiation sites leading to a decrease in the bond strength. An ideal joint would not have any residual stresses due to thermal-expansion-coefficient mismatch between the joined constituents. When joining brittle materials, such as ceramics, large tensile stresses due to thermal-expansion-coefficient mismatch may result in the premature failure of the joint. The parts being joined must also be chemically compatible with each other to avoid the formation of any secondary phases. Interfacial reactions may result in the formation of brittle, and possibly low-melting-point products that can degrade mechanical properties and decrease service temperatures. Lastly, when joining parts designed to operate in high-temperature environments, it is necessary to produce joints that can also withstand high temperatures.

There is also a set of ideal processing conditions aimed to minimize cost and degradation of the materials being joined. For instance, an ideal bonding process would require low bonding temperatures, which would save energy and enable parts with temperature-sensitive microstructures to be joined. It would also be ideal to use short bonding times, which would increase throughput and decrease exposure time at elevated temperatures. Minimal bonding pressure to bring the parts into intimate contact is also highly desirable because it would decrease processing costs (e.g., no complex fixturing) and would prevent deformation of the parts being joined. As will be discussed, in actual systems, these ideal joint properties and processing conditions are often conflicting, and it is typically necessary to make compromises.

Currently, there are a few conventional joining methods used for bonding ceramics, each with characteristic benefits and drawbacks. One of the most widely used processes is brazing, which involves melting a metallic layer between the parts being joined and allowing it to solidify during cooling. The liquid metal flows to fill the gap between the faying surfaces and draw the parts together. Brazing typically requires short bonding times – on the order of several minutes, and low bonding pressures – only a small clamping pressure is used to hold the parts in place. Using a low-melting-point braze may also minimize the bonding temperatures. Clearly, the processing conditions used for brazing are similar to the ideal processing conditions. However, there are some drawbacks associated with the properties of brazed joints. The bond strengths of brazed joints are largely determined by how effectively the liquid flows into interfacial gaps, or how well the liquid *wets*, or spreads on, the joining surfaces. If the liquid metal is able to wet the joining surfaces, which is typically observed when brazing metallic parts, interfacial void size and population are minimized. However, when the liquid

does not wet the faying surfaces, which is often the case when brazing ceramics, the liquid does not spread to fill the gaps, resulting in incomplete bonds with large interfacial flaws. Thus, surface modification or the addition of reactive metal(s) is typically required to braze ceramics. Brazed joints generally have limited service temperatures because the maximum allowable service temperature must be below the melting point of the braze and below the joining temperature. To increase the temperature capabilities of brazed joints, one must use a higher-melting-point braze, but higher bonding temperatures would be required.[1,2] In practice, because the yield strength of the braze decreases with increasing temperature, the useable service temperature of the joint is often well below the joining temperature.[3] Thus, brazing is generally inappropriate for joining high-temperature materials with temperature-sensitive microstructures.

In contrast, solid-state diffusion bonding involves plastic deformation and solid-state diffusion at the interface to "fuse" the solids together. This can be achieved with or without an interlayer. Since no liquid forms during bonding and the process takes place below the melting points of the constituents ($0.5T_{melt} < T_{bond} < 0.9T_{melt}$), the service temperatures of the joints can potentially match or exceed the bonding temperatures – ideal for assembling high-temperature structures. In solid-state diffusion bonding, it is possible to join ceramics using metal layers that would dewet as liquids, or have melting points that exceed that of the ceramic being joined. This facilitates the materials selection process, enabling a wider range of materials combinations to be joined. With the appropriate processing conditions, it is also possible to produce nearly flaw-free, high-strength interfaces. Compared to brazed joints, the properties of diffusion-bonded joints more closely mimic the aforementioned set of ideal joint properties. However, since diffusion bonding relies on plastic flow and solid-state diffusion to fill gaps, which are significantly slower than liquid flowing into gaps, much longer bonding times (on the order of tens of hours) and higher bonding pressures (typically 10 – 100 MPa) are required. Higher bonding temperatures may be used to ease bonding time and pressure requirements, but can result in microstructural degradation of the parts being joined. Since there is no liquid to flow into gaps and voids, the faying surfaces must also be exceptionally clean, nearly parallel, and well polished, which adds to the processing costs. Compared to brazing, diffusion bonding has a higher potential to produce joints with nearly ideal properties, but requires much more demanding processing conditions.

In an effort to combine the advantages of both brazing and diffusion bonding, and eliminate many of their shortcomings, Iino[4] and Glaeser[5] independently developed transient-liquid-phase (TLP) bonding for ceramics. TLP bonding is a liquid-phase bonding process that requires less demanding processing conditions than diffusion bonding, but produces joints that have significantly higher service temperatures than brazed joints. While several successful interlayer systems have been developed in previous studies, the complex interrelationships between processing conditions and joint properties make interlayer design in TLP bonding very challenging. The current study explores model multilayer Ni/Nb/Ni and Co/Nb/Co interlayer systems to establish the effects of processing conditions, interlayer chemistry, core-layer (Nb) microstructure, and wetting behavior on the mechanical properties of the joints to provide a framework for new interlayer designs for joining a wide variety of ceramics.

2. Background

In numerous industries, from microelectronics to aeronautics, ceramics are used for their unique and advantageous properties. While metals are used extensively in most structures for their toughness, formability, relative abundance, and manufacturability, there are many applications, such as those in high-temperature and corrosive environments, in which metals are simply inadequate. In such cases, ceramics are highly desirable because they are typically much more chemically stable, resistant to creep, and have high melting points. However, ceramics are brittle and in general have lower fracture toughness than metals, making them difficult to form into complex shapes. Thus, it is often necessary to join smaller ceramic parts to fabricate larger, more complex assemblies. As discussed in the previous chapter, solid-state diffusion bonding offers the potential to produce joints with high service temperatures, but requires demanding processing conditions. In contrast, brazing involves a nearly ideal joining process, but produces joints with limited service temperatures. This chapter will identify the effects of key processing parameters in ceramic joining and explain how TLP bonding circumvents some of the disadvantages associated with brazing and solid-state diffusion bonding.

2.1 Wetting Behavior

2.1.1 Contact Angle and Work of Adhesion

In any liquid-based joining process, such as brazing, the liquid must flow into interfacial gaps to draw the two surfaces together, and then solidify to form a permanent bond. The driving force of this capillary flow is determined by the wetting behavior of the liquid on the two joining surfaces. Sessile-drop experiments, in which liquid droplets are formed or placed on solid substrates, are commonly used to quantify wetting characteristics. In this configuration, a system forms a characteristic equilibrium contact angle, θ, where the liquid surface meets the solid surface, or at the *triple line*, as illustrated in Figure 2.1a. Assuming that the solid is perfectly smooth, insoluble in the liquid, and remains perfectly rigid, this contact angle is given by the Young equation,

$$\cos\theta = \frac{\gamma_{sv} - \gamma_{sl}}{\gamma_{lv}} \tag{2.1}$$

where the γ_{ij} terms represent the interfacial tensions of the *i-j* interfaces, with *s*, *l*, and *v* denoting the solid, liquid, and vapor phases, respectively. The values of γ_{ij} terms are the interfacial energies. When $\theta < 90°$, the liquid is said to *wet* the solid, and when $\theta > 90°$, the liquid is said to be *non-wetting*.

The interaction between the liquid and the solid substrate is also described by the *work of adhesion*, W_{ad}, which is defined as the reversible work required to replace the solid-liquid interface with two free surfaces (Dupré equation)

$$W_{ad} = \gamma_{sv} + \gamma_{lv} - \gamma_{sl} \tag{2.2a}$$

Work of adhesion is lower when the solid-liquid interfacial energy is lower than the sum of the solid and liquid surface energies, i.e., it is more energetically favorable to form the solid-liquid interface.

Experimentally, it is relatively simple to measure γ_{lv}, but difficult to obtain γ_{sv} and γ_{sl}. However, when Eqn. 2.2a is combined with Eqn. 2.1 to obtain the Young-Dupré equation,

$$W_{ad} = \gamma_{lv}\left(1+\cos\theta\right) \tag{2.2b}$$

the work of adhesion can be obtained by using two measurable quantities, θ and γ_{lv}. For liquid-metal/solid-Al_2O_3 systems, it has been shown that the work of adhesion increases with increasingly negative oxide formation free energy of the metal.[6,7]

It is somewhat expected that bond strengths would be related to W_{ad}, since interfacial fracture involves separating the two parts along the interface to create two free surfaces. Previous studies have attempted to show the relationship between W_{ad} and bond strength.[8-10] However, no clear conclusions were reached because the measured bond strengths depend on energy dissipation through plastic deformation of the droplet, residual stresses from thermal-expansion mismatch, and interfacial flaw size and population. It should also be noted that W_{ad}, θ, and γ_{lv} are quantities that describe the interaction between the *liquid* metal and the solid substrate, while mechanical tests are performed on the solidified bonds. Furthermore, as it will be discussed in a later section, strong bonds between a ceramic and a non-wetting metal can be produced through solid-state diffusion bonding.

2.1.2 Parameters Affecting Contact Angles

The Young equation (Eqn. 2.1) shows that a given materials combination has a characteristic contact angle based on their interfacial tensions. However, in high-temperature wetting experiments, deviations from the Young contact angle may be observed due to substrate deformation at the triple line, surface roughness, changes in liquid and solid compositions, and furnace atmosphere. For example, in contrast to the assumptions made in the Young equation derivation, at high temperatures, even rigid materials, such as Al_2O_3, can form ridges along the triple line due to the vertical component of the liquid surface tension. This process takes place through solid diffusion and creep deformation. The formation of ridges leads to changes in the local interfacial curvatures, which drives diffusion near the triple line and increases the ridge height. This can affect the spreading kinetics as well as the observed contact angles.[11] In a sessile-drop configuration, when the solid metal first melts on the ceramic substrate, the liquid rapidly (typically in <1 s) transforms into a spherical cap, as shown in Figure 2.1a. Contact angles measured within $<10^3$ s are similar to the equilibrium contact angles described by Eqn. 2.1, since there is insufficient time for significant diffusion to occur at the interface and thus, for the solid to form ridges with measurable dimensions. For time scales between 10^3 – 10^5 s, however, the solid may form ridges along the triple line (Figure 2.1b),[12] and depending on the ridge height relative to the droplet radius of curvature, the presence of ridges may affect the measured contact angle.[11] Formation of ridges allows the system to achieve local equilibrium, but global equilibrium is reached in isotropic systems when the solid-liquid interface has a constant curvature (Figure 2.1c).[13,14] The Smith equation describes the equilibrium relationships between the three dihedral angles and the surface tensions at the triple line

$$\frac{\gamma_{sv}}{\sin\phi_l} = \frac{\gamma_{sl}}{\sin\phi_v} = \frac{\gamma_{lv}}{\sin\phi_s} \tag{2.2}$$

where ϕ_i terms represent the dihedral angles in phase *i*, as drawn in the inset in Figure 2.1c. This expression has also been used to describe grain-boundary-grooving angles in polycrystalline materials.

In practice, the equilibrium dihedral angles in a solid ceramic-liquid metal system are often very difficult to obtain in high-temperature systems because reaching global equilibrium often requires exposing the sample to elevated temperatures for tens of hours. Long anneal times can result in the evaporation of the liquid, adsorption of evaporated materials on the substrate surface, as well as changes in the substrate and liquid compositions, substrate microstructure, and surface roughness (for instance, due to grain-boundary grooving in polycrystals), which can all independently change the contact angle. Fortunately, in liquid-phase joining, the time needed for a wetting liquid to fill interfacial gaps is on the order of a few seconds, which is typically not sufficient for any significant deformation to occur in the solid. Thus, the contact angles measured within short times, essentially the Young contact angles, are the relevant values for characterizing joining processes.

Substrate surface roughness can also affect the contact angle and the spreading behavior of the liquid. It should be emphasized that because surface roughness does not fundamentally change the surface energies, the microscopic contact angle should still be equal to the Young equilibrium contact angle. However, on a macroscopic scale, the *observed* contact angle may be quite different. In real systems, *advancing* and *receding contact angle hysteresis* is observed due to surface roughness. Advancing angle refers to the contact angle of a spreading liquid, while receding angle refers to that of a retracting liquid. As described in more detail by Eustathopoulos,[14] when either an advancing or a receding liquid front encounters a sharp feature on a surface, the triple line may be pinned and the liquid may form a range of contact angles with respect to the plane of the surface. Thus, the observed contact angle may be quite different when surface roughness is varied.

Several models have been developed to describe the effects of roughness on wetting. However, these models are limited to specific conditions, largely because roughness itself is very difficult to quantify (long- vs. short-wavelength features, shapes of surface features, etc.).[14] One of the first treatments to consider the effects of surface roughness on wetting was by Wenzel,[15,16] who stated

$$\cos\theta_r = r\cos\theta \tag{2.3}$$

where θ_r is the contact angle on a rough surface, θ is the equilibrium (Young) contact angle on a perfectly smooth surface, and *r* is the roughness factor, or the ratio between the actual surface area and the projected surface area. Eqn. 2.3 predicts that a wetting liquid would form a lower contact angle, while a non-wetting liquid would form a higher contact angle as the surface roughness increases. Unfortunately, this expression proved to be quite limiting in describing a wide range of real systems. For instance, Nakae *et al.* showed that the Wenzel equation does not take into account any details of the roughness or the range of contact-angle hysteresis that is typically observed in real systems.[17] In addition, Wolansky and Marmur showed that the Wenzel equation is only valid when the roughness scale of a saw-tooth surface is much smaller than the dimension of the liquid droplet.[18] Another shortcoming of the Wenzel model is its assumption that the liquid fills all surface flaws, but with a non-wetting liquid, these flaws may be left unfilled and become interfacial voids. Such cases require an additional term accounting for the liquid-void interfaces.[17,19] A different model proposed by Shuttleworth and Bailey described contact angle hysteresis with respect to the angles of the grooves on the solid surface, but did not take into account the groove dimensions.[20] While some general trends

have been drawn from these studies, they often deal with contrived surface features, and as a result, fail to fully describe the wetting behavior of real systems.

The two factors that affect contact-angle measurements presented thus far, ridging and surface roughness, do not fundamentally change the characteristic contact angle of a given system, but rather, have the effect of distorting the macroscopically observed contact angle. However, significant changes in the characteristic contact angles are observed when the liquid chemical composition is altered, either through the introduction of impurities or alloying components. The biggest differences in contact angles are observed between *reactive* and *non-reactive* metals. Non-reactive metals, such as Au, Ag, Cu, and Sn, form contact angles >100° on ceramics.[21] The contact angle of Ni on Al_2O_3 has been reported to be ≈100°–120°.[7,22] When reactive metals such as Zr,[23] Ti,[24] or Cr[25] are added to non-reactive liquid metals, the contact angles decrease dramatically. This has been attributed to the increased affinity for oxygen, where the reactive-metal addition either reacts to form stable oxide layers[22,23] or forms oxide clusters in the liquid that adsorb onto the interface.[7,26-28] With any chemical reactions, however, there is some equilibrium constant that determines the relative amounts of reactants and products. Thus, even a "non-reactive" liquid metal in contact with an oxide ceramic, for example, an reduce some minute amount of the substrate along the interface. Therefore, it is unclear as to exactly what distinguishes reactive metals from non-reactive metals. One method of distinguishing these metals was proposed by Eustathopoulos and Drevet,[29] who showed that for a liquid metal on an oxide substrate, the mole fraction of O dissolved in the liquid, x_O, can be estimated using known thermodynamic quantities. For metals with $x_O < 10^{-6}$, the contact angles were found to be ≈120° and independent of x_O values. For metals with $x_O > 10^{-6}$, however, significantly lower contact angles were observed for systems with higher x_O values.[29] This method appears to be the most systematic and effective way to distinguish reactive and non-reactive metals. However, some non-wetting metals, such as Ni on Al_2O_3, are classified as "reactive," which may lead to some confusion, and a method of characterizing liquid alloys has not yet been established.

The wetting properties are also affected by the furnace environment, or more specifically, P_{O2}, the partial pressure of O_2. With molten Cu on Al_2O_3, for example, contact angles have been found to decrease to <100° with increasing P_{O2}.[30-32] These measurements were made at sufficiently low P_{O2} levels to reduce Al_2O_3. At higher P_{O2} levels (>10^{-11} atm), θ, γ_{sl}, and γ_{lv} all decrease, due to the formation of a two-dimensional $AlCuO_2$ phase at the solid-liquid interface[32] and the adsorption of O on the liquid surface.[31] If a Cu_2O layer is present on the Cu surface prior to melting, then Cu_2O and Al_2O_3 can undergo a eutectic reaction to form $AlCuO_2$.[33] This changes the wetting behavior, as the liquid forms in contact with the $AlCuO_2$ phase. Thus, the furnace atmosphere may be controlled to improve wetting and adhesion, but excess P_{O2} levels may result in the formation of a brittle oxide layer at the interface.

2.2 Conventional Joining Methods

2.2.1 Brazing

Brazing is used to join a wide range of materials for numerous applications because it is a cost-effective and rapid joining process. Brazing typically requires short bonding times, low bonding pressures, and depending on the type of braze, modest bonding temperatures. These favorable processing conditions are due to the formation of a liquid that flows to fill interfacial gaps and voids. However, because most liquid metals are non-wetting on ceramics, brazing ceramic parts is quite challenging. As a result, many studies on brazing ceramics have been devoted to changing the liquid or

the ceramic surface chemistries to improve wetting and adhesion. One often-used processing route is metallization, which involves forming robust Mo[34-37] layers on the ceramic surfaces, and then allowing the braze to adhere to the metallic surfaces. Since liquid metals tend to wet metallic surfaces, the liquid is able to fill interfacial gaps much more effectively and form stronger joints. The metallization process consists of first painting or coating the ceramic surface with a mixture of Mo-Mn powder suspended in an organic solution. This powder is subsequently sintered onto the ceramic surface by firing at 1500°C in a wet H_2 atmosphere. The sintered layer is then coated with a lower-melting-point metal, such as Ni or Cu, typically through electroplating. The Ni or Cu layer is sintered onto the Mo layer, again in a H_2 atmosphere at an elevated temperature. Lastly, the metallized ceramic parts are joined using a non-reactive braze, such as Cusil® (Ag-Cu eutectic alloy). While this process is widely used to produce reliable ceramic joints, it involves multiple high-temperature steps prior to joining, which can damage temperature-sensitive components and increase costs.

To avoid this multi-step process, numerous studies on developing suitable active-brazing alloys for direct bonding of ceramics have been conducted. These alloys contain small amounts of Ti, Zr, Hf, or other reactive metals[38,39] that readily form oxides, nitrides, or carbides, *via* redox reactions with the ceramic. Addition of even small amounts of Ti (a few at.%) to non-reactive brazes, for example, has been found to drastically improve wetting and adhesion of liquid metals on Al_2O_3.[24,40-44] However, higher concentrations of reactive metals lead to the formation of thicker reaction layers, which tend to contain pores and cracks due to volume mismatch.[45-48] Therefore, an ideal brazing alloy must be designed such that the active-metal addition has a high activity, but a low reaction rate, which would promote wetting and minimize reaction-layer thickness.[48]

Currently, there are many commercially available brazing alloys that are quite effective in forming strong, reliable ceramic joints.[49] These brazing alloys have relatively modest melting points (in the case of Ag-Cu–based alloys, ≈600°C – 900°C) to allow for modest bonding temperatures. However, this also limits the service temperatures of the resulting brazed joints, since the service temperatures must be below the melting points of the brazing alloys. In practice, brazed joints are often susceptible to significant softening above 50% of the joining temperature.[3] Common approaches to increase high-temperature strengths of brazed joints are to either use brazes with higher melting points,[1,2] which inevitably increases the joining temperatures, or to use thinner interlayers, which further constrains the metal layer, but decreases fracture toughness.[3,50] The latter approach does not necessarily affect the microstructure or the properties of the materials being joined, but the former is problematic if the temperature at which microstructural degradation initiates is below the melting point of the brazing alloy. Thus, in general, fabricating high-temperature joints through brazing is not feasible.

Despite some of the shortcomings associated with brazed joints, brazing still offers versatility and nearly ideal processing conditions. It is clear that brazing is a cost-effective and rapid joining process, particularly suited for high-volume production. There have been countless studies dedicated to developing new brazing alloys or optimizing the compositions of existing alloys to obtain certain joint properties.[37,41,42,45,47,51] As a result, there are numerous commercial brazing alloys available for joining a wide range of materials for many applications.

2.2.2 Solid-State Diffusion Bonding

While brazing has proven to be a cost-effective joining process, in many cases, it is unable to produce joints that allow full exploitation of high-temperature structural ceramics. As an alternative,

solid-state diffusion bonding is used to produce joints that can potentially survive significantly higher service temperatures. Solid-state diffusion bonding relies on local deformation and diffusion along the interface to fill gaps and voids. This process may or may not include an interlayer between the parts being joined. However, when joining ceramics, it is advantageous to use a metallic interlayer, which is typically more ductile than the ceramic parts being joined, and thus, better able to plastically flow into interfacial gaps and voids. Diffusion bonding, in general, requires bonding temperatures 0.5 – 0.9 T_{melt} of the interlayer. Thus, unlike brazed joints, the service temperatures of diffusion bonds can potentially approach or exceed the bonding temperatures. Higher service temperatures may be achieved by using interlayers with melting points approaching or exceeding those of the ceramics being joined, such as Nb, which has been used to join Al_2O_3.[52] Diffusion bonding is also more effective in joining ceramics with noble or nonreactive metal interlayers, such as Au,[53,54] Pt,[55] and Ag.[56-58] This makes diffusion-bonded joints more suitable for oxidizing environments. However, since diffusion bonding does not involve the formation of a liquid that fills interfacial gaps and voids, but rather, relies on solid-state diffusion and plastic flow, significantly longer bonding times and higher applied loads are required. Joint properties are also highly sensitive to the joining-surface roughness, and therefore, diffusion bonding requires much more stringent surface preparation to produce strong, hermetic interfaces.[59,60]

To better understand the diffusion-bonding process, many studies have focused on modeling and predicting the bonding mechanisms. In one of the first attempts to model diffusion bonding, Hamilton used creep-deformation rates for a Ti alloy to determine the relationships between bonding temperature, pressure, and time needed for pore closure between two sawtooth surfaces.[61] Hamilton's model was fairly accurate in predicting the processing conditions necessary to obtain bond strengths matching the strength of the base metal, but some errors were present because the effects of diffusion were neglected. Garmong *et al.* expanded on Hamilton's creep deformation model by including the effects of volume diffusion and the presence of long- and short-wavelength asperities on the surfaces.[62] The calculations were based on pressing and deforming this patterned surface against a flat surface until all of the asperities disappeared. Garmong *et al.* state that in the initial stage of bonding, the applied load and elevated temperature allow creep deformation to flatten the long-wavelength asperities. Then, in the following stage, both diffusion and creep deformation lead to the collapse of microvoids.[62] In a later study, more specific diffusion and deformation mechanisms, similar to those occurring in powder sintering, were proposed.[63,64] This work showed that power-law creep is the dominant mechanism in the initial stages of bonding. Once intimate contact is formed between the joining surfaces through creep deformation, the remaining pores are removed by volume diffusion. For example, with Nb-Al_2O_3 diffusion bonds, the bond fronts grow to fill interfacial gaps. When these fronts meet each other to form a pore channel, the channel breaks up into small pores, which eventually disappear.[65]

In diffusion bonding, it is essential that an appropriate set of processing conditions is used to activate sufficient plastic flow and diffusion along the interface to produce interfaces with few or no flaws. Barring any formation of reaction products at the interface, as would be the case with a noble-metal–Al_2O_3 pair, this may be achieved using different bonding time-temperature-pressure combinations, as these variables are complementary. For instance, if a relatively low bonding temperature must be used to preserve the microstructures of the parts being joined, a combination of longer bonding time and higher bonding pressure may be used to compensate for the lower plastic flow and diffusion rates associated with the lower temperature. If a higher throughput is desired, a

shorter bonding time may be used with higher bonding temperature and pressure, which increase the deformation and diffusion rates. In contrast to brazing, where the process variables are determined by the characteristics of the brazing alloy, in diffusion bonding, the processing conditions may be tailored to accommodate particular materials combinations or production demands.

Several studies explored the effects of processing temperature, time, and applied pressure on the mechanical properties of diffusion bonds. Of these variables, the bonding temperature is the only one that affects both the plastic flow and diffusion. Thus, to obtain a bond with measureable strength, a sufficiently high processing temperature must be used to thermally activate plastic flow and diffusion. When higher bonding temperatures are employed, the interfacial flaw population and size decrease resulting in higher bond strengths. Nicholas and Crispin[58,66] claimed that the strength of Al_2O_3/Al/steel/Al/Al_2O_3 assembly was described by an Arrhenius expression,

$$BS = B_o \exp\left(-Q / RT\right) \tag{2.4}$$

where BS is the bond strength, B_o is a constant (2.5×10^6 MPa), T is the bonding temperature, and Q is the apparent activation energy (80.3 kJ mol^{-1}). Eqn. 2.4 fits the bond strength data obtained using bonding temperatures 450°C – 600°C, and shows that a threshold behavior is observed, where a bonding temperature >450°C was needed to obtain a measurable strength. Similar behavior was obtained when using Ag, Cu, and Ni interlayers, but peak strengths were observed in these systems, which was likely due to increased stresses developed from contraction mismatches during cooling.[58] In other studies, where bulk Kovar[67] and steel[68] were joined using Al and Cu interlayers, respectively, peak strengths were also observed for intermediate bonding temperatures. Other studies that used Au, Cu, and Pt interlayers to join Al_2O_3 showed that the bond strengths increased with higher bonding temperatures,[33,54,55] but did not exhibit an optimum intermediate bonding temperature. These studies show that when higher bonding temperatures are employed, bond strengths generally increase.

The relationship between bond strength and processing temperature becomes more complex when joining reactive metals, such as Ti, to ceramics. In such cases, the bonding temperature must be sufficiently high to allow a chemical bond to form between the metal and the ceramic. However, for a given bonding time, there is an optimal bonding temperature, above which the interfacial strength decreases.[69] Unlike brazed joints, where various forms of Ti oxides formed along the interfaces depending on the processing conditions, when Ti was diffusion bonded to Al_2O_3 in vacuum, a Ti_3Al intermetallic layer was found along the metal-ceramic interface.[69-72] At higher bonding temperatures, thicker intermetallic layers can form and degrade the mechanical properties of the joints. Similar to the case of reactive-metal brazing, the formation of a thicker reaction layer results in higher stresses from volume mismatch. Although strong bonds between reactive metals and ceramics can be formed, if the joints are to operate at elevated temperatures, the intermetallic layer may become thicker during service and be a source of failure. It has been shown that by using an interlayer such as Nb or Ta, which form complete solid solutions with Ti, the formation of intermetallic layers can be prevented, while retaining fracture energies comparable to Ti/Al_2O_3 bonds.[73]

Bonding time is also a critical processing variable because sufficient time is required for plastic flow and diffusion to fill interfacial gaps and voids. When a Pt interlayer was used to join Al_2O_3 at 1450°C, four-point-bend fracture strength increased from 70 MPa to >150 MPa when the bonding time was increased from 12 min to 10 h.[55] As expected, other interlayer/ceramic combinations, such as Au/Al_2O_3[54] and Cu/Al_2O_3[33,74] exhibited increased bond strengths when longer bonding times were

used. However, the bond strength may not always increase with longer bonding times. For example, when a thin Al interlayer was used to join bulk Al_2O_3 and bulk stainless steel, a maximum bond strength was obtained after a 30-min bonding time.[66] With a 120-min bonding time, samples fractured along intermetallic layer between the steel and the Al interlayer. When joining Ti and Al_2O_3, longer bonding times resulted in the formation of an excessively thick Ti_3Al intermetallic layer, which decreased both the fracture strength and the joint toughness.[75] If the system forms a reaction layer(s) along the interface(s), the bond strength will be highly dependent on the reaction-layer thickness, which increases with $\sqrt{t}$, where t is the bonding time.

The bond strengths are also expected to increase with greater bonding pressures. Bonding pressures associated with diffusion bonding are several orders of magnitude higher than the typical clamping pressures used in brazing. Applied pressure is expected to serve two main purposes when joining metals with ceramics: break the surface oxide on the metal to allow direct contact between the ceramic and the clean metal surface, and induce plastic flow to fill interfacial gaps and increase the area fraction of metal-ceramic contact. Thus, increase in bonding pressures generally corresponds to higher bond strengths. However, once sufficiently high bonding pressures are used, the strength becomes independent of the bonding pressure since all or most of the interfacial voids are filled.[33,54,55,67]

Solid-state diffusion bonding produces joints at reduced bonding temperatures relative to the maximum operating temperatures of the joints. High bond strengths can be attained in diffusion bonds, but compared to brazing, it requires much longer bonding times, higher applied pressures, and more stringent surface finish, which sum to significantly higher costs and lower throughput. Currently, diffusion bonding is used mostly in specialized applications, such as joining components for laboratory equipment, where brazed joints are insufficient.[59,76]

2.3 Transient-Liquid-Phase (TLP) Bonding

2.3.1 Metal-Metal TLP Bonding

TLP bonding[77] has been primarily developed to join high-temperature alloys that are otherwise difficult or impossible to join using conventional methods. Previous studies provide qualitative descriptions of the TLP bonding process.[77-79] This method uses an interlayer containing a melting-point depressant (MPD) or a low-melting-point constituent. When combined with the base-metal parts being joined, a liquid forms at a reduced temperature due to either a eutectic reaction or a depression of the solidus temperature. Depending on the solubility limit of the parent metal in the liquid, the liquid layer thickens as it dissolves some of the parent metal. Simultaneously, the MPD diffuses out of the interlayer and into the parent metal, which depletes the liquid of the MPD. This allows the liquid layer to shrink, and then solidify isothermally when "long-range" MPD diffusion is realized. Continued annealing at the bonding temperature allows the MPD concentrations to equalize, resulting in a joint that is chemically indistinguishable from the joined parts. Thus, in principle, TLP bonding allows metal parts to be joined at reduced temperatures, while producing joints that can match the parent-metal properties.

Previous studies have shown that TLP bonding can effectively join various high-temperature metals. Lynch *et al.*,[80] showed that Ti can be joined using a thin Ni layer, which enables the formation of a liquid as low as 955°C. The evolution of the TLP bonding process was observed for various isothermal holding times to show that the interlayer width decreased with increased bonding time, until finally, the joint appeared to be essentially a grain boundary. Ag has also been shown to be an effective MPD for producing Ti joints with high shear strengths.[81] Wu[82] and Wells[83] used Cu as the

MPD to produce joints that match the mechanical properties of the base metal. While these earlier studies demonstrated that TLP bonding allows Ti to be joined effectively, it was also shown that using a set of appropriate processing conditions, which are materials-combination specific, is critical in avoiding the formation of unwanted intermetallic phases. The presence of secondary phases can degrade the joint properties, particularly in high-temperature environments.

More extensive studies have been done in TLP bonding of Ni-base superalloys, as well as Ni and its intermetallics. Ni-base superalloys are specifically designed to operate at high temperatures, such as in turbine engines. However, unlike conventional alloys, superalloys are difficult/impossible to weld as this often leads to hot cracking.[84,85] As mentioned in an earlier section, brazed joints would not provide sufficiently high service temperatures, and diffusion bonding would be far too costly and difficult to execute when assembling hundreds of turbine blades in an engine. Thus, TLP joints provide the best combination of manufacturability and performance. In a study by Duvall *et al.*,[86] various Ni-Cr and Ni-Cr-Co superalloys were joined using small amounts of MPDs, such as B and Si. The interlayers had compositions similar to those of the base metals to facilitate rapid homogenization and allow the joint to become chemically indistinguishable from the base metal. B was used in all interlayers because it is effective in depressing the melting point *and* can diffuse rapidly into the base alloy.[86] Despite using an MPD with high diffusion rate, holding times up to 24 h were needed to achieve complete isothermal solidification. Insufficient bonding times led to solidification during cooling, which resulted in the formation of brittle boride phases in the joint. Similar results were obtained when Ikawa *et al.*[87] joined Ni-base alloys using electroplated Ni-P and Ni-B interlayers; again, long holding times were needed to obtain fully homogenized joints. More recently, commercial TLP insert metals have been developed for joining Ni-base alloys, such as BNi-3 (Ni-4.5Si-3.2B). Gale *et al.* observed the microstructures of Ni and NiAl bonded using BNi-3 to determine the nature of the solidification process (isothermal vs. during cooling). When Ni/BNi-3/NiAl and Ni/BNi-3/Ni joints were produced, it was determined that a 2-h holding time at 1065°C was sufficient for complete isothermal solidification.[88-90] However, when NiAl/BNi-3/NiAl joints were made, holding times as long as 72 h were needed.[91] This large difference in solidification times was attributed to the low diffusivity of B in NiAl ($\approx 10^{-12}$ m^2 s^{-1}) compared to that in Ni ($\approx 10^{-10}$ m^2 s^{-1}).[89] While these joints solidified isothermally, multiple intermetallic phases, Ni_3B, Ni_3Al, and Ni_3Si, precipitated near the interface. The precipitation of Ni_3B could be avoided by using a bonding temperature (1150°C) greater than the Ni-B eutectic (1095°C), but extensive liquation of Ni was observed.[89] Although mechanical properties of these joints have not been measured, the presence of intermetallic phases often leads to degradation of mechanical properties. For instance, Gale and Guan reported large scatter in the shear strengths of both NiAl/Cu/Ni and NiAl/Cu/MM-247 (Ni-base superalloy) joints[92] that solidified isothermally, but formed intermetallic phases. This demonstrates that ideal microstructures and joint properties can be obtained when high bonding temperatures are used, but the process becomes impractical when the processing temperatures are exceedingly high.

Clearly, one of the key hurdles in TLP bonding is to minimize the isothermal-solidification time. One possible approach to reduce the isothermal-solidification time is to decrease the amount of liquid formed by using a lower bonding temperature. However, this also decreases the MPD-diffusion rate in the parent metal. Conversely, the bonding temperature may be increased to accelerate diffusion, but this typically increases the amount of liquid formed. Joining nominally flat and well-polished surfaces, which would minimize the interfacial-gap width, can also reduce the liquid volume needed to fill the gap. However, this requires additional time and cost to obtain more stringent surface finishes.

Likewise, higher bonding pressure can be used to reduce the gap width, and thus, the liquid volume, but this may increase processing costs and require more complex equipment. The interrelationships between the bonding temperature, time, and interfacial gap width (related to bonding pressure and surface roughness) is quantified through TETIG (**TE**mperature, **TI**me, and **G**ap) diagrams.[93] TETIG diagrams consist of two axes, where, for example, the y-axis shows the bonding temperature and the x-axis represents the gap width. Various curves are then plotted for different isothermal holding times to show the temperature-time-gap-width combinations needed to achieve complete isothermal solidification. These diagrams, thus far, have only been constructed empirically, but are useful in displaying the general trends.

One method of decreasing the isothermal-solidification time, called wide-gap TLP bonding,[94-97] uses a composite interlayer containing non-melting, base-metal powder, and MPD powder. In contrast to an interlayer that melts completely, the wide-gap method allows the solid particles to fill the gap, thereby reducing the necessary amount of liquid, and provide larger surface area for MPD diffusion to occur. In Gale and Guan's study,[94] for example, it was found that by including a non-melting NiAl powder with Cu in the interlayer (6:1 NiAl:Cu ratio by weight), complete isothermal solidification can be achieved in 1 min at 1150°C when joining single-crystal NiAl and polycrystalline MM-247 alloy using a 175-μm thick interlayer. In comparison, when a 50-μm thick layer of Cu was used to join the same materials at 1150°C, a 1-h holding time was required.[92] Joints made with the NiAl/Cu interlayer had a ≈10-μm wide region containing precipitates adjacent to the bond line, while those made with the Cu interlayer had a ≈90-μm wide region. The presence of NiAl particles reduced the amount of base-metal dissolution and Cu diffusing out of the interlayer, resulting in significantly less intermetallic precipitates forming away from the interlayer. The wide-gap method was also used to join Ti-48 at.% Ni-2% Al-2% Cr ("48-2-2") alloy with a mixture of Cu and 48-2-2 alloy powders. This required a mere 10-min solidification time at 1150°C. Furthermore, when the joints were annealed in Ar at 1350°C for 1 h, the bond line became barely discernible, with no secondary phases.[97] Clearly, wide-gap TLP bonding has the potential to reduce the bonding time and, with the right materials combinations, prevent the formation of secondary phases that may degrade joint strengths.

Currently, TLP bonding is used to join and repair high-temperature components in heat exchangers and turbine engines. There are commercially available foils and preforms, which are essentially mixtures of MPDs (B and Si) and non-melting metal (Ni-base alloy). The relationship between materials combinations and processing conditions in TLP bonding is much more complex than in brazing and solid-state diffusion bonding. However, TLP bonding has the potential to produce high-temperature joints using reduced bonding temperatures and relatively short bonding times.

2.3.2 Modeling of TLP Bonding

Experimental studies on TLP bonding showed that the isothermal-solidification time is a strong function of the MPD diffusivity-solubility product. As mentioned previously, the isothermal-solidification times can vary greatly between different materials combinations, making it very challenging to determine the appropriate processing conditions. Likewise, determining a suitable materials combination within certain processing constraints can also be difficult. The complex nature of TLP bonding has led to the development of several calculation methods to determine the processing conditions.

As described by Tuah-Poku *et al.*,[79] the TLP bonding process may be separated into discrete steps: 1) dissolution of the interlayer, 2) homogenization of the liquid, 3) isothermal solidification, and 4) homogenization. Both analytical and numerical approaches have been used to describe all four stages of TLP bonding. Particular attention has been paid to determining the kinetics of the isothermal-solidification step, as it is the rate-limiting step of the entire process, and perhaps the most difficult to predict.

One of the first attempts to calculate the rate of solid-liquid interface displacement was by Lynch *et al.*[80] He solved for the net flux of the solute across the solid-liquid interface to determine the expression for the solidification rate, or the (solid-liquid) interfacial velocity,

$$\frac{dx}{dt} = K\left[\frac{R_1 D_L^{1/2} - R_2 D_S^{1/2}}{t^{1/2}}\right] \tag{2.5}$$

where K, R_1 and R_2 are constants, t is the isothermal holding time, and D_L and D_S are the solute diffusivities in the liquid and the solid, respectively. Unfortunately, this expression contains several unknown constants, and thus, could not be used to compare with the experimental results. Eqn. 2.5 does show that the isothermal-solidification rate is inversely proportional to $t^{1/2}$, which is consistent with subsequent studies.[79,98,99]

More recently, analytical models based on solutions to Fick's equation have been developed and compared with experimental results. One of the key studies was done by Tuah-Poku *et al.*,[79] who showed that the time needed for isothermal solidification was given by

$$t = \frac{\pi W_o^2}{16 D_s}\left(\frac{C^{\beta}}{C^{\alpha L}}\right)^2 \tag{2.6}$$

where W_o is the initial interlayer width, D_s is the MPD diffusivity in the parent metal, C^{β} is the solidus composition, and $C^{\alpha L}$ is the liquidus composition. Ikawa *et al.*[100] and Nakao *et al.*[101] also developed a solution for isothermal-solidification time using a similar approach. Tuah-Poku *et al.* showed that for a Ag/Cu/Ag sandwich joint, Eqn. 2.6 predicted 1200 h for complete isothermal solidification to occur. Compared to the experimentally predicted solidification time of ≈200 h, which was obtained by extrapolating the interlayer width vs. time data, the calculated times were significantly longer.

MacDonald and Eagar[99] used a moving-boundary analysis, which accounts for the MPD diffusion across an advancing solid-liquid interface. For comparison, Ag/Cu/Ag joints were produced at 820°C with holding times ranging from 1–64 h using a 100-μm thick Cu interlayer. Their model predicted an isothermal-solidification time of ≈1400 h. However, extrapolating the interlayer width vs. time data suggested that a ≈300-h solidification time is needed. The authors noted that the solid-liquid interfaces were non-planar and the thicknesses varied with position, making it difficult to measure the liquid-layer width accurately. Since the solidification rate is directly related to the Cu-diffusion rate, MacDonald and Eagar compared the measured and calculated Cu-concentration profiles in the Ag substrate near the Ag/Cu interface. This comparison showed that the model was accurate in tracking the Cu-diffusion profiles with respect to the isothermal-holding time, but no further attempts to measure the actual solidification time were made.

Several hypotheses have been put forth to account for the large discrepancies observed between the calculated and experimental isothermal-solidification times. One possible source of error is the difference between the predicted and the actual amount of liquid (i.e., the amount of MPD) retained in the joint. For instance, if excess liquid forms relative to the gap width, it will flow out of the joint. This makes it very difficult to control the exact amount of liquid that solidifies isothermally, and experimentally replicate the boundary conditions used in the models. These studies used different experimental setups intended to control the overall MPD concentration. In Tuah-Poku's work, two Ag discs were joined using an 80-μm thick Cu interlayer, which was surrounded by a 100-μm thick Ta washer. The assembly was held in place with a light clamping pressure, which, when combined with the Ta washer, should have maintained a 100-μm-wide gap. However, when the joints were heated to 820°C and quenched after various holding times (5–30 min), it was observed that the liquid film widened to ≈420 μm, which was comparable to the calculated maximum liquid-film width (≈380 μm).[79] This perhaps suggests that the clamping pressure was not sufficient to maintain the intended gap width and it is unclear how much, if any, liquid was lost during bonding.[99] MacDonald and Eagar used a more elaborate system, which controlled a very low constant bonding pressure to retain all of the liquid in the bond.[99] However, given that both MacDonald and Eagar, and Tuah-Poku *et al.* observed similar discrepancies in their respective comparisons between the calculated and extrapolated isothermal-solidification times, it is not entirely clear how effective either experimental setup was in replicating the boundary conditions used in the calculations.

Both Tuah-Poku *et al.*, and MacDonald and Eagar also cited that the solid-liquid interfaces did not remain planar, but instead, developed ≈25 – 50-μm-deep grain-boundary grooves. The regions of the solid-liquid interface intersecting grain boundaries grooved in order to accommodate the varying directions and magnitudes of the surface tensions.[102] This made it difficult to measure the interlayer thicknesses because some regions appeared to have completely solidified, while, in others, the liquid remained. In addition, Tuah-Poku *et al.* noted that the calculated solidification times may have been much longer than the extrapolated time because the increase in the solid-liquid interfacial area increased the total Cu flux into Ag, which was not considered in the model.[79] The presence of grain boundaries intersecting the interfaces also increases the Cu flux since diffusivities along grain boundaries are typically several orders of magnitude higher than the lattice diffusivities, particularly at low-to-moderate temperatures ($T<0.7\ T_{melt}$). MacDonald and Eagar also added that because, in some systems, higher diffusivities have been observed when the solute concentration increases, the Cu diffusivity in Ag may increase as the Cu concentrations near Ag grain boundaries rise, leading to an irrigation diffusion mechanism.[99,103] Further evidence of grain-boundary-enhanced isothermal solidification was demonstrated by Kokawa *et al.* and Saida *et al.*, who both showed that the solidification time decreased when finer-grained Ni (40 μm vs. > 4 mm in Kokawa *et al.*[104]; 200 μm vs. 3.5 mm in Saida *et al.*[105]) was bonded. Several studies have also reported further enhancement of solute diffusivity due to migrating grain boundaries.[106-110] Thus, the presence of grain boundaries should increase the solute-diffusion rate, which decreases the isothermal-solidification time, but currently, there are no TLP bonding models that account for the effects of grain-boundary diffusion.

Numerical methods have been used to model the changes in the isothermal-solidification rates due to the presence of grain boundaries. Ikeuchi *et al.*[111] used a finite-difference method to show the effects of higher diffusivity along a grain boundary and the relative energies of the grain boundary and the solid-liquid interface. It was found that when interfacial energy terms were ignored, the solidification rate increased only in the vicinity of the grain boundary (within ≈3 μm from the grain

boundary). Furthermore, the solid surface protruded out of the solid ahead of the grain boundary, which is in contrast to the experimental observations of grain-boundary grooves extending *into* the solid. When the surface-energy terms were introduced, the grain boundaries grooved into the solid, similar to the experimental observations and the solid front >10 μm from the grain boundary advanced more rapidly. However, compared to the case where the effects of grain-boundary diffusion were neglected, the displacement of the solid-liquid interface away from the grain boundary was only a few microns greater.

While Ikeuchi's study mathematically showed the local effects of grain-boundary grooving on the solidification process, it did not show the global effects of having multiple grain boundaries over a larger volume. The model also assumes that the grain boundary is stationary, which is unlikely when joining polycrystalline solids at elevated temperatures. There are three classes of diffusion kinetics in polycrystals based on the diffusion distance and the average grain size, as described by Harrison.[112] According to Harrison, Type A kinetics refer to a case where the diffusion distance, $\sqrt{D_l t}$, where D_l is the lattice diffusivity and t is the processing time, is much larger than the grain size. The concentration profiles in the Type A regime follows the solutions to Fick's equation using an apparent diffusion coefficient. In Type B, lattice diffusion is confined to regions near the grain boundaries because $\sqrt{D_l t}$ is much less than the grain size. This essentially isolates diffusion along each boundary and the macroscopic diffusion profile does not obey Fick's equation. Lastly, Type C is observed when essentially no lattice diffusion takes place and only grain-boundary diffusion is observed. Cahn and Balluffi extended the three types by including the grain-boundary-migration distance, Vt, where V is the grain-boundary-migration rate.[113] In Zhou and North's numerical model, it was shown that grain-boundary migration increased the amount of solute diffused only partly through the processing time, where the maximum amount of solute diffuses when $\sqrt{D_l t} + Vt$ is comparable to the grain size (transition between Type A and Type B). The effect of grain-boundary migration is negligible for both short- and long-diffusion times.[108] Unfortunately, this model was not extended to determine the influence of grain-boundary migration on isothermal-solidification rates.

In another study by Zhou and North,[114] isothermal-solidification times were calculated using a numerical model and compared to previous experimental results obtained from joining single-crystal Ni with Ni-19 at.% P.[105] Zhou and North's calculations closely matched the experimental data largely because single-crystalline, rather than polycrystalline, Ni was joined, and thus, did not have to account for the effects of grain-boundary diffusion. Based on this comparison, it also appears that most of the liquid was retained in the actual joint, which had a stopper around the filler metal and welded clamps on the two base-metal plugs being joined to maintain a constant gap width.

It appears that in analytical and numerical models, the effects of grain boundaries on the solidification kinetics are not fully developed, largely due to the complex relationships between the effects of grain-boundary diffusivity, grain-boundary migration, base-metal microstructure, and the interfacial and surface energies. The current models also failed to mention or did not consider diffusion during heat and cooling – if, for instance, low heating rates are used, significant interdiffusion may occur prior to liquid formation, which may lead to less liquid forming in the joint than predicted. Furthermore, a more systematic method to determine just how much liquid is retained in the joint must be developed. Implementing these boundary conditions may improve existing models and make them more reliable in predicting isothermal-solidification times of real systems.

2.3.3 Ceramic-Ceramic TLP Bonding

Strong, reliable joints with high heat resistance are needed to fully exploit the advantageous properties of ceramics. Conventional brazing and solid-state diffusion bonding each offer advantages, but TLP bonding is the only joining method that has potential for cost-efficient production of high-performance ceramic joints. TLP bonding is particularly effective in circumventing mechanical property and microstructural degradation in the ceramic parts being joined, while maintaining their usability in high-temperature applications. Repair of expensive and hard-to-manufacture ceramic parts with TLP bonding, paralleling practices employed for repair of Ni-base superalloy components, would also be of great interest in various applications. However, the TLP bonding method used to join high-temperature alloys cannot be employed in joining ceramics because the dissolution and the diffusion of MPD into the ceramic would be too sluggish. Thus, TLP bonding of ceramics using a multilayer interlayer design was pioneered independently by Iino[4] and Glaeser.[5]

Similar to TLP bonding of metals, ceramic-ceramic TLP bonding utilizes a non-equilibrium interlayer, which forms liquid layers at moderate temperatures, and then undergoes isothermal solidification. As illustrated in Figure 2.2a, suppose that the interlayer consists of a B/A/B sandwich structure. For simplicity, assume that the A-B pair has a "lens" binary phase diagram. In this system, thin layers of the lower-melting-point metal, or the MPD, B, flank the higher-melting-point core-layer metal, A. If the system is heated to some temperature T_{bond}, where $T_{melt,\,B} < T_{bond} < T_{melt,\,A}$, the cladding melts, and the liquid dissolves A until it saturates at the liquidus composition. Concurrently, the solid surface absorbs sufficient B to reach the solidus composition, as shown in Figure 2.2b. However, since the overall concentration of B is well below its solubility limit in A, B continues to diffuse into the core, which decreases the amount of B in the liquid. Because the concentration of B is fixed by an equilibrium condition, this results in the decrease in the amount of liquid, allowing isothermal solidification to take place (Figure 2.2c). This solidification stage is typically the rate-limiting step of the joining process, as it depends on the solid-state diffusion of B in A. Therefore, a MPD with a high diffusivity-solubility product must be selected to minimize solidification times. Once all of the liquid has disappeared, further annealing would result in homogenization of the interlayer (Figure 2.2d). In contrast to TLP bonding of metals, the MPD diffuses *into* the interlayer, rather than *out* of the interlayer, which significantly reduces the diffusion distance needed for complete homogenization to occur. The resulting joint has a melting point, T_{melt}, which is significantly higher than T_{bond}. This enables TLP bonds to operate at higher temperatures than brazed joints produced at the same bonding temperature.

As was the case in metal-metal TLP bonding, designing a successful interlayer system requires a thorough understanding of the interrelationships between the processing conditions, interlayer microstructure, and joint properties. TLP bonding of ceramics is, in some ways, simpler than TLP bonding of multi-component, multiphase alloys, because the ceramic is often not involved in the dissolution and solidification processes. Thus, the interlayer materials combinations may also be less complex (e.g., binary systems). A similar exercise to the one shown in Figure 2.2 using a binary phase diagram can often be useful in guiding the selection of an appropriate interlayer system. Ideally, an interlayer materials combination should have a melting-point minimum, such as a eutectic point, or a low cladding melting point, enabling the TLP to form at relatively modest temperatures. The TLP should also dissolve some of the core-layer metal and the saturated liquid should be in equilibrium with the MPD-saturated single-phase core metal (rather than an intermetallic phase). This allows the formation of a sufficient amount of liquid to fill interfacial gaps, even with thin cladding layers, and hence, a small amount of MPD. In most systems, minimizing the overall concentration of MPD

maximizes the interlayer re-melt temperature. Such a system would also avoid the formation of intermetallics, which can degrade the joint properties. Lastly, the MPD solubility in the core must be sufficiently high over a wide temperature range to prevent precipitation of secondary phases either during cooling or in service.

Kinetic considerations must also be taken into account when designing TLP interlayers. As mentioned previously, the isothermal-solidification stage is limited by the solid-state diffusion rate of the MPD in the core-layer metal. Thus, it is ideal to choose an MPD that has a high diffusivity. An adequately high bonding temperature must be chosen to allow rapid diffusion, but the maximum allowable bonding temperature is limited by processing costs and the types of materials (i.e., temperature at which microstructural degradation occurs) being joined. While selecting an interlayer system with these aforementioned solution thermodynamic and kinetic properties does not necessarily ensure that adequately strong bonds will form, these considerations are essential in selecting possible interlayer materials that allow favorable bonding conditions.

With any joining method, the mechanical properties of the resulting joints depend on the interfacial flaw size and population,[5,115] formation of secondary phases, and residual stresses due to thermal-expansion-coefficient mismatches. In liquid-phase bonding, the interfacial-flaw distribution is dependent on how well the liquid fills both large-scale gaps between the parts being joined and small-scale asperities on the faying surfaces. In order for the liquid to spontaneously flow into interfacial gaps, the sum of the two contact angles formed on the joining surfaces must be <180°.[116] When brazing ceramic parts using a non-reactive liquid metal, this condition is typically not satisfied (Figure 2.3a) and the liquid does not flow into interfacial gaps. However, when joining two metallic parts, this condition is easily satisfied, as shown in Figure 2.3b, since liquid metals typically form low contact angles on solid-metal surfaces. As discussed in *Section 2.2.1*, metallization of the ceramic surfaces or the addition of reactive metals has been used to braze ceramics, but metallization requires high-temperature processing prior to joining, and the use of active-metal brazes may result in the formation of a brittle, interfacial-reaction layer, which, in excess, can degrade joint strengths. In TLP bonding of ceramics, the liquid forms between the metallic core layer and the ceramic. Thus, even a typical non-reactive liquid metal can form contact angles that sum to <180°, as shown in Figure 2.3c. To eliminate local voids, however, it is still advantageous for the liquid to form contact angles <90° on each faying surface. This allows the liquid to fill surface asperities and results in the formation of less stable pores that have higher driving force for size reduction.[116]

Interfacial reactions may also drastically affect the joint properties. For instance, if a reactive metal is used as an interlayer constituent, the wetting behavior of the liquid would improve and allow the interfacial flaws to reduce in size and population, but brittle reaction layers may form and degrade bond strengths.[4,117] The formation of intermetallic[118] or spinel[115,119-121] phases along the interface may also decrease fracture strength and toughness. Intermetallic phases typically form from reactions between the cladding and core-layer metals, while spinel phases may form in the presence of an oxygen source, which could originate from the joining environment, the ceramic being joined (e.g., glassy phase in Al_2O_3), or the metal itself (dissolved O).[115,119,120,122]

Lastly, residual stresses due to thermal-expansion-coefficient mismatches, which have the effect of pre-loading the joints, may be detrimental if the ceramic is in a tensile stress state. In conventional brazing, the interlayer metals typically have higher thermal-expansion coefficients than their ceramic counterparts. When the interlayer is cooled, it will contract more than the ceramic, which puts the ceramic in compression along the interface. Since ceramics are much less susceptible to

fracture under compression, such a scenario is advantageous over cases where the metal has a lower thermal-expansion coefficient than the ceramic. While lower-melting-point fcc metals have higher thermal-expansion coefficients than Al_2O_3, some refractory bcc metals can have much lower thermal-expansion coefficients (Figure 2.4). In terms of thermal-expansion matching for joining Al_2O_3, V, Ta, and Nb appear to be preferable choices as interlayer materials amongst high-melting-point metals.

In the current study, Ni/Nb/Ni and Co/Nb/Co interlayers are used to join high-purity Al_2O_3 blocks. As demonstrated in the aforementioned example, the binary phase diagrams are very useful in determining the feasibility of the interlayer-materials combination for TLP bonding. The Ni-Nb binary phase diagram (Figure 2.5)[123] shows that a liquid can form at the eutectic point at 1175°C, which is significantly below the melting points of Ni and Nb. When the system is heated above the peritectic temperature (1291°C), the Nb-saturated liquid is in equilibrium with the Ni-saturated Nb. In the Co-Nb phase diagram (Figure 2.6),[124] it can be seen that the Co/Nb/Co interlayer forms a liquid at a modest temperature (1237°C), and above 1374°C, the Nb-saturated liquid is in equilibrium with the Co-saturated Nb solid. Furthermore, both binary systems form Nb-rich liquids, suggesting relatively thick liquid films would form from thin Ni or Co cladding layers.

In previous TLP bonding studies,[5,115,125] the interlayers consisted of materials that do not form any stable intermetallic compounds, i.e., form complete solid solutions for all compositions or have a miscibility gap over a wide temperature range. These systems were intentionally chosen to avoid the formation of brittle phases. However, there are only a few binary systems with such characteristics, and thus, systems with more complex equilibrium phase relationships, such as the Ni-Nb and Co-Nb systems, must be explored.

2.2.4 Previous Studies on Ceramic-Ceramic TLP Bonding

Previous studies on TLP bonding of ceramics have demonstrated its effectiveness in producing joints with high service temperatures and high mechanical reliability at reduced bonding temperatures. In Iino's earlier study,[118] Ni-Nb multilayer interlayers were used to join Si_3N_4 at 950°C, which is much lower than the bonding temperatures typically needed for diffusion bonding Si_3N_4. It was recognized that liquid does not form in this process, but the interdiffusion of Ni and Nb allowed reasonably strong bonds to form. However, Ni-Nb intermetallic phases formed along the interfaces, consistent with the Ni-Nb phase diagram (Figure 2.5).[123] This study then led to Iino's development of Ni-Ti-based interlayers to join Si_3N_4, where a sufficiently high bonding temperature (1050°C) was used to form TLP layers between the ceramic and the Ni core layer. Although not mentioned, it was likely that these joints contained Ti-nitride layers, TiNi, and $TiNi_3$ phases along the interface.[126] The presence of Ti can improve wetting and adhesion on ceramic surfaces, but the formation of brittle reaction layers can degrade the mechanical properties of the joints, similar to the observations made in active-metal brazing.

Glaeser *et al.* conducted more detailed studies of TLP bonding using various interlayer materials combinations. As explained earlier, an ideal interlayer for TLP bonding should form a liquid that is in thermodynamic equilibrium with the single-phase core metal to avoid the formation of brittle intermetallic phases. The Cu/Pt/Cu,[5] Cu/Ni/Cu,[115] Cu/Nb/Cu,[119,120] and other interlayers,[125,127] which at the bonding temperatures exhibit such a characteristic, were used to join Al_2O_3. For example, the Cu-Ni phase diagram shows that the two metals are mutually soluble above 354°C.[128] Thus, when joined at 1150°C for 6 h, the interlayer consisted of a single-phase solid solution containing 94% Ni, with no intermetallic phases or reaction layers. These interlayer systems have favorable phase-equilibrium relationships for TLP bonding, allowing bonds to be produced at

moderate temperatures. However, the fracture strengths of some of these joints were significantly below the bulk Al_2O_3 fracture strength (≈280 MPa average). Samples bonded with a Cu/Pt/Cu interlayer exhibited an average four-point-bend flexural strength and standard deviation of 160±55 MPa,[5] while those produced using Cu/Ni/Cu interlayer yielded 160±63 MPa.[115] The fracture surfaces of the samples bonded with Cu/Pt/Cu and Cu/Ni/Cu interlayers showed some regions were well bonded, with the metal side containing imprints of the ceramic surface. However, there were other regions that suggested no contact was made between the Al_2O_3 and the interlayer due to the TLP dewetting.[5,115]

One possible approach to improve bond strengths is to expose the samples to a post-bonding anneal. Annealing allows the interlayer to chemically homogenize, potentially reducing any thermal-expansion gradients, and may lead to the reduction of interfacial flaw size and population.[5] Annealing in different environments may also change the interfacial chemistry, which can drastically affect the joint strengths. With the Cu-Pt system, higher bond strengths (217±44 MPa) were obtained when the joints were annealed in air at 1000°C for 10 h. Shalz explained that when the joints were annealed in air, O diffusion through the Cu-Pt alloy along the metal-ceramic interface may result in internal oxidation of Cu. The Cu oxide and Al_2O_3 then reacted to form a strong chemical bond, which increased the bond strengths. When the joints were annealed in Ar, however, the samples failed during routine handling. The fracture surfaces revealed evidence of Cu-Pt alloy dewetting along the interface.[5] When the samples bonded with Cu/Ni/Cu were annealed in Ar or air at 1000°C for 10 h, the strengths decreased relative to the as-bonded samples in both cases due to spinel phase formation along the interfaces.[115]

Bond strengths are also dependent on the wetting behavior of the liquid and how effectively the liquid fills interfacial gaps and asperities on the joining surfaces. Although the Cu/Ni/Cu interlayer showed potential to produce joints with high strengths (267 MPa), the majority of the test samples failed at significantly lower loads. The low average bond strength and wide strength distribution were attributed to the poor wetting behavior of the liquid, resulting in incomplete metal-ceramic contact. Similar to active-metal brazing, the wetting behavior of the TLP can be improved by incorporating a reactive metal. For example, wetting experiments have shown that an addition of 6% Cr to Cu decreased the contact angle from the 115° for pure Cu on Al_2O_3 to 67° at 1150°C.[25] Cr was added to the interlayer either through the deposition of a thin (≈10 nm) pre-coat on the Al_2O_3 prior to Cu film deposition, or the use of 80Ni-20Cr core layer. Many of the beams joined with the Cr pre-coat exhibited fracture strengths >200 MPa, but the majority of the samples still yielded strengths that ranged between 50–150 MPa. This resulted in no change in the average strength, but a wider variation in strength was observed, which suggested that there was not enough Cr to sufficiently improve wetting and adhesion at the metal-ceramic interfaces.[125] When Cu/80Ni-20Cr/Cu interlayer was used to join Al_2O_3, the average strength increased to 227 MPa and the standard deviation decreased to ±19 MPa.[125,129] This result shows that stronger TLP bonds can be produced when the liquid forms a lower contact angle on the ceramic. However, since the wetting at the liquid-core metal interface provides an additional driving force for capillary flow (compared to conventional brazing), as shown in Figure 2.3, a liquid with a moderately low contact angle (≈90°) on the ceramic may still be sufficient. Such a system is less likely to form a brittle reaction layer, but still form a strong metal-ceramic interface. Many alloys with Ti additions, for instance, form contact angles <40° on Al_2O_3, but also react to produce TiO_x layers.[24,44,130] Furthermore, it should be noted the contact angle of the TLP may be drastically different from that of the molten cladding metal, as the TLP dissolves some of the

core layer. For this reason, the contact angles of Ni-Nb liquid close to the liquidus composition have been measured to characterize the Ni/Nb/Ni interlayer system currently being studied.

TLP bonding has also been used to join other ceramics, such as Si_3N_4 and SiC. Compared to Al_2O_3, both Si_3N_4 and SiC have significantly lower coefficients of thermal expansion. To reduce the residual stresses from thermal-expansion mismatch, a thin (25 μm) Ni core layer was used.[125] Since Si_3N_4 and Ni can react at ≈1170°C, it was also desirable to minimize the bonding temperature. When Si_3N_4 was joined using a Cu-Au/Ni/Cu-Au interlayer, with ≈4 at.% Ti added to the cladding layers, at 950°C for 2 h, an average bend strength of 770±200 MPa was measured. The joint strength was comparable to the bend strength of the bulk Si_3N_4 (960±110 MPa), but the scatter was significantly larger.[129] Similarly, when SiC was joined using the same interlayer, the average bend strength was 260±130 MPa, which was significantly lower than that of the bulk SiC (420±30 MPa).[125] Si_3N_4 was also joined using Au/Ni-22Cr/Au interlayer at 1000°C for 4 h, which produced an average fracture strength of 272 MPa. While this was much lower than the bulk Si_3N_4 fracture strength (770 MPa), slight increases in the average strength (288 MPa) and Weibull modulus (2.5 vs. 3.9) were observed after a 60-h post-bonding anneal at 800°C. It was determined that an optimum bond strength would be achieved when an 8-μm thick CrN reaction layer formed along the interface, which would require a post-bonding anneal up to 1000 h at 800°C.[131]

In one of the more recent studies, TLP bonding with commercial Ag-Cu active brazing alloys (Cusil-ABA®, Ticusil®) was explored in joining Al_2O_3 at temperatures (600°–700°C)[117,127] well below typical brazing temperatures associated with these alloys (>800°–900°C). Both Cusil-ABA and Ticusil are Ag-Cu eutectic alloys containing 1.75 wt.% and 4.5 wt.% Ti, respectively. When the In/Cusil-ABA®/In interlayer was used to join high-purity, high-strength Al_2O_3 (average flexural strength = 359±52 MPa) at 700°C for 1.5 h, a relatively high average strength (276 MPa) was accompanied by a high standard deviation (±102 MPa). When In/Ticusil®/In interlayer was used to join the same type of Al_2O_3, an average fracture strength of 350±45 MPa was obtained. Although Ticusil® contains a higher Ti concentration, the majority of the Ti resides between Ag-Cu-eutectic layers. In contrast, Cusil-ABA® contains small Ti-rich particles that are randomly distributed within an Ag-Cu matrix. The increase in strength observed when Ticusil® was used in place of Cusil-ABA® can be attributed to the more uniform core-layer surface of Ticusil® being in contact with the TLP. While much less Ti was incorporated in the liquid with the Ticusil® core layer (since liquid is only in contact with Ag- and Cu-rich phases), the Ti concentration was uniform throughout the solid-liquid interface. This likely allowed the liquid to distribute more uniformly, but further experimental work will be needed to observe the differences in the liquid distribution in the In-Ticusil® and In-Cusil-ABA® pairs. This work does show that the core-layer microstructure can also affect the liquid distribution and the resulting joint properties.

Liquid-film-assisted joining (LFAJ), a derivative of TLP bonding, was also developed by Glaeser. LFAJ uses a Cu/Nb/Cu multilayer interlayer, which forms thin liquid films between the Al_2O_3 and the Nb core layer, similar to the interlayers used in TLP bonding. In TLP bonding, the liquid must distribute to fill interfacial gaps, and then isothermally solidify. In LFAJ, the Cu-rich liquid film dewets the interface to form discrete Cu particles that solidify during cooling. While this may appear counterintuitive at first, the liquid essentially functions as a high-diffusivity pathway for Nb to bond with the Al_2O_3. This allows the system to replace the Cu/Nb and Cu/Al_2O_3 interfaces with the more energetically favorable Nb/Al_2O_3 interface as the Cu liquid dewets. When high-purity Al_2O_3 blocks were bonded at 1400°C for 6 h, an average fracture strength of 359±26 MPa was

obtained. High-temperature fracture tests also showed that, despite the presence of Cu, which melts at 1085°C, the joints exhibited fracture strengths >200 MPa at 1200°C.[119] Although at 1200°C, the Cu melted along the interface, high bond strengths were still retained because the discrete Cu particles were surrounded by Nb-Al_2O_3 interface. Since LFAJ does not require the liquid to isothermally solidify, it has the potential to produce strong, reliable joints with significantly shorter bonding times than TLP bonding. The presence of a dewetting liquid is also not an issue because the liquid must simply provide a high-diffusivity pathway for the core metal to make contact with the ceramic. High-temperature four-point bend tests revealed that, despite the presence of residual Cu particles, the joints maintained useful strengths at temperatures above the Cu melting point. Despite these advantages, LFAJ may only be applied to a limited number of materials combinations that have little or no mutual solubility in the solid-state, and some solubility of the core metal in the liquid.

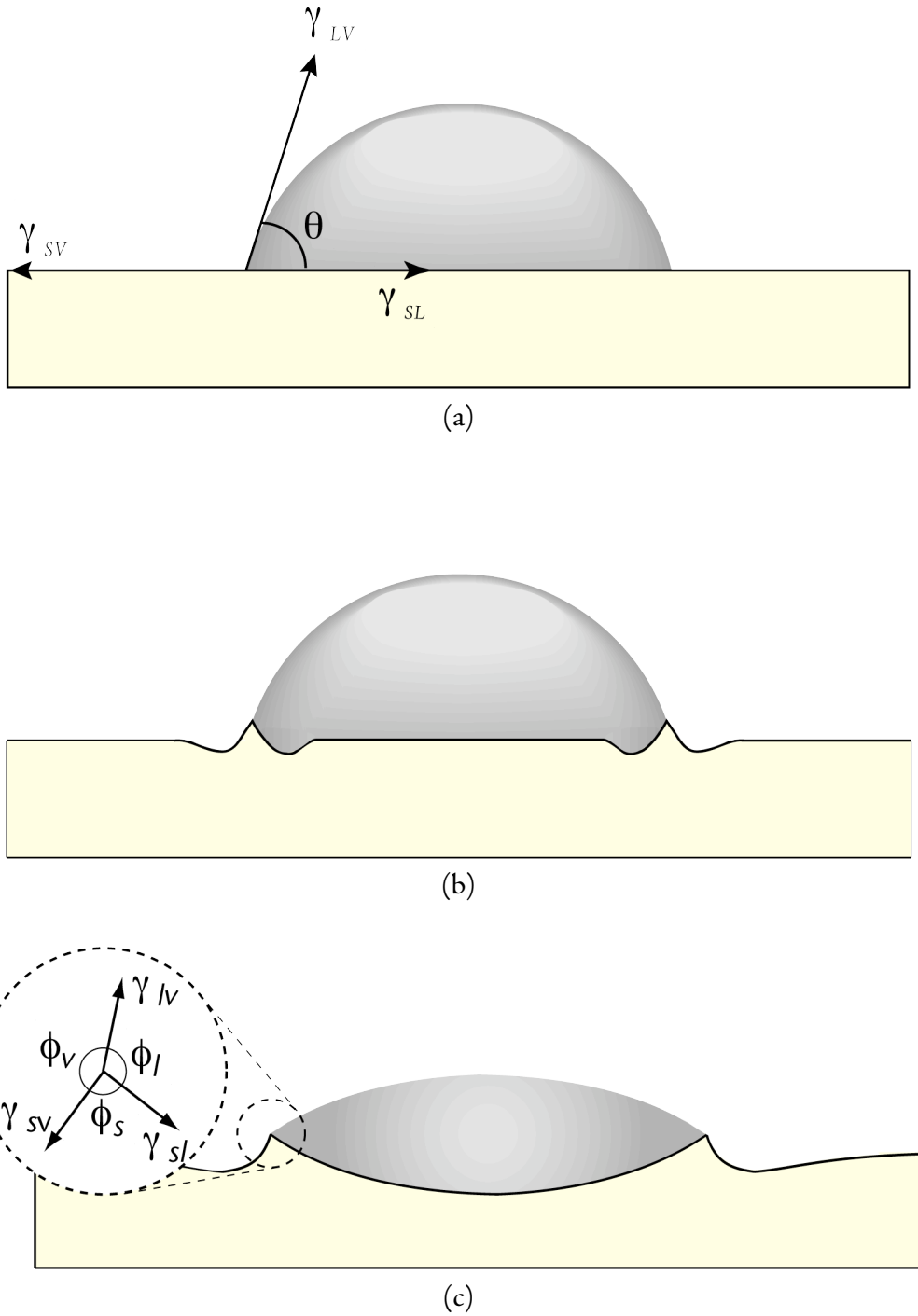

FIGURE 2.1 Schematic of (a) metastable, (b) local equilibrium at the triple junction, and (c) local and total equilibrium along the solid-liquid interface of liquid droplet on solid substrate.[14]

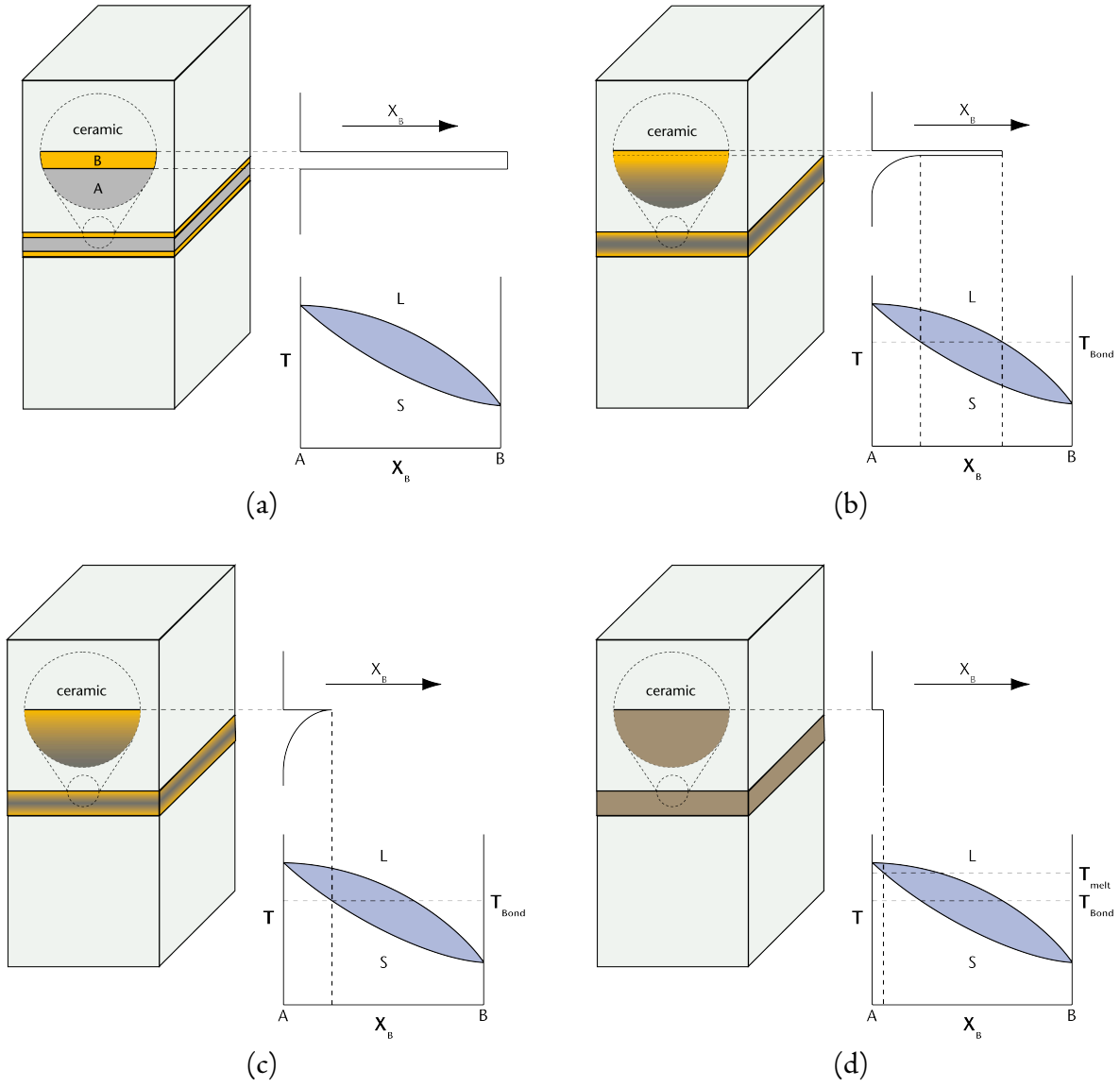

FIGURE 2.2 Schematic of TLP bonding process. (a) Initial bonding assembly with multilayer interlayer consisting of thin cladding layers (B) on either side of thick core layer (A); (b) Assembly is heated to T_{bond}, resulting in the formation of TLP; (c) Diffusion of B into A results in isothermal solidification; (d) Homogenized interlayer has a solidus temperature that is significantly higher than T_{bond}.

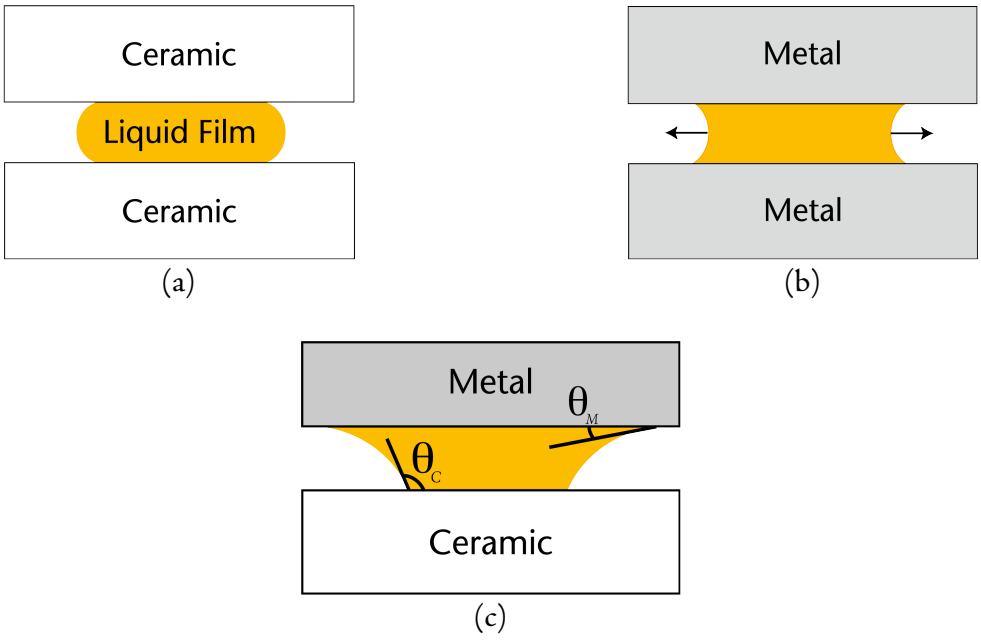

FIGURE 2.3 Illustration of liquid distribution in conventional brazing and TLP bonding. (a) When a non-reactive liquid metal is used to braze two ceramic parts, the sum of the two contact angles formed on the two faying surfaces is >180°. (b) When joining two metallic parts, the sum of the contact angles is <180°. (c) In TLP bonding, the liquid forms in contact with the ceramic and the metallic core layer surfaces, making it possible for the sum of the contact angles to be <180° even for non-reactive liquid metals.

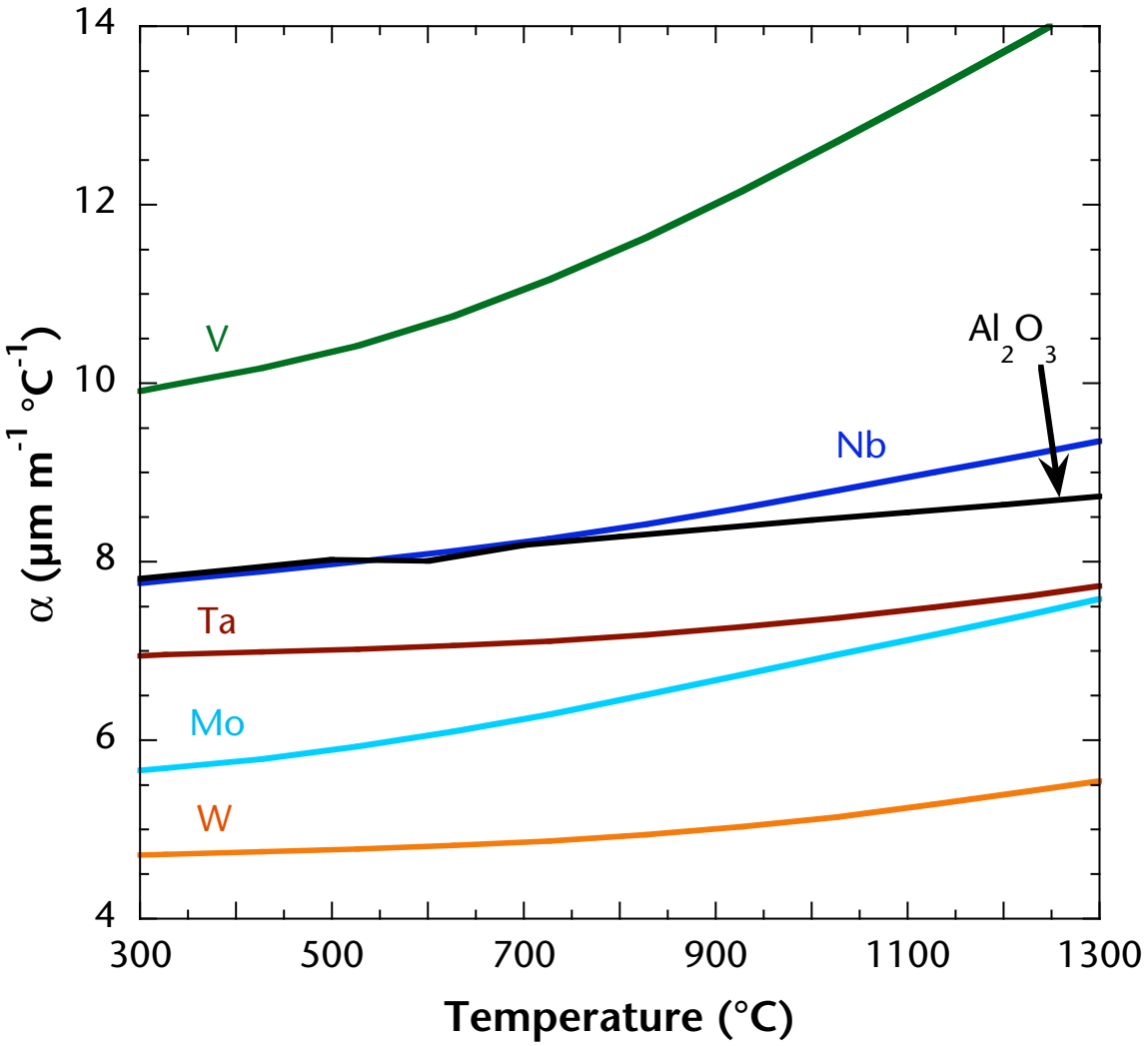

FIGURE 2.4 Plot of coefficients of thermal expansion of bcc refractory metals, and Al_2O_3 as functions of temperature.[132]

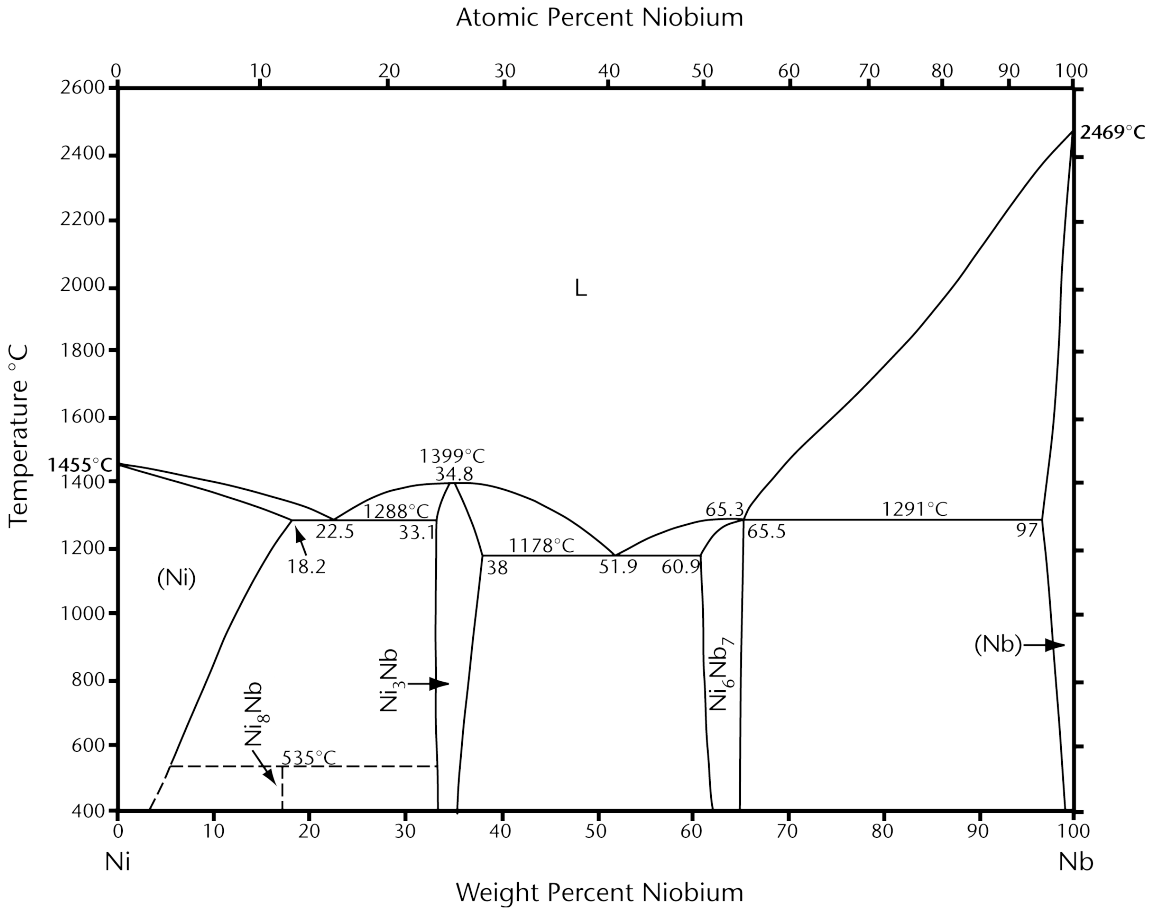

FIGURE 2.5 Ni-Nb binary phase diagram.[123]

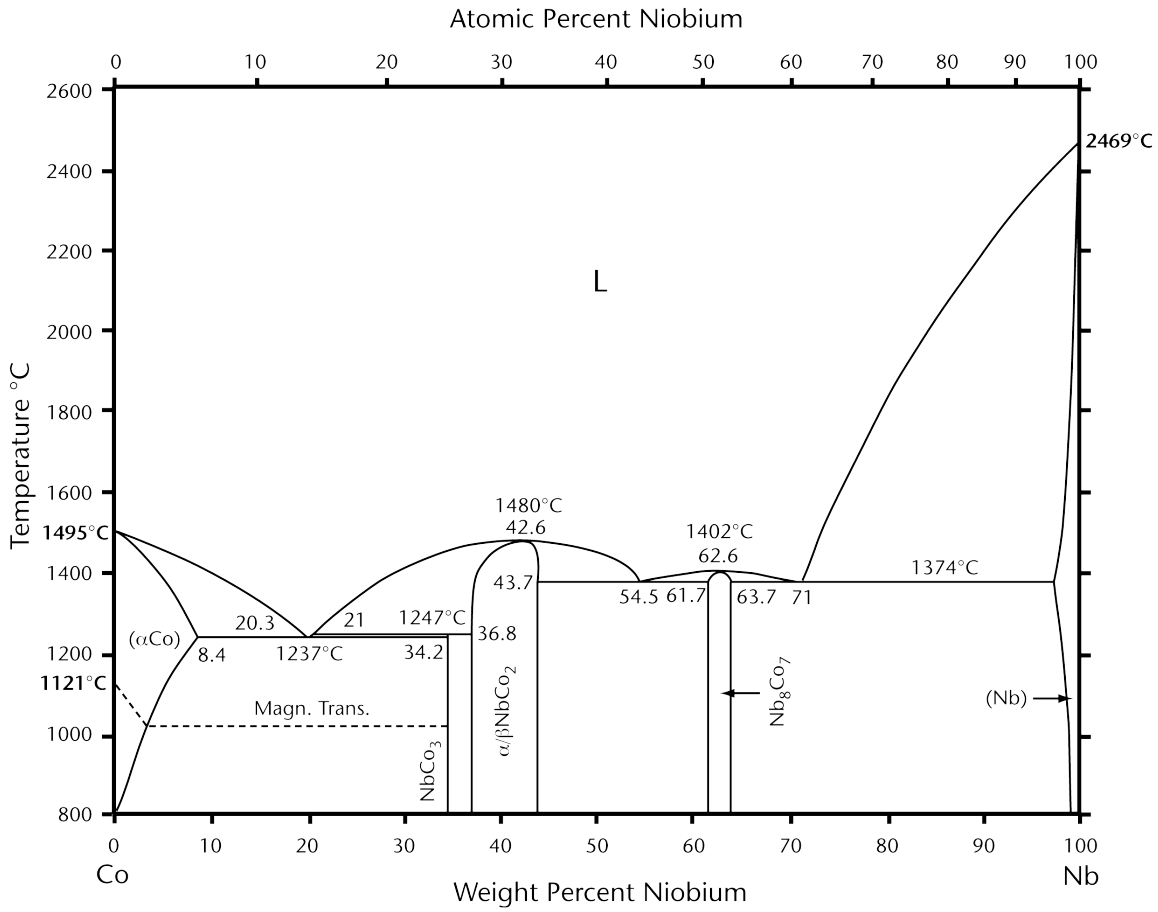

FIGURE 2.6 Co-Nb binary phase diagram.[124]

3. Experimental Procedures

3.1 Al_2O_3 Blocks

Polycrystalline Al_2O_3 blocks of 98% density and 99.9% purity (SSA-999W Nikkato, Osaka, Japan), with dimensions of 20 mm × 20 mm × 20 mm were joined. A hot-isostatically pressed version of the same material (SSA-999S) with the same dimensions was used to produce higher-strength samples. One surface of each block was ground with a surface grinder using a 400-grit (37-μm) diamond wheel. The blocks were then polished with an automatic polisher (Logitech Ltd, Glasgow, Scotland) in subsequent steps with 9-μm, 6-μm, 3-μm, and 1-μm diamond suspension solutions, and 0.02-μm colloidal silica. The polished surfaces were used as joining surfaces, which minimized surface flaws to ensure good contact with the metal layer. The polished blocks were ultrasonically cleaned in distilled water and soap, distilled water, acetone, and isopropyl alcohol for ≥15 min in each solution, in the order listed. The blocks were then dried with a hot-air gun and annealed in air for 1 h at 1000°C to remove any residual organics.

3.2 Nb Core Layer

Nb foil of 99.9% purity (Goodfellow, Cambridge Ltd., Devon, PA) and 125-μm thickness was cut into ≈20 mm × 20 mm pieces to match the dimensions of the Al_2O_3 blocks being joined. To reduce large-scale curvatures, the sectioned foils were flattened between two polished stainless-steel plates using a vice. The foils were then ultrasonically cleaned in distilled water and soap, distilled water, acetone, and isopropyl alcohol for ≥15 min in each solution in the sequence listed.

Nb core layers with finer grain sizes were also used in interlayers to study the effects of core-layer grain size on the isothermal-solidification time. Foils with smaller grain sizes were produced by rolling 1-mm thick, 99.9%-pure Nb foils with a rolling mill to ≈130 μm. The rolled foils were then sectioned into ≈20 mm × 20 mm pieces. Some of the foils were joined as-rolled, while others were annealed at 1000°C for 1 h in Ar-2%H to induce recrystallization prior to joining.

3.3 Cladding-Layer Deposition

Ni wire of 99.98% purity (Goodfellow Cambridge Ltd., Devon, PA) or Co wire of 99.995% purity (Alfa Aesar, Ward Hill, MA) was used as the source for cladding-layer deposition. The wires were cut into four 0.5-mm pieces that weighed ≈0.60 g total and ultrasonically cleaned in distilled water and soap, distilled water, acetone, and isopropyl alcohol. Thin oxide layers on the wires were then stripped by dipping them in Aqua Regia (3:1 HCl:HNO_3) solution for 10-15 s. The wires were rinsed in distilled water, and in isopropyl alcohol, and then dried with a hot-air gun. The cleaned wires were loaded in a pair of Al_2O_3-coated W-wire baskets in a thermal-evaporation deposition system (Mikros, Inc., Portland, OR). The deposition chamber was pumped down overnight to $\approx 7 \times 10^{-7}$ torr prior to coating.

In previous studies of TLP bonding, the cladding layers were deposited directly onto the polished Al_2O_3 surfaces to be joined. This allowed coating of two cladding layers (on either side of the core layer) without breaking vacuum. However, when Ni or Co was deposited directly onto the Al_2O_3 blocks, the films spalled off due to high residual stresses in the films. Thus, Ni or Co was deposited onto each side of the Nb foils. This required breaking vacuum between each run, but ensured the production of uniform cladding layers. Examining the cross-sectioned foils in a scanning-electron microscope (SEM) revealed that the resulting films were ≈2 μm thick.

3.4 Joining

Various joining conditions were used to study the effects of bonding temperature, time, and applied pressure. A schematic diagram of the joining assembly is shown in Figure 3.1a. Either SSA-999W or SSA-999S Al_2O_3 blocks were joined using Ni/Nb/Ni interlayers in a graphite-element hot press furnace (Thermal Technology, Inc., Santa Rosa, CA) at 1400°C with holding times of 5 min, 30 min, and 6 h, and a constant 2.4-MPa applied pressure. The furnace was heated at 4°C/min and cooled at 2°C/min. A computer controller was set to control the temperature, time, and applied pressure. The chamber was pumped down overnight to $<7 \times 10^{-6}$ torr and the pressure was kept below 8×10^{-5} torr throughout the heating cycle. Joints using Co/Nb/Co interlayers and SSA-999W Al_2O_3 were also bonded in the same hot press at 1400°C and 1500°C with 30-min holding times. Both the heating and cooling rates were identical to prior runs, and a 2.4-MPa pressure was also used.

Samples were also fabricated using a much lower applied pressure by using a small weight, rather than the hydraulic press in the hot press because 2.4 MPa was the minimum bonding pressure that can be applied in the hot press with the given sample dimensions. As before, SSA-999W or SSA-999S Al_2O_3 blocks were bonded with Ni/Nb/Ni interlayer. The bond was made in a W-element vacuum furnace (Centorr Vacuum Industries, Nashua, NH), which maintained a vacuum pressure $\approx 2 \times 10^{-5}$ torr. The sample was, again, heated at 4°C/min, soaked at 1400°C for 6 h, and cooled at 2°C/min. A 6.7 kPa load was applied by placing an Al_2O_3 crucible containing ≈270 g of Mo-wires on top of the sample. To ease loading of the assembly into the furnace, the sample and the weight were placed in a larger Al_2O_3 crucible.

Diffusion experiments were also conducted to measure the effects of Nb grain size on the Ni-concentration profiles. SSA-999W Al_2O_3 plates that were machined from the blocks were polished and cleaned in the same manner as the blocks, and then joined using Ni/Nb/Ni interlayers with as-rolled, or recrystallized (rolled and annealed) Nb foils. These foils were prepared by cold rolling 1-mm thick, 99.9%-pure Nb to ≈130–150 μm. The recrystallized foils were obtained by annealing the rolled foils in Ar-2% H_2 environment at 1000°C for 1 h. These samples were bonded in the hot press using the same heating cycle and applied pressure, as described earlier.

3.5 Fracture Testing

The joined blocks were sectioned into four ≈4–5-mm thick plates using a diamond saw blade, as illustrated in Figure 3.1b. The sectioned plates were then ground with a 400-grit diamond wheel on both faces of the plates to 3-mm thickness. When machining bonds made with SSA-999S Al_2O_3 blocks, the 400-grit wheel was used to grind the plates to ≈3.2-mm thickness, and then an 800-grit wheel was used to grind one of the surfaces to reduce the thickness to 3 mm. This was done to minimize both subsurface and surface flaws introduced by grinding, which should aid in obtaining the highest fracture strengths possible. The ground plates were polished using an automatic polisher (Logitech Ltd, Glasgow, Scotland) in subsequent steps with 9-μm, 6-μm, 3-μm, and 1-μm diamond suspension solutions, and 0.02-μm colloidal silica. The polished surfaces served as the tensile faces of the fracture-test beams.

The polished plates were then sectioned into four beams with 3 mm × 3 mm cross-sectional dimensions, as shown in Figure 3.1b. The edges adjacent to the polished faces of the beams were beveled using a rotating 3000-grit (6-μm) diamond plate, and then polished using 1-μm diamond solution and 0.02-μm colloidal silica on rotating polishing pads. Greater care was used in preparing the high-strength material (SSA-999S Al_2O_3) to eliminate flaws on the tensile faces and edges. The beams were then dipped in ink, which penetrated surface and edge flaws to facilitate visual inspection

for flaws under an optical microscope. If a beam contained any large flaws (typically along the tensile edges), it was re-polished using colloidal silica. Just prior to mechanical testing, the beams were wiped with acetone and lint-free tissue, and ultrasonically cleaned in distilled water and soap, acetone, isopropyl alcohol, and ethanol. The beams were then dried using a hot-air gun. To compare with the fracture strengths of the joined Al_2O_3, monolithic Al_2O_3 beams were also subjected to the same mechanical test. In view of the potential microstructural changes in the Al_2O_3 during processing, monolithic Al_2O_3 plates were also annealed to match the thermal cycles of the bonded blocks. These plates were polished and machined into beams in the same manner as the bonded plates.

Four-point bend tests using a mechanical tester (Instron, Canton, MA) and a fully articulating four-point-bend-test jig were conducted to determine the load vs. displacement relations of the bonded and monolithic beams at room temperature. The cleaned beams were placed polished face (tensile face) down in the testing jig, configured with a 9-mm inner span and a 25-mm outer span, as illustrated in Figure 3.2. Although it would be ideal to align the interlayers of the bonded beams exactly at the center of the inner span, because a four-point-bend configuration yields a constant bending moment within the inner span, slight offset in the interlayer position was not expected to affect the results (in contrast to a three-point-bend configuration). The articulating jig also compensated for any small dimensional differences and allowed all four pins to contact the beam. The lowest crosshead speed allowed by the instrument, 0.05 mm/min, was used.

3.6 Microscopy and Chemical Analysis

Optical and scanning-electron microscopes were used to observe the microstructures of the bonded interlayers. Optical images were captured using a high-resolution digital camera. The samples were sectioned into small pieces that included the entire interlayer and placed in epoxy. The epoxy-encased samples were ground using an automatic grinder, then polished by hand using 30-μm, 15-μm, 6-μm, 3-μm, and 1-μm diamond pastes, and colloidal silica in the order listed. The polished interlayers were preferentially etched by swabbing a 3:1:1 (by vol.) $C_3H_6O_3$ (lactic acid):HNO_3:HF solution for 5–10 s to reveal the Nb grain boundaries. However, because the Nb grains appeared larger than the interlayer thickness, it was difficult to assess the grain sizes. Thus, the bonded Ni/Nb/Ni interlayers were also observed in the plane parallel to the bonded surfaces. As shown in Figure 3.3, this was done by sectioning the joined region using a low-speed saw from a beam and grinding the excess Al_2O_3 from one side of the interlayer until the metal surface was exposed. The interlayer was then etched and observed in both the optical microscope and the SEM.

Electron-probe microanalysis (EPMA), which is accurate to ≈0.01 wt.%, was used to measure the interlayer compositions. Due to the relatively low concentrations of Ni or Co, it was necessary to use an acceleration voltage of 20 keV, which yielded a spatial resolution (i.e., excitation width) of ≈3 μm. Reference signals were established using high-purity Al_2O_3, Ni, or Co, and Nb samples. Backscatter electron images were also captured, which did not produce sharp, high-resolution images with the given beam conditions, but provided contrast between some Nb grains and any Ni-Nb intermetallic phases.

3.7 Wetting Experiments

As discussed in the previous chapter, the wetting behavior of the TLP has a large effect on the mechanical properties of the joints. It should be stressed that the liquid composition differs from the initial cladding-layer composition, as the liquid dissolves the core layer and reaches the liquidus composition. Therefore, in this work, sessile-drop experiments were used to measure the contact

angles of Ni-Nb (50:50 [by weight]) alloys on Al_2O_3 substrates at 1400°C. The 50:50 composition was chosen because it is close to the eutectic composition at which the liquid initially forms, and it melts at a temperature (1178°C) below the maximum furnace temperature of ≈1400°C. The alloy was produced by mixing high-purity metal powders and melting them in an Al_2O_3 crucible in an inert gas (Ar-2%H) furnace at 1600°C. The composition of the alloy was specifically chosen near the eutectic composition to measure the contact angle of the liquid that forms initially during the bonding process. Once the alloy was cooled and solidified, it was sectioned into small pieces (≈1.5–2 mm diameter) using a low-speed saw.

The Al_2O_3 substrates for sessile-drop experiments were approximately 10 mm × 10 mm × 1 mm. These plates were polished and cleaned in the same manner as the Al_2O_3 blocks that were joined. A small piece of the alloy was placed on top of an Al_2O_3 substrate and loaded in a high-vacuum, W-element furnace. The furnace consists of a Mo stage for the sample and a quartz window to allow *in-situ* measurements of the wetting angle, as illustrated in Figure3.4a. The furnace was heated at 30°C/min to 1400°C and soaked for 30 min while a digital camera was used to capture images of the droplet on the substrate in 30-s intervals. The same experiments were performed using 99.995%-pure *c*-plane sapphire substrates. The sectioned pieces of the alloys were typically smaller than the diameter of the melted droplets, resulting in the liquid front spreading outwards to form "advancing" contact angles. "Receding" contact angles were measured by melting cold-pressed multilayer foils with the same overall compositions as the 50:50 Ni-Nb alloy. This allowed liquid to retract and form droplets with smaller footprints than the initial foil. The contact angles were obtained using a computer program, which fit the droplets into a circle to estimate the contact angle, or by manually measuring the angles on either sides of the droplet and averaging them. The cross-sectioned droplets were also examined in the SEM and optical microscope, and its chemical composition was determined using an energy-dispersive x-ray spectrometer (EDS) on the SEM.

Drop-transfer experiments were conducted to measure the contact angle of the liquid NiNb alloy on Nb. For this experiment, a piece of 50:50 NiNb alloy was placed on an Al_2O_3 plate on the Mo stage of the furnace. Because a sufficiently thick Nb plate was unavailable, a 1-mm thick Nb plate was bonded to an Al_2O_3 plate using a thin Ni cladding layer in a vacuum furnace at 1400°C for 6 h prior to the wetting experiment. The Nb substrate was secured onto the drop-transfer apparatus, as shown in Figure 3.4b. The furnace was heated to 1250°C (maximum temperature allowed by the drop-transfer apparatus), allowing the alloy to melt on the Al_2O_3 substrate. Once the alloy fully melted and the droplet was stabilized, the Nb substrate was lowered until it made contact with the droplet. A high-speed video camera was used to capture the Nb substrate making contact with the liquid and the liquid spreading onto the Nb at 2000 frames per second (fps). Advancing and receding contact angles were also obtained in this setup by displacing the top substrate up and down from the contact height. A similar experiment was conducted to measure the advancing and receding contact angles on Al_2O_3 by placing an Al_2O_3 substrate, rather than a Nb substrate, onto the drop-transfer apparatus.

3.8 Diffusion Calculation

A diffusion calculation method was developed to estimate the time needed for isothermal solidification and homogenization of the MPD. This calculation was based on analytical solutions to Fick's second law. Similar to prior studies in modeling the kinetics of conventional metal-metal TLP bonding, this calculation divided the bonding sequence into two discrete stages: an isothermal-solidification stage and an MPD-homogenization stage.[78,79] It was deemed unnecessary to calculate the

time for the dissolution stage because previous modeling studies on metal-metal TLP bonding have shown it to be several orders of magnitude shorter than the solidification and homogenization stages.[79] Since the liquid layers in ceramic TLP bonding are much thinner than in TLP bonding of metals, the time needed for the dissolution stage is expected to be less than a few seconds.

In the isothermal-solidification stage, it was assumed that liquid layers with essentially negligible thicknesses were in equilibrium with the Nb core layer. Thus, the Ni concentration at the solid-liquid interface was fixed at the solidus composition while the liquid was present. Using this assumption, the solution for fixed surface source was superimposed to account for Ni diffusion from both sides of the core layer,

$$C_{iso}(x,t) = C_{\circ}\left\{\left[1-erf\left(\frac{x}{2\sqrt{D_{app}t}}\right)\right]+\left[1-erf\left(\frac{1-x}{2\sqrt{D_{app}t}}\right)\right]\right\} \tag{3.1}$$

where C_o is the surface concentration, which is fixed at the equilibrium solidus composition at the joining temperature, D_{app} is the apparent diffusivity, and l is the total thickness of the interlayer. D_{app} was estimated using published values of the lattice (D_l) and grain boundary (D_{gb}) diffusivities of Ni in Nb,[133,134] segregation coefficient, s, the grain boundary width, δ, and the average grain size, d, with the expression,

$$D_{app} = D_l + \frac{s\delta}{d}D_{gb} \tag{3.2}$$

The isothermal-solidification time was then determined iteratively by matching the calculated amount of Ni diffused into the core layer with the amount measured in the joined samples.

Once the isothermal-solidification time and the corresponding concentration profile was determined, another solution to Fick's equation[135] was used to determine the homogenization behavior

$$C_{homo}(x,t) = \frac{1}{l}\int_0^l C_{iso}(x',t_{iso})dx' + \frac{2}{l}\sum_{n=1}^{\infty}\exp\left(-\frac{D_{app}n^2\pi^2 t}{l^2}\right)\cos\left(\frac{n\pi x}{l}\right)\int_0^l C_{iso}(x',t_{iso})\cos\left(\frac{n\pi x'}{l}\right)dx' \tag{3.3}$$

where $C_{iso}(x',t_{iso})$ is the Ni concentration profile after complete solidification given by Eqn. 3.1. This solution basically uses the concentration profile found in the first part of the calculation as the initial concentration profile, and then confines diffusion within two impermeable surfaces on either side of the foil. Further description of this calculation will be presented in the Results and Discussion chapter.

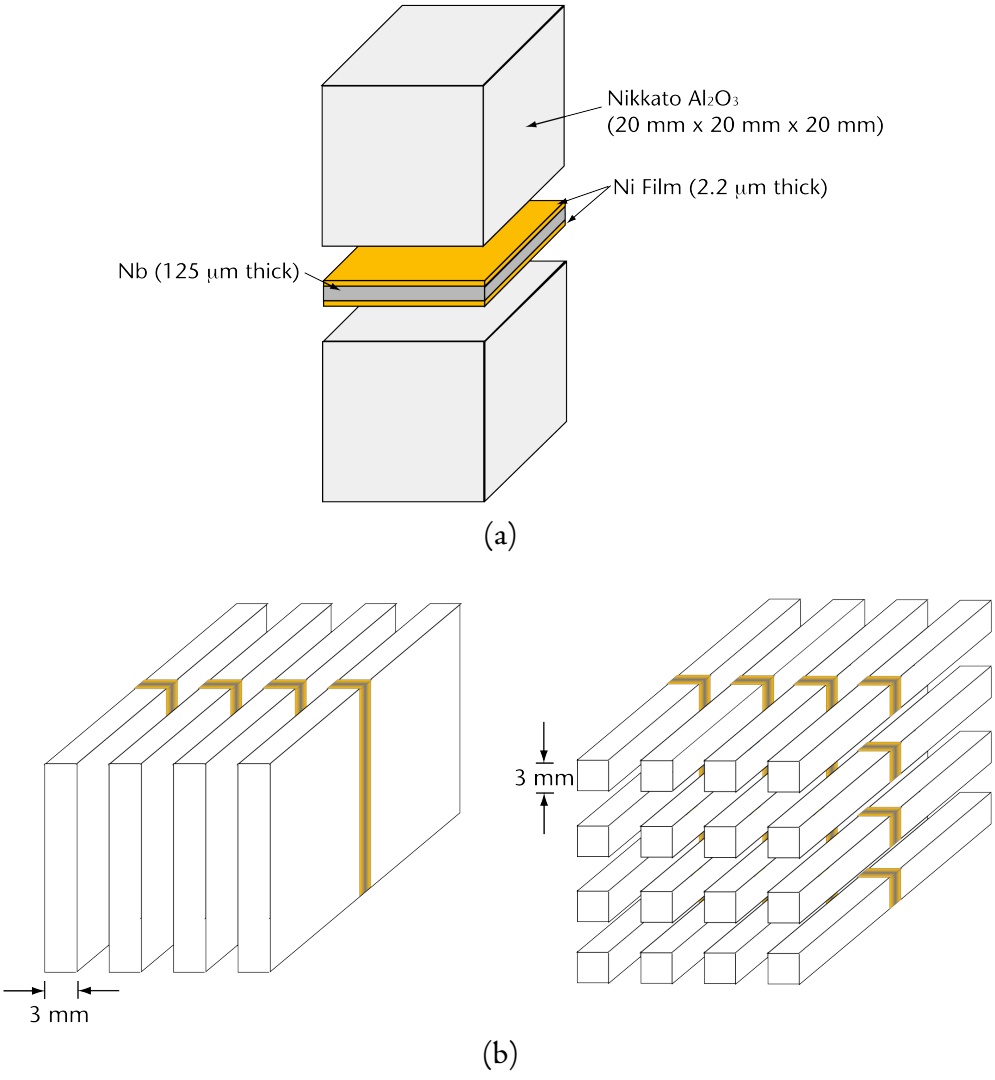

FIGURE 3.1 (a) Schematic of TLP joining assembly with Ni/Nb/Ni interlayer. (b) Joined blocks are machined into plates, which are then sectioned into beams to be used as four-point-bend-test specimens. The beams have dimensions 3 mm × 3 mm × 40 mm.

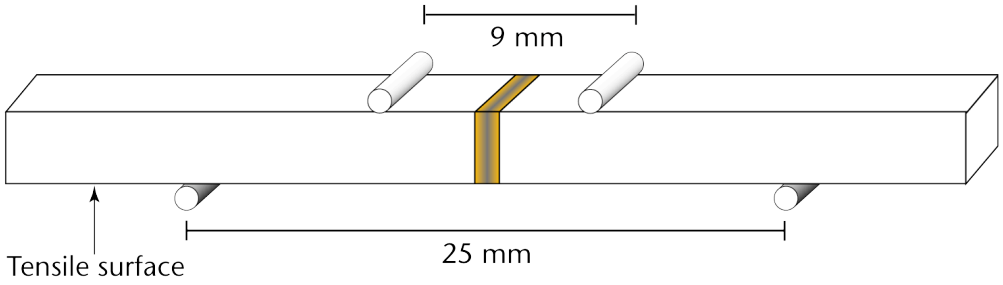

FIGURE 3.2 Illustration of four-point-bend-test geometry. The inner span is 9 mm and the outer span is 25 mm.

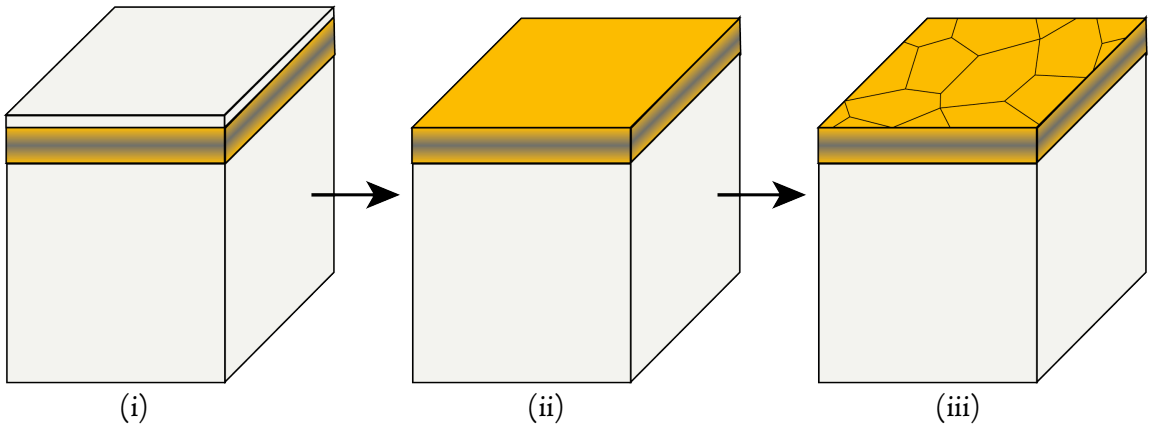

FIGURE 3.3 (i) Interlayers were sectioned from beams. (ii) Excess Al_2O_3 was ground off to expose the metal surface parallel to the interface. (iii) Exposed metal surface was polished and then chemically etched to reveal its grain boundaries.

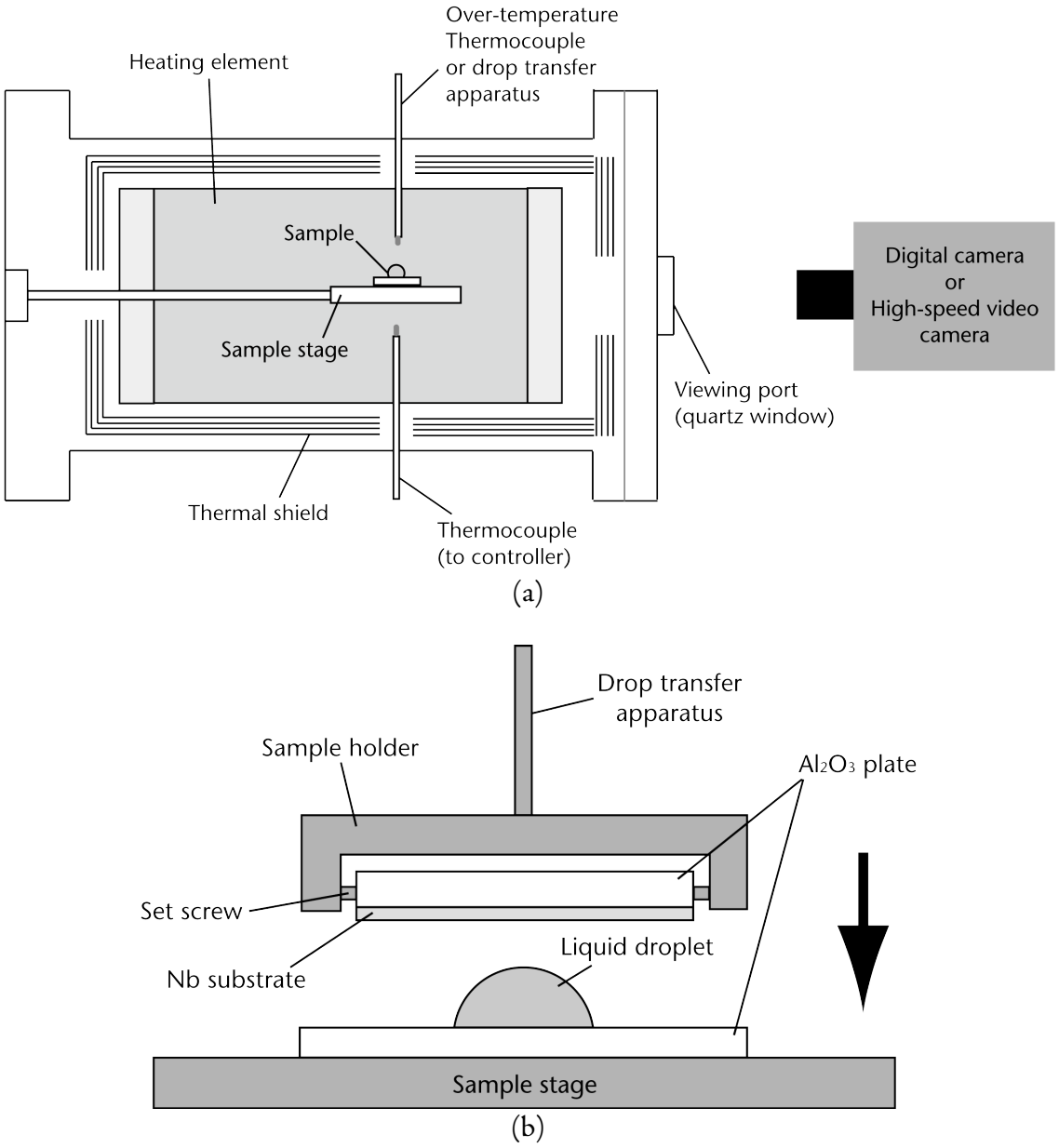

FIGURE 3.4 (a) Cutaway view of high-temperature wetting furnace. (b) Schematic of the drop-transfer apparatus, which is inserted in place of the over-temperature thermocouple in the wetting furnace.

4. Results and Discussion

4.1 Fracture-Strength Data

4.1.1 Bulk Al_2O_3

Fracture strengths were measured for both the as-received and annealed (1400°C for 5 min, 30 min, and 6 h) bulk Al_2O_3 to obtain the upper limits of fracture strengths expected for the bonded Al_2O_3. Bulk Al_2O_3 plates were annealed to match the bonding conditions to observe the effects of heat treatment on the fracture strengths. The as-received SSA-999W Al_2O_3 exhibited an average fracture strength of 359±32 MPa (average strength ± standard deviation), while those annealed for 5 min, 30 min, and 6 h yielded 349±37 MPa, 331±36 MPa, and 337±40 MPa, respectively. The small standard deviations indicate that the distributions of these fracture strengths are relatively small, and are reflected by the relatively high Weibull moduli of 12, 9.8, 9.5, and 8.3, for the as-received, and 5 min, 30 min, and 6 h anneal samples, respectively. Figure 4.1a shows the fracture probability vs. fracture strength relationships.

Similar experiments were conducted for the hot-isostatically pressed, bulk SSA-999S Al_2O_3. The as-received materials exhibited an average fracture strength of 500±116 MPa, and a Weibull modulus of 4.4. The samples annealed at 1400°C for 5 min, 30 min, and 6 h yielded average fracture strengths of 530±119 MPa, 535±92 MPa, and 560±83 MPa, and Weibull moduli of 4.1, 6.1, and 6.6, respectively. The fracture probability vs. fracture strength plot is shown in Figure 4.1b.

From these fracture probability plots, it can be deduced that the heat treatments had minimal effects on the fracture strengths of these materials. However, it is of note that the SSA-999S Al_2O_3 had significantly higher average fracture strengths, but exhibited lower Weibull moduli than the SSA-999W Al_2O_3. Furthermore, when the SSA-999W Al_2O_3 was subjected to heat treatment, the average strengths decreased when the anneal times were increased, while the opposite trend was observed for the SSA-999S Al_2O_3.

4.1.2 Al_2O_3/Ni/Nb/Ni/Al_2O_3 Joints

Four-point bend tests were also used to measure the fracture strengths of the joined Al_2O_3 to determine the relationship between the fracture strength and the processing conditions. When SSA-999W Al_2O_3 blocks were bonded at 1400°C with a 2.4-MPa bonding pressure, average fracture strengths of 343±44 MPa, 462±53 MPa, and 342±28 MPa were obtained for samples made with 5-min, 30-min, and 6-h holding times, respectively. The Weibull moduli of the joined samples were 8, 6, and 13, for the 5-min, 30-min, and 6-h samples, respectively. The fracture probability vs. fracture strength plot is shown in Figure 4.2a. The filled gray area in Figure 4.2a represents the range of fracture strengths of the bulk SSA-999W Al_2O_3 found in Figure 4.1a. In all fracture tests of joints, the fracture paths were recorded for each specimen, i.e., interfacial or ceramic fracture. Figure 4.2a shows that all but one beam failed in the ceramic, indicating that the fracture strengths of the joints matched or exceeded those of the bulk Al_2O_3.

The joints made with 5-min and 6-h holding times exhibited similar fracture strengths as the as-received and annealed bulk Al_2O_3 (Figure 4.1a). This result was expected since the joined samples failed predominantly in the ceramic. In contrast, the 30-min sample exhibited much higher average fracture strength than the bulk Al_2O_3 annealed for 30 min at 1400°C. Figure 4.1a shows that the fracture strength of the monolithic Al_2O_3 decreases slightly when the material is annealed for a longer time, which is expected, since samples exposed to a longer anneal have larger grains. However, it is yet unknown why the joints made with 30-min holding time yielded much higher fracture strengths,

particularly since all beams fractured in the ceramic. It is possible that the joined Al_2O_3 blocks used with the 30-min bonding time contained smaller internal flaws, perhaps due to variations in the manufacturer's processing conditions.

In an attempt to measure the true fracture strengths of the bonds, the Ni/Nb/Ni interlayer was used to join SSA-999S Al_2O_3 using the same processing conditions. The samples produced with 5-min, 30-min, and 6-h isothermal holding times yielded average fracture strengths of 513±119 MPa, 522±96 MPa, and 523±63 MPa, respectively. As with the monolithic SSA-999S Al_2O_3, higher average strengths were attained, but the standard deviations were larger. Again, the wider strength distributions are reflected by the lower Weibull moduli of 3.3, 4.8, and 8.9, respectively. Figure 4.2b shows that the fracture probability vs. fracture strength relationships of the joined Al_2O_3 are very similar to those of the as-received and annealed reference Al_2O_3.

Unlike the SSA-999W Al_2O_3 bonds, several beams joined with 5-min and 30-min holding times failed in the interface, but none of the beams from the 6-h bonds exhibited interfacial failures. 31% of the 5-min samples and 16% of the 30-min samples failed in the interface. However, it should be noted that nearly all interfacial failures resulted in fracture paths that meandered along the interface and in the ceramic near the interface. Two beams from the joints made with 5-min holding times did not fracture completely through the sample because fracture occurred on both sides of the interlayer simultaneously, and propagated partially through the interface and into the metal interlayer, where the crack arrested (*see insert in* Figure 4.2a). Based on the fracture strength alone, these results suggest that the processing conditions are nearly optimized.

4.1.3 Al_2O_3/Ni/Nb/Ni/Al_2O_3 Joints Fabricated Using Lower Bonding Pressure

In large-scale commerical applications, optimization of the bonding temperature, time, and pressure are essential in minimizing costs. Although the effects of bonding temperature and time are well studied in liquid-phase bonding processes, including previous works on TLP bonding, the role of bonding pressure have not been explored to the same extent. In principle, TLP bonding should not require a high bonding pressure since it involves the formation of liquid layers, which fill interfacial gaps and voids. With a high bonding pressure, both long-wavelength and short-wavelength roughness features on the interlayer surfaces can plastically deform to make intimate contact with the ceramic surfaces and thereby decrease the interfacial void volume. However, when the bonding pressure is decreased, the interfacial gap width increases, which increases the amount of liquid required to fill interfacial gaps. If an insufficient bonding pressure is used, larger interfacial gaps will be present, thus requiring more liquid to fill the gaps. Simply increasing the initial cladding-layer thickness can increase the amount of liquid formed, but this can result in longer isothermal-solidification time, or intermetallic formation during cooling, if the overall MPD concentration exceeds the solubility limit in the core metal. To explore the effects of bonding pressure, Al_2O_3 blocks were joined using Ni/Nb/Ni interlayers using a 6.7-kPa bonding pressure.

When the lower bonding pressure was used in joining SSA-999W Al_2O_3 blocks at 1400°C for 6 h, the resulting joint yielded an average fracture strength of 324±23 MPa, and a Weibull modulus of 14.3. As shown in Figure 4.3a, the fracture strengths are nearly identical to the samples bonded in the hot press (2.4-MPa pressure). However, 25% (4 of 16) of the beams failed in the interface, compared to just 6% (1 of 16) of the beams joined in the hot press. Still, the majority of the beams failed in the ceramic when a substantially lower bonding pressure was used.

As with the bonds produced in the hot press, higher-strength SSA-999S Al_2O_3 blocks were joined to observe the effects of a lower bonding pressure on the actual bond strengths. Four-point

bend test yielded an average fracture strength of 400±68 MPa, with a Weibull modulus of 5.8. The highest strength recorded was 504 MPa. The use of the higher-strength Al_2O_3 subjected the joints to higher loads, resulting in 62.5% (10 of 16) of the beams failing in the interface. Figure 4.3b shows that the interfacial failures occurred over a wide range of loads. Compared to the annealed reference SSA-999S Al_2O_3 and the samples bonded in the hot press, these joints exhibited much lower fracture strengths, but a similar Weibull modulus. Combined with the higher fraction of beams that failed at the interface, the use of a lower bonding pressure decreased the fracture strengths of the joints.

4.1.4 Al_2O_3/Co/Nb/Co/Al_2O_3 Joints

As discussed in *Section 2.3.3*, there are many key similarities between the Ni-Nb and Co-Nb phase diagrams (see Figure 2.5 and 2.6). The literature also shows that the Co lattice diffusivity in Nb ($\approx 3.0 \times 10^{-10}$ cm^2 s^{-1}) is very similar to that of Ni in Nb ($\approx 4.3 \times 10^{-10}$ cm^2 s^{-1}) at 1400°C.[133] Given the success of the Ni-Nb interlayer system, the Co-Nb pair also appeared to be a viable candidate for TLP bonding interlayer. When SSA-999W Al_2O_3 blocks were bonded using a Co/Nb/Co interlayer at 1500°C for 30 min with a 2.4-MPa bonding pressure and subjected to four-point bend fracture tests, an average fracture strength of 274±38 MPa with a Weibull modulus of 7.3 was measured. Fracture test specimens were also produced by joining at 1400°C for 30 min, which resulted in an average strength of 306±28 MPa and a Weibull modulus of 11. A comparison of the fracture probability vs. fracture strength between the samples made using Co/Nb/Co interlayers and those using Ni/Nb/Ni interlayers is shown in Figure 4.4.

As was the case with beams bonded with Ni/Nb/Ni interlayers, the majority of those bonded with Co/Nb/Co interlayers fractured in the ceramic. The 1500°C, 30-min bond had lower fracture strengths than the 1400°C, 30-min bond and the reference monolithic Al_2O_3. This may be attributed to increase in residual stresses from larger thermal contraction mismatch upon cooling from 1500°C, or introduction of flaws during sample preparation. The pore size and population in the Al_2O_3 may also vary from sample to sample, resulting in slight variations in the fracture strengths. It should be noted that the fracture strength of the bulk SSA-999W Al_2O_3 decreased slightly with increased anneal time at 1400°C, thus, the drop in the fracture strength of the samples bonded at 1500°C appears to be consistent. When compared to the beams joined with Co/Nb/Co interlayer, the specimens joined with Ni/Nb/Ni at 1400°C for 30 min had significantly higher fracture strengths. However, this large discrepancy in the fracture strength appears to be an anomaly and does not reflect the actual effects of heat treatment on the fracture strengths of the joints.

4.2 Interlayer Chemistry and Microstructure

4.2.1 Ni/Nb/Ni Interlayers

The microstructure and composition of the interlayer is closely related to the phase-equilibrium relationships of the interlayer constituents, and affects the resulting thermal and mechanical properties of the joints (*see Section 2.3.3*). Both optical and scanning electron microscopy were used to study the interlayer microstructure, and EPMA was conducted to measure the interlayer chemical compositions. The Ni-Nb phase diagram (Figure 2.5) shows that the Ni/Nb/Ni interlayers processed at 1400°C should form a Nb-rich liquid, which isothermally solidifies as Ni diffuses into Nb. It was estimated that the initial pair of 2-μm thick Ni cladding layers deposited on a 125-μm thick Nb foil corresponded to an overall Ni concentration of ≈4.5 at.%. The initial Ni concentration nearly coincides with the Ni solubility limit in Nb at 1400°C. In principle, this means that given

sufficient time for diffusion, the liquid should fully solidify isothermally, without the formation of any intermetallics along the interfaces.

Optical images of the cross-sectioned Ni/Nb/Ni interlayers after joining at 1400°C using a 2.4-MPa bonding pressure are shown in Figures 4.5a–c. These micrographs show that the interlayers are free of any secondary-phase particles or layers. This indicates that the TLP has completely solidified isothermally and not during cooling, resulting in a single-phase Nb interlayer. The results of EPMA, shown in Figure 4.6, confirmed that the interlayers had low Ni concentrations (average concentration <1 at.%) even in the samples joined with a 5-min isothermal holding time. The Ni concentration profiles show that the interlayers of the 5-min and 30-min bonds did not fully homogenize and have Ni concentration gradients. In contrast, the interlayer bonded with a 6-h isothermal holding time appeared to be fully homogenized. It is important to note that the peak Ni concentrations along the interfaces of the 5-min and 30-min samples are still well below the Ni solubility limit in Nb, and thus, the joints are expected to have re-melt temperature ≈2200°C. Figure 4.6 also shows that the measured Ni concentrations are much lower than the total amount of Ni from the initial cladding layers deposited onto the Nb foils (<1 at.% vs. ≈4.5 at.%). The significant loss of Ni is likely due to excess liquid flowing out of the joints, as evidenced by solidified metallic beads along the edges of the joints.

To observe the near-interfacial compositions and microstructures in more detail, Dr. McKeown used a transmission electron microscope (TEM) to obtain a higher-resolution bright-field image of the metal-ceramic interface joined at 1400°C for 30 min, as shown in Figure 4.7a. Compared to the SEM used for EPMA, which has a spatial resolution of ≈3 μm (i.e., the excitation volume width), the TEM produced much higher resolution images, which show that there are no secondary-phase particles or layers at the interface. Chemical composition maps of the interfacial region were also generated using an EDS, as shown in Figure 4.7b-e. The EDS results reveal that the Ni concentration remains low throughout the interfacial region. The circle in Figure 4.7b highlights a small region with high Ni concentration, but this may be an aberration due to thickness variations in the sample. Even if this feature is actually a Ni-rich phase, it is a discrete, 0.1-μm particle, and thus, should not adversely affect the mechanical and thermal properties of the joint.

As discussed in *Section 2.3.2*, in metal-metal TLP bonding, the grain structures of the parent metal may play a significant role on the isothermal solidification and homogenization rates. Similarly, the microstructure of the core layer in multilayer interlayers may have a similar influence on the bonding kinetics. Polishing and chemical etching revealed the grain structures of the joined Ni/Nb/Ni interlayers, which were then observed in the optical microscope, as shown in Figures 4.5a–c. As a reference, the as-received Nb foil was also etched and characterized – the average grain size of the as-received Nb foil was ≈10 μm (Figure 4.5d). It is clear from Figure 4.5 that after joining at 1400°C, the Nb grains become much larger; interlayers contained grains that appeared larger than the interlayer thickness. To accurately measure the interlayer grain sizes, the joint regions were sectioned from the beams and any residual Al_2O_3 was removed by grinding to reveal the interlayer grain structure in the plane parallel to the interface. Figures 4.8a–c are optical micrographs of the polished and etched interlayers in plan view. The average grain sizes of the joints produced using 5-min, 30-min, and 6-h holding times were approximately 130 μm, 180 μm, and 520 μm, respectively. For reference, when an as-received Nb foil was annealed at 1400°C for 20 h, the average grain size was ≈23 μm. The polished surfaces of these interlayers contained randomly scattered "rough" and faceted features, such as the one highlighted in Figure 4.8c. There were some initial concerns that these

features were very thin intermetallic phases, but EDS revealed low Ni concentrations in these regions. Given their highly faceted appearance and the lack of any compositional differences, it is possible that these features correspond to etched dislocations. Similar microstructure was observed in Hillert's study of diffusion-induced grain-boundary migration in the Fe-Zn couple.[136] Hillert determined that these walls of dislocations formed to compensate for any lattice misfit due to the presence of Zn in the Fe lattice. Likewise, in the current system, these features may be dislocations due to the misfit caused by Ni atoms in the Nb lattice.

4.2.2 Effects of Lower Bonding Pressures on Interlayer Chemistry and Microstructure

When the interlayers of the joints produced using lower bonding pressures were observed in the optical microscope, it was immediately obvious that there were secondary-phase layers along the interfaces, as shown in Figure 4.9. Figure 4.9a shows a region near the sample edge and reveals continuous, ≈10-μm-thick intermetallic layers along the interfaces. In contrast, Figure 4.9b shows that in the regions away from the sample edges, the intermetallic layers appear much thinner and discrete, and reside primarily in the grain-boundary grooves. The non-uniform intermetallic-layer thickness is an indication of varying liquid-layer thickness caused by non-uniform interfacial gap widths. Prior to joining, it was observed that the Nb foil had a large curvature that spanned the entire edge dimension of the foil in one direction, as well as some local plastically deformed regions along the foil edges. Despite cold pressing the foil prior to joining, with the lower bonding pressure, the interlayer was not sufficiently flattened against the Al_2O_3 surfaces, resulting in larger gap widths. In regions where wider interfacial gaps existed (primarily along the sample edges), more liquid was present, which solidified under cooling to form continuous intermetallic layers. Furthermore, the beams sectioned near one of the edges all fractured along the interfaces at significantly lower loads (average strength ≈310 MPa). The EPMA results, as shown in Figure 4.10, revealed that the composition of the secondary phase coincided with the liquidus composition at 1400°C on the Ni-Nb phase diagram (Figure 2.5). This suggests that these layers/particles consist of a two-phase mixture of Ni_6Nb_7 and Nb, which is consistent with solidification during cooling. The interlayer microstructure reveals why a higher percentage of samples failed at the interface, and the average fracture strength decreased compared to the samples bonded with the higher pressure when SSA-999S Al_2O_3 blocks were joined. Formation of the Ni_6Nb_7 phase also decreases the interlayer re-melt temperature significantly (1290°C), thus, decreasing its maximum allowable service temperature.

Figures 4.9a and b also show that the grain boundaries intersecting the interfaces grooved to balance the interfacial forces at the triple junctions. In liquid-rich regions, the grooves were much deeper, and in some cases, the liquid penetrated tens of microns along grain boundaries (Figure 4.9a). In the liquid-depleted regions, the liquid penetrated only a few microns and was essentially trapped in the grooved features on the Nb surface (Figure 4.9b). The grain structure of the interlayer was revealed by chemical etching, as shown in Figure 4.9b. In contrast to the samples shown in Figure 4.5, some grain boundaries in Figure 4.9b appear to have varying curvatures, likely due to diffusion-induced grain-boundary migration.[136] This indicates that the grain boundaries of the samples bonded with the lower pressure likely contained higher Ni concentrations than those of the samples bonded with the higher pressure.

The formation of intermetallic layers also indicates that a 6-h isothermal holding time at 1400°C was insufficient for complete isothermal solidification to occur. The required time for complete isothermal solidification can be reduced by depositing thinner Ni cladding layers, which

would reduce the amount of liquid formed during bonding. However, using a lower bonding pressure leads to larger interfacial gaps that require more liquid to fill. Thus, to use a low bonding pressure, further optimization of the cladding-layer thickness, surface roughness, and bonding time would be necessary to produce strong, reliable joints consisting of single-phase interlayers. Such optimization processes may be facilitated by a model that calculates the isothermal-solidification times for a given liquid-film thickness, as will be presented in *Section 4.4.1*.

4.2.3 Co/Nb/Co Interlayers

The joints made with Co/Nb/Co interlayers all fractured in the ceramic in the four-point bend tests. Given a very similar equilibrium phase relationship as the Ni-Nb pair, it was expected that the Co/Nb/Co interlayer would have a similar microstructure to the Ni/Nb/Ni interlayers. Optical microscopy revealed that the interlayer produced at 1400°C consists of a single Nb-rich layer with no precipitates or intermetallic layers, similar to the Ni/Nb/Ni interlayer processed using the same conditions. Similar interlayer microstructure was found in the samples bonded at 1500°C. Chemical analysis of the 1400°C sample, in Figure 4.11, shows that the peak Co concentration is below the Co solubility limit in Nb, and the average concentration (≈1 at.%) is well below the initial Co concentration (≈4 at.%) corresponding to two 2-μm thick cladding layers. As expected, Figure 4.11 shows that the 1500°C sample has a lower peak concentration (≈1.4 at.%) and higher centerline concentration than the 1400°C sample. With these low Co concentrations, the re-melt temperatures of these interlayers are expected to approach 2000°C. As was the case with the Ni/Nb/Ni interlayer, the lower Co concentration is likely due to the TLP flowing out of the joints, resulting in significant Co loss. This suggests that excess liquid forms during bonding, and thus, thinner Co cladding layers may be employed.

4.2.4 Interfacial Fracture Surfaces

Optical microscopy was used to observe the fracture surfaces of beams that failed at the interfaces. The majority of the beams made with Ni/Nb/Ni interlayers using a 2.4-MPa bonding pressure failed in the ceramic, with fracture strengths similar to those of the reference Al_2O_3. It was thus concluded that the fracture strengths of the joints matched or exceeded those of the bulk Al_2O_3. The fracture surfaces revealed that when a crack initiated at the interface, it typically propagated away from the interface and into the ceramic, or more commonly, the crack initiated both at the interface and in the ceramic on the tensile surface. The ceramic and metal fracture surfaces of a beam bonded at 1400°C for 5 min are shown in Figures 4.12a and b. Nearly all beams recorded as interfacial failures, in fact, consisted of fracture that partially initiated at the interface, and then propagated into the ceramic. Of these beams, two contained cracks that initiated on opposite sides of the interlayers, and then propagated toward each other, through the interlayer. Figure 4.13 shows a set of macroscopic images representing the four faces of such fracture test specimen. These samples did not fracture completely, and instead, the primary crack arrested as the metal layer partially tore and plastically deformed to blunt the crack tip. The large interlayer deformation then led to multiple cracks propagating into the ceramic, away from the interface (Figure 4.13d). Although it was reported that 31% of the SSA-999S Al_2O_3/Ni/Nb/Ni/SSA-999S Al_2O_3 joints bonded at 1400°C for 5 min failed in the interface, none of the beams fractured solely through the interface. Similar conclusion can be made regarding the samples made with a 30-min holding time.

The four-point-bend tests of the joints made of the high-strength SSA-999S Al_2O_3 showed that the percentage of interfacial failures decreased when longer bonding times were employed. Although optical microscopy and chemical analyses of these samples suggest that all the joints made at 1400°C consisted of nearly identical interlayer microstructures (i.e., single-phase Nb with no intermetallic phase), the fracture test results suggest that there may have been differences in the interfacial flaw size and population. Since a 5-min bonding time was sufficient for complete isothermal solidification, any additional bonding time represents a regime in which interfacial flaws are removed through solid-state diffusion.

As mentioned previously, a higher fraction of beams fabricated using a 6.7-kPa bonding pressure fractured along the interface. The interlayers of these samples contained intermetallic layers due to solidification of the TLP during cooling. These brittle intermetallic layers likely reduced fracture strengths. The fracture surfaces of a beam that fractured along the interface, as shown in Figure 4.14, indeed, demonstrate that the fracture propagated through the intermetallic layer and did not deviate into the ceramic. A large area fraction of the ceramic side of the fracture surface (Figures 4.14a and c) consists of the intermetallic layer (brighter regions) that remained attached to the Al_2O_3 surface. However, there are still some regions where the Al_2O_3 surface is visible (darker regions). The metal side (Figures 4.14b and d) appears quite similar to the ceramic side because it consists of the opposite side of the fractured intermetallic layer. Other regions show imprints of the Al_2O_3 surface, but it is unclear whether these areas are due to separation of the Al_2O_3-intermetallic or the Al_2O_3-Nb interface.

Lastly, the fracture surfaces of Al_2O_3/Co/Nb/Co/Al_2O_3 bonds were also examined using an optical microscope. These samples exhibited fracture strengths similar to those of the bulk Al_2O_3 annealed at 1400°C for 30 min, and only one beam failed along the interface. As shown in Figure 4.15, the fracture initiated both in the ceramic and the interface on the tensile surface, then propagated along the interface. The majority of the ceramic side of the fracture surface is the bare Al_2O_3 surface, with a few, ≈100-μm wide patches of metal tear-outs. The metal side of the fracture surface is largely made up of the Al_2O_3 surface imprint, along with Al_2O_3 fragments. With the exception of the large ceramic fragment found in Figure 4.12, the fracture surface shown in Figure 4.15 appears quite similar to the samples joined with Ni/Nb/Ni interlayer.

4.3 Wetting

4.3.1 Sessile-Drop Experiments

Ceramics are difficult to join using conventional brazing largely due to poor wetting of most liquid metals on ceramics. Metallization and active-metal brazes have been used to join Al_2O_3, but the former requires high-temperature processing prior to joining, while the latter typically forms brittle interfacial reaction layers. As discussed, the multilayer-interlayer design in TLP bonding promotes better wetting and liquid redistribution. With this multilayer-interlayer setup, the liquid films form and locally redistribute to minimize interfacial energies. If the contact angles on the two joining surfaces sum to >180°, the liquid film will tend to dewet and form discrete droplets along the interface. In contrast, if the contact-angle sum is <180°, the liquid should remain between the ceramic and the core layer until it isothermally solidifies. While most non-reactive liquid metals form contact angles <130° on ceramics and <50° on metals, it has been shown that stronger, more reliable TLP bonds are produced when the liquid forms a relatively low contact angle on the ceramic surface.[129] This enables the liquid to flow into microscopic and local surface asperities, and eliminate interfacial voids.

In the current study, a Ni/Nb/Ni interlayer has been used to join high-strength, high-purity Al_2O_3. The exceptional fracture strengths and the nearly flaw-free interfaces suggest that the liquid was able to wet the Al_2O_3. According to the Ni-Nb phase diagram, Figure 2.5, a eutectic liquid (Ni-48Nb by wt.% (Ni-41Nb by at.%)) should form at 1178°C. To determine the wetting characteristics of the TLP, both sessile-drop and drop-transfer experiments using a 50:50 (by wt.%) NiNb liquid alloy were conducted on SSA-999W Al_2O_3 and c-plane sapphire substrates at 1400°C. There have been no previous efforts to measure the contact angle of a Ni-Nb liquid alloy on Al_2O_3 or any other ceramics.

Sessile-drop experiments with either a small piece of the 50:50 NiNb alloy that was sectioned from a solidified mixture or a cold-pressed foil assembly with the same composition, were conducted in a tungsten-element, high-vacuum ($\approx 10^{-6}$ torr) furnace at 1400°C. When the small pieces of the sectioned alloy melted, the liquid spread out to form "advancing" contact angles, and when the foils melted, the liquid retracted to form "receding" contact angles. By definition, advancing and receding contact angles are dynamic contact angles that are observed while the liquid surface is in motion, and this hysteresis is associated with the surface roughness of the substrate.[17] In the sessile-drop experiments, the alloy melted at ≈1200°C, and then the liquid either spread or retracted to form a spherical cap within a few seconds, well before the furnace temperature reached 1400°C. Once at temperature, the liquid remained stationary, but formed "advancing" or "receding" contact angles because the triple line was pinned by surface roughness features. Surface roughness on polished polycrystalline Al_2O_3 is often due to grain-boundary grooving at the solid-liquid interface and inherent porosities typical of sintered materials. Thus, the "advancing" and "receding" contact angles shown in Figure 4.16 should be distinguished from the dynamic advancing and receding angles. Rather, these angles should be considered as deviations from the equilibrium contact angle of the system due to pinning on the surface-roughness features. Given sufficient anneal time, these deviations from the equilibrium contact angle are expected to diminish, but as discussed in *Section 2.1.2*, changes in other variables, such as liquid compositions and substrate roughness, during the anneal may affect the contact angle.

The average "advancing" and "receding" angles on SSA-999W Al_2O_3 were 87° and 75°, and on sapphire were 90° and 83°, respectively (Figures 4.16a and b). An "advancing" contact angle was also measured on the SSA-999W Al_2O_3 with a graphite block placed in the furnace to simulate the P_{O2} level of the graphite-element hot press used to produce TLP joints. This experiment yielded an average contact angle of 90°. However, there was no available instrument to measure the P_{O2} levels in either the hot press or the wetting furnace. The contact angles were measured by observing the angles formed by tangent lines (as in Figure 2.1a). A circle-fit measurement method, which uses a program that fits a circle based on selected points along the liquid-droplet surface, was also explored. However, the circle-fit measurements, particularly for contact angles on the SSA-999W Al_2O_3, appeared to be less accurate than measuring the angles formed on either side of the droplets because the droplets were often asymmetric. Pinning of the liquid surface on surface roughness features (e.g., grain boundaries, surface flaws/voids) likely led to the droplet asymmetry. In contrast, the differences in the tangent-line and circle-fit contact-angle measurements on sapphire were minimal because the sapphire surface does not have grain boundaries and little or no surface asperities, and as a result, the droplets were nearly symmetric.

There were some experimental errors that caused a few discrepancies in the contact-angle measurements. For instance, there was a larger scatter in the "advancing" angles on the SSA-999W

Al_2O_3 ((ii) in Figure 4.16a) than in the other contact-angle measurements. Yet, qualitative assessment of the droplet images revealed minimal changes in the droplet shape. These variations in the contact angles over time were likely due to measurement errors, and not phenomenological occurrences. The most obvious source of any measurement errors is the viewing angle of the samples. Ideally, the contact angles are measured using photographs of perfectly perpendicular projections of the droplets. Although best efforts have been made to observe the droplets in this ideal position, in practice, the goniometer was either slightly above or below the perpendicular line of sight. It was found that when the viewing angle was above the perpendicular position, the images of the droplets contained reflections of the substrate surfaces, making the triple line nearly indistinguishable from the droplet surface ((ii) in Figure 4.16a). When the viewing angle was below the ideal position, the view of the triple line was obstructed by the front edge of the substrate, which can lead to a lower observed contact angle. It should also be noted that the droplets on the SSA-999W Al_2O_3 were asymmetric. The reported contact-angle measurements are averages of just two angles formed on each projected image, and lack any information about the contact angles formed along the rest of the triple line i.e., along the droplet perimeter.

Small differences in the "advancing" angles on SSA-999W Al_2O_3 with or without a graphite block in the furnace was observed (Figure 4.16a). As discussed in *Section 2.1.2*, P_{O2} levels can drastically affect the contact angles of liquid metals on ceramic substrates. Based on the chemical analysis of the joined samples, which showed there were no reaction layers at the metal-ceramic interfaces, the predominant form of interaction between the NiNb liquid alloy and the Al_2O_3 substrate is likely the dissolution reaction of the Al_2O_3 (rather than a redox reaction),

$$\tfrac{1}{2}\mathrm{Al_2O_3} \rightleftharpoons (\mathrm{Al}) + \tfrac{3}{2}(\mathrm{O}) \tag{4.1}$$

where the parentheses denote Al and O atoms dissolved in the liquid. The equilibrium constant of this reaction can be written in terms of the activities of (Al) and (O), a_{Al} and a_O, respectively, as

$$K_{eq} = a_{Al} \cdot a_O^{3/2} \tag{4.2a}$$

If the concentrations of (Al) and (O) are assumed to be in the dilute limit, Henry's law can be applied to assume constant activity coefficients, γ_{Al} and γ_O,

$$\begin{aligned} K_{eq} &= (\gamma_{Al} x_{Al})(\gamma_O x_O)^{3/2} \\ &= \gamma_{Al} \gamma_O^{3/2} x_{Al} x_O^{3/2} \end{aligned} \tag{4.2b}$$

where x_{Al} and x_O are mole fractions of Al and O in the liquid. The influence of the P_{O_2} of the atmosphere depends on the reaction

$$(\mathrm{O}) \rightleftharpoons \tfrac{1}{2}\mathrm{O_2} \tag{4.3}$$

If the O flux in and out of the droplet is at steady state, i.e., $\left(P_{O_2}\right)^{1/2} = a_O$, then reaction 4.1 is at equilibrium ($3x_{Al} = 2x_O$). When the P_{O_2} increases from this steady-state value, x_O increases (Sievert's law), driving reaction 4.1 to the left. The excess O atoms combine with the metal atoms, M, to form O-M clusters, which can become partially ionic, and adsorb onto the solid-liquid interfaces. If P_{O_2} is decreased, x_O decreases and reaction 4.1 proceeds to the right, dissolving excess Al atoms in the liquid. In M-Al_2O_3 systems, Al tends to adsorb onto the solid-liquid interface and decrease γ_{sl}.[29,137] Such shifts in reaction 4.1 have been attributed to the changes in the contact angles of Ni[14] and Fe[138] liquids on Al_2O_3 with P_{O_2}. In both systems, maximum contact angles were observed at x_O corresponding to the condition, $\left(P_{O_2}\right)^{1/2} = a_O$. Deviations from this equilibrium P_{O_2} result in the adsorption of Ni-O or Fe-O clusters, or Al atoms at the solid-liquid interface and, thus, lower contact angles.

Since the W-element wetting furnace and the graphite-element hot press were not equipped to measure the exact values of P_{O_2}, the effect of P_{O_2} on the wetting behavior has yet to be fully determined. At 1400°C, the equilibrium decomposition P_{O_2} for WO_2 is $\approx 9 \times 10^{-10}$ atm, which represents an upper bound P_{O_2} in the wetting furnace.[139] If CO is assumed to be the prevalent gas in the hot press, the same calculation for CO gives $P_{O_2} \approx 4 \times 10^{-24}$ atm, but with the given furnace hot-zone volume, this translates to 0.12 O_2 molecules – a nonsensical figure. Since the equilibrium P_{O_2} for the oxidation reaction of C is lower than that of W, placing the graphite block in the wetting furnace likely reduced the P_{O_2}. However, the 3° difference is within experimental errors due to differences in the substrate surface roughness, the initial alloy geometry, and the viewing angle of the droplet. Qualitative observation of a NiNb droplet on SSA-999W Al_2O_3 in the graphite-element hot press also revealed that the contact angle remained close to 90°. This suggests that within the range of P_{O_2} tested, the contact angle of NiNb liquid alloy is a weak function of P_{O_2}. To observe the effects of P_{O_2} on the contact angle of NiNb liquid on Al_2O_3, sessile-drop experiments in P_{O_2}-controlled inert-gas environments will be needed.

To further assess the interactions between the Al_2O_3 and the NiNb liquid alloy, SEM and EDS were used to observe and analyze the solidified droplets and the substrates. EDS analysis showed that there were Al_xO_y particles on the solidified surface of the NiNb droplet (Figure 4.17a and Table 4.1), but not within the droplet itself (Figure 4.17b). It has yet to be determined why these particles formed on the droplet surface. It may be possible that the NiNb alloy contained some Al_2O_3 particles since it was melted and solidified in an Al_2O_3 crucible. The wetting furnace itself may have also had some contamination since it has been used to conduct numerous wetting experiments on Al_2O_3 substrates. However, if contamination was not the source, it may be argued that these particles originated from the dissolved Al_2O_3 substrate. Figure 4.18 shows that the NiNb liquid etched the sapphire subtrate along the triple line, but the amount of Al_2O_3 dissolved in the alloy has not yet been measured. In order for the dissolved Al_2O_3 to form these Al_xO_y particles, the Al and O atoms in the liquid may have either segregated along the liquid-vapor interface to form Al-O clusters, or nucleated into Al_xO_y particles during cooling. Based on their non-uniform distribution along the droplet surface, however, neither scenario appears likely.

EDS analysis also revealed that the Al_xO_y particles also contained small amounts of W and small W particles were also found around the perimeter of the triple line on the sapphire surface, as shown in Figure 4.18. This micrograph shows that the particles are finer and more densely packed closer to the triple line. If there were W-contamination in the wetting furnace, one would expect the W particle size and distribution to be uniform. However, the non-uniform distribution suggests that the droplet may have been the source of W. The NiNb alloy may have contained some small amounts of W since it was made in a W-element, inert-gas furnace, but it is still unclear why the particle size increases farther away from the droplet surface. The fine particle sizes suggest that the particles nucleated at relatively low temperatures and did not have enough driving force to coarsen, which perhaps means that W particles did not form during the wetting experiment. A more in-depth analysis will be needed to determine the origins of both the Al_xO_y and W particles and whether the formations of these particles had any effects on the interfacial energies and the contact angles of the NiNb liquid on Al_2O_3.

4.3.2. Drop-Transfer Experiments

As mentioned earlier, the "advancing" and "receding" contact angles found in the sessile-drop experiments differ from the dynamic advancing and receding angles because they were measured by observing stationary droplets.[14] In order to find the true advancing and receding contact angles, spreading and retracting droplets must be observed. In low-temperature experiments (e.g., organic solutions), there are several ways to measure the true advancing and receding contact angles. For example, a syringe may be used to introduce the liquid onto the substrate to observe the advancing liquid, and to draw the liquid back in the syringe to examine the receding liquid. Another method would be to observe the contact angles formed on a tilted substrate, and to measure the advancing and receding contact angles on the leading and trailing sides of the droplet, respectively, as it rolls down the surface. With high-temperature systems, however, such experiments are difficult to execute. Thus, a drop-transfer experiment was conducted to measure the advancing angle of 50:50 NiNb liquid on SSA-999W Al_2O_3. As shown in Figure 3.4b, the drop-transfer setup consists of a liquid droplet on the bottom substrate (SSA-999W Al_2O_3) and the top substrate, which, in this case, was also an SSA-999W Al_2O_3 plate. When the top substrate was lowered and made contact with the droplet, a high-speed camera was used to capture the liquid spreading on the top substrate. The advancing angles, as shown in Figure 4.19, ranged from ≈110°–140° at 1250°C (the maximum operating temperature of the drop-transfer apparatus is 1250°C). A photograph of the advancing droplet is also shown in inset (ii) of Figure 4.19. Since both substrates were of the same composition, the liquid did not transfer onto the top substrate (as it would when the liquid preferentially wets the top substrate), but rather, remained in place and equilibrated. Following the advancing angle measurement, when the top substrate was raised with the droplet in place, a receding contact angle of ≈61° (inset (iii) in Figure 4.19) was obtained. Based on the sessile-drop experiment results and these advancing and receding contact angles, it is reasonable to believe that the equilibrium contact angle of this system is ≈90°.

A drop-transfer experiment was also conducted to measure the contact angle of the 50:50 NiNb liquid on solid Nb. As shown in Figure 3.4b, the NiNb alloy was melted on an SSA-999W Al_2O_3 substrate and the Nb substrate was lowered to make contact with the droplet at 1250°C. In the first experiment, within 0.5 s of the Nb substrate making contact with the droplet, the liquid spread to fill the gap between the two substrates and drew the Al_2O_3 plate up in contact with the Nb substrate (Figure 4.20a). Although this demonstrated how effective the liquid was in joining the two materials,

it prevented quantitative measurements of the contact angle on the Nb. When this experiment was repeated using a larger Al_2O_3 substrate and a smaller NiNb alloy bit, a contact angle ≈25° was observed (Figure 4.20b). This angle was measured shortly after the liquid ceased spreading, before significant interdiffusion occurred between the liquid and the Nb substrate.

With equilibrium contact angles of ≈90° and ≈25° on polycrystalline Al_2O_3 and Nb, respectively, the 50:50 NiNb liquid forms a contact angle sum well below 180°. Clearly, the dissolution of Nb in the liquid significantly lowered the contact angle on Al_2O_3, compared to a pure Ni liquid.[21,140] These relatively low contact angles allow strong, flaw-free interfaces to form during TLP bonding. It is expected that the equilibrium O concentration from the dissociation of Al_2O_3, x_O, in the NiNb liquid would be higher than in a pure Ni liquid[29] because Nb has a higher affinity for oxygen (i.e., formation free energies of NbO, NbO_2, and Nb_2O_5[141] are more negative than that of NiO[142]) and the NiNb liquid alloy forms a much lower contact angle on Al_2O_3. Unfortunately, x_O cannot be calculated using the Eustathopoulos' method[29] because of the lack of thermodynamic data for Al and O dissolved in a NiNb liquid alloy. Although good wetting behavior is not the only recipe to producing strong TLP bonds, the wetting properties must be considered when designing other multilayer-interlayer sytems for TLP bonding.

4.4 Bonding Kinetics

4.4.1 Bonding-Time Calculation

In TLP bonding of metals, it was recognized that the liquid must solidify isothermally and homogenize in order for the joint to survive high service temperatures and mechanical loads. Likewise, in ceramic-ceramic TLP bonding, favorable joint properties are obtained when a single-phase refractory interlayer is obtained through complete isothermal solidification and homogenization. As shown in Figures 4.3, 4.9, and 4.14, when the interlayer forms excess liquid that solidifies during cooling, formation of lower-melting-point intermetallic phase and degradation of fracture strengths were observed. In prior studies, phase diagrams, diffusion data, and prior experience have been considered in empirically determining the appropriate bonding conditions. While this method has led to several successful interlayer designs, the process remains time-consuming and tedious. A simple calculation-based model that uses published thermokinetic data to determine the isothermal-solidification and homogenization kinetics of a given system would greatly facilitate new interlayer designs and processing-condition optimization.

As discussed in *Section 2.3.2*, several studies explored both analytical and numerical models to determine the optimum processing conditions of metal-metal TLP bonds. In particular, these models have been used in predicting the isothermal-solidification time, which represents the minimum bonding time. The analytical models discussed in *Section 2.3.2* overestimated the solidification times by an order of magnitude.[79,99] These errors were attributed to the changes in the solid-liquid interfacial area due to grain-boundary grooving and possible unaccounted liquid loss from the joint regions in experimental samples. The numerical calculations appeared better suited to take the effects of base-metal microstructure into account, but were only used to observe local changes in the solidification rates near a grain boundary or the amount of solute diffused in a polycrystalline material, but did not explicitly calculate the solidification times.[108,111] In metal-metal TLP bonds, the dissolution process can increase the liquid-film thickness by up to tens of microns from the initial interlayer thickness.[79,86,87,90,99] When in contact with such a thick liquid layer, the grain boundaries intersecting the solid-liquid interfaces groove by as much as tens of microns, causing non-planar solidification and local variations in the MPD flux.[99] In these studies, there was also no attempt in predicting the actual

amount of MPD retained in the system. The effects of diffusion during heating in TLP bonding has been qualitatively described,[98,103] but none of the models have quantified MPD diffusion during heating and cooling. Clearly, there are no reliable methods available to predict the optimum bonding conditions for TLP bonding.

Just as in metallic systems, it is difficult to predict the bonding conditions in TLP bonding of ceramics and there are no models available to predict the isothermal-solidification and homogenization times. However, there are some key characteristics in TLP bonding of ceramics that may allow for some simplifying assumptions in calculating the processing times. Multilayer-interlayer systems typically consist of ≈2-μm thick cladding layers deposited on 50–125-μm thick core layers. Depending on the liquidus composition, the maximum possible liquid-film thickness is typically <5 μm on either side of the core layer. In actual systems, the liquid films are expected to be thinner than the maximum thickness because some interdiffusion between the cladding and core-layer materials during heating is expected and if excess liquid forms in relation to the interfacial gap width, the liquid is also expected to flow out of the joint and further reduce the liquid-film thickness. This reduces the solid-liquid interface displacement to at most a few microns, and thus, it may be assumed that the interface remained fixed in position. The solid-liquid interface was also assumed to be planar because grain-boundary grooving and liquid penetration along grain boundaries appeared limited when relatively thin TLP layers were retained (with a 2.4-MPa bonding pressure), as observed in Figure 4.5a–c. Since diffusion of most metals in ceramics is sluggish, it can be assumed that diffusion takes place only within the interlayer.

In this work, the MPD (Ni) concentration profiles were determined using published solubility and diffusivity data, and two different solutions to Fick's second law. Eqn. 3.1 was used to obtain the Ni-concentration profiles during isothermal solidification and Eqn. 3.3 was used to calculate the concentration profiles during the homogenization process, as illustrated in Figure 4.21. The first step is to calculate the effective diffusion time to account for the Ni diffusion during heating and cooling. This was done by using the temperature-dependent expressions for the lattice and grain boundary diffusivities[133,134] and using Eqn. 3.2 to obtain $D_{app}(T)$ to calculate the diffusion distance, $\sqrt{D_{app}(T)t}$, over the entire bonding cycle. The total diffusion distance was then used to calculate the time needed to obtain the equivalent diffusion distance at 1400°C. With the 4°C/min and 2°C/min heating and cooling rates, respectively, the effective diffusion time in single-crystal Nb was 60 min. Thus, for instance, when calculating the Ni-concentration profile for a 5-min bond, a diffusion time of 65 min was used. The effective diffusion time increases as the average Nb grain size decreases because of the higher grain-boundary diffusion contribution at lower temperatures.

In the isothermal-solidification step, the liquid is in contact with the solid surface, and thus, it can be assumed that the Nb-core-layer surface concentrations are fixed at the solidus composition (4.5 at.% Ni). With this assumption, isothermal solidification is complete once the total amount of Ni diffused coincides with the amount of Ni in the liquid films. Since the EPMA results showed that substantial amount of Ni was lost due to liquid flowing out of the joints, the average measured Ni concentration, ≈0.8 wt.% Ni, was used in the initial condition, rather than the 4.5 wt.% Ni corresponding to the two 2-μm thick Ni cladding layers. Once the solidification is complete, it is followed by the homogenization stage, which takes the Ni-concentration profile from the first solution as the initial condition and assumes that diffusion occurs between two impermeable boundaries over the remaining isothermal-holding time (i.e., (total effective diffusion time) – (isothermal-solidification time)). Since the Nb microstructure changes during bonding, various average Nb grain sizes were used

to calculate D_{app}, which were then used in Eqns. 3.1 and 3.2. The resulting Ni-concentration profiles were quantitatively compared to the measured profiles to assess the validity of this model, as shown in Figure 4.22. The objectives of this model are to study the effects of processing conditions on the bonding times and to provide a method of calculating the MPD-diffusion profiles to obtain a set of optimum processing conditions.

The calculated Ni-concentration profiles and the EPMA results in Figure 4.22a and b show that in the 5-min and 30-min samples, respectively, the best fit was obtained when 200-μm Nb-grain size was assumed. With the 6-h samples, the calculated values were very similar to those of the measured profile irrespective of the grain size used. As shown in Figures 4.5 and 4.8, the actual Nb-grain size increased from 10 μm to 130, 180, and 520 μm in the 5-min, 30-min and 6-h samples, respectively. Since diffusion and grain growth occur simultaneously during the entire bonding cycle, the average grain size predicted by the model is expected to be smaller than the final grain sizes of the joined interlayers. However, the calculations presented in Figure 4.22 show that when the Nb-grain size is <200 μm the apparent diffusivity is too high compared to the actual system. Part of this discrepancy may be due to the crude approximation of D_{app} and the use of Fick's law, which assume that the grain boundaries are stationary and that the lattice diffusion distance is much greater than the grain size, i.e., $\sqrt{D_l t} \gg d$ (Type A kinetics according to Harrison[112]) The diffusion distance after a 65-min isothermal holding time at 1400°C is ≈13 μm, which is comparable to the *initial* Nb-grain size and significantly less than the final grain size. The significance of Nb microstructure will be discussed in more detail in the following section.

One possible source of error in this model is the lack of ability to predict the amount of liquid retained in the system, which depends on the wetting behavior, bonding pressure, and the joining surface roughness. As mentioned earlier, the EPMA results showed that most of the Ni was lost due to excess liquid flowing out of the joint. With the calculations presented in Figure 4.22, the amount of Ni used in the boundary condition was based on the overall Ni concentrations measured in the joined samples. Unfortunately, there is no systematic approach to relate the amount of liquid retained in the joints with wetting property, bonding pressure, and surface roughness. For instance, while most studies quantify surface roughness with a single R_a (mean deviation in surface height) value, there are no means of distinguishing long-range waviness and short-range roughness, as well as the shapes of the surface features – all of which are important in determining the interfacial void volume filled by the liquid. Similar surface roughness characterization issues were presented, but left unresolved in previous studies of roughness effects on wetting.[16-18,20] With the current model, it is possible to observe the effects of the total amount of Ni retained in the joint on the isothermal-solidification time, as shown in Figure 4.23. Here, the amount of Ni diffused is converted to initial cladding layer thickness and all of the Ni from the cladding layer is assumed to remain in the joint. It would be expected that when the amount of Ni approaches its solubility limit in Nb, the driving force for diffusion (i.e., the concentration gradient) becomes smaller, which would lead to longer isothermal-solidification times. Indeed, Figure 4.23 shows that for a given value of Nb grain size (or D_{app}), the isothermal-solidification time increases with increasing slope as the total amount of Ni increases. When very thin cladding layers are used, or, equivalently, when a small percentage of the initial cladding layer remains in the system, small differences in the predicted amount of Ni diffused results in relatively small errors in the isothermal-solidification times. However, if larger amounts of Ni remain in the joint, significantly larger errors in the solidification times are observed. This plot also shows that when a relatively small amount of Ni is in the system (<0.5 μm thick), the isothermal-solidification times

predicted for single-crystal and 200-μm grain polycrystalline Nb are within 1 h of each other. Thus, even without specific knowledge of core layer microstructure, this model can at least provide an order of magnitude estimation of the isothermal-solidification time when the amount of MPD is minimized.

Another issue that may affect the accuracy of this model is the Ni diffusion calculation in the heating stage. This model simply compares the diffusion distances during heating based on a constant D_{app} and solidus (surface) composition. However, the Ni-Nb phase diagram shows that a liquid does not form until the system reaches 1178°C and the liquid is in equilibrium with the Ni_6Nb_7 phase up to 1291°C, rather than Nb (Figure 2.5). Below the bonding temperature, Ni_3Nb and Ni_8Nb intermetallic phases are also stable at higher Ni concentrations. The diffusion distance in the heating stage was found to be equivalent to that of ≈30-min hold at 1400°C in Nb with a 200-μm average grain size. However, the isothermal-solidification time predicted by the model was ≈11 min when a total concentration of 0.8 at.% Ni was used. In the actual system, some Ni diffusion is expected to occur during heating, prior to liquid formation. Once the system reaches the eutectic temperature, the liquid forms, and the excess liquid flows out of the joint rapidly, while the remaining liquid isothermally solidifies. While the results suggest that intermetallic formation and time-dependent changes in the solubility limits in the Ni-Nb system may not have had a significant impact on the calculated Ni-concentration profiles, these issues may play bigger roles when transferring this model to other materials combinations. Clearly, a more sophisticated calculation method would be needed to account for the changes in solubility, diffusion rates, core-layer microstructure, and liquid loss. With the current model, comparisons between Ni concentration profiles of samples joined using higher heating rates and the calculated profiles may deconvolute some of these complications.

It should be emphasized here that with the Ni/Nb/Ni interlayer, the processing conditions were already known, and therefore, the unknown parameter in the calculation was the average grain size, or the corresponding D_{app}. While the predicted grain size (200 μm) is larger than expected, it is still relatively close to the final grain sizes observed in the joined interlayers. While there are some limitations, since this model was able to match the Ni concentration profiles in the current system, it should be able to estimate the processing times for other interlayer systems.

4.4.2 Effects of Core-Layer Microstructure

In the Ni/Nb/Ni interlayer, when the amount of liquid retained in the joint was reduced by using a 2.4-MPa bonding pressure, bonding times as short as 5 min were sufficient to produce strong, isothermally-solidified joints. When the bonding pressure was decreased, which increased the amount of liquid in the system, even a 6-h bonding time was insufficient for complete isothermal solidification to occur. While Ni has been identified as an anomalously fast diffuser in Nb, this interlayer system would still benefit from enhanced diffusion rates, which would decrease the solidification times, particularly when low bonding pressures are used. One method of increasing the diffusion rate is to simply use a higher bonding temperature, but this can result in lower post-bond Al_2O_3 fracture strength due to microstructural degradation (i.e., grain growth). An alternative route would be to increase the contribution of grain-boundary diffusion in the core layer, thereby increasing D_{app}. In metal-metal TLP bonding, the isothermal-solidification time can be significantly shorter when joining base-metal parts with smaller grains.[104,105] As shown in Figures 4.22 and 4.23, bonding-time calculations can be highly sensitive to D_{app}, i.e., the average Nb grain size. In order to extend the model presented in this study to other materials systems, a more sophisticated method of predicting D_{app} is needed.

To examine the effects of core-layer microstructure on the bonding kinetics, as-rolled, and recrystallized (rolled and then annealed at 1000°C for 1 h) Nb foils, shown in Figures 4.24a and b, respectively, were used as the core layers. Compared to the microstructure of the as-received 125-μm thick Nb foil (Figure 4.5d), the as-rolled and recrystallized Nb foils had smaller, highly deformed grains. Both the as-rolled and recrystallized Nb layers were coated with 2-μm thick Ni films and used to join SSA-999W Al_2O_3 plates at 1400°C for either 5 min or 30 min with a 2.4-MPa bonding pressure. Due to equipment problems, mechanical test samples could not be fabricated. Instead, the joined plates were cross-sectioned for microstructural and chemical analyses.

The interlayer microstructures of the as-rolled and recrystallized Nb core layers, as shown in Figures 4.24c–f, appear quite similar to each other and to those of the as-received Nb core layers (Figures 4.5a–c). Even with a 5-min isothermal holding time, the majority of the grains spanned approximately half the interlayer thickness. The grains in the 30-min samples appear to be only marginally larger than those in the 5-min bonds and the interlayer microstructures also appear similar to those of the joints made with the commercially available Nb foil (Figures 4.5a and b). Ideally, the finer grain structures of the as-rolled and recrystallized Nb layers would be maintained throughout the joining process to enhance the grain-boundary contribution to Ni diffusion. However, it appears that under the processing conditions used in this study, the initial Nb microstructure has no discernible effect on the final interlayer microstructure. To observe the interlayer microstructure evolution, the as-rolled, recrystallized, and as-received foils were used to join Al_2O_3 at ≈1000°C. In all cases, the near-interface Nb grains grew substantially compared to those in the center of the interlayer, as shown in Figure 4.25. EPMA revealed that the Ni only diffused through the large-grained regions while no measurable amount of Ni was present in the finer-grained regions. Ideally, when a finer-grained Nb core layer is joined, Ni diffusion would be enhanced by a larger contribution from grain-boundary diffusion. However, the micrographs of the joined interlayers show that the Nb microstructure above 1000°C is essentially independent of its initial microstructure because Ni diffusion accelerates grain growth.

EPMA was conducted to measure the Ni concentrations in the interlayers based on the as-rolled and recrystallized Nb core layers. Figure 4.26a shows the Ni-concentration profiles of the samples bonded for 5 min and Figure 4.26b shows those bonded for 30 min at 1400°C. The Ni-concentrations in the as-rolled and recrystallized Nb are nearly identical and the differences between the 5-min and 30-min bonds appear to be minimal. When compared to the samples joined with the as-received Nb core layer (Figure 4.6), the as-rolled and recrystallized Nb interlayers have higher centerline concentrations and lower peak concentrations along the interfaces. This suggests that the finer grain structure in the initial Nb core layer enhanced the apparent Ni diffusion rate, despite having similar final microstructures as those of the joined as-received Nb. However, since most of the liquid flows out of the joints when a 2.4-MPa bonding pressure is used, the decrease in isothermal-solidification time may only be on the order of minutes (Figure 4.23). On the other hand, if lower bonding pressures are desired, which may result in wider interfacial gaps to be filled by thicker TLP layers, then using a finer-grained Nb core layer may result in a more substantial isothermal-solidification-time decrease.

The results of the processing-time model also showed that obtaining the true apparent diffusivity, which is microstructure dependent, is a key hurdle in accurately predicting the isothermal-solidification times. As discussed in *Section 2.3.2*, in metal-metal TLP bonding, it was recognized that grain-boundary diffusion can decrease the isothermal-solidification times,[79,99,103,114] but these studies

had limited success predicting the effects of grain-boundary diffusion on the process kinetics.[108,111] In analytical treatments, solutions to Fick's second law have been used to calculate the MPD-concentration profiles. As described by Harrison, when grain-boundary diffusion dominates (Type B and C kinetics), as is the case for diffusion depth $>(3 \text{ to } 4)\times\sqrt{D_l t}$ from the interface, then Fick's law does not apply. It has been shown empirically that when *ln C* (solute concentration) is plotted against $y^{6/5}$ (distance from the surface), the concentration profile corresponding to diffusion along stationary grain boundaries becomes approximately linear, as illustrated by the "penetration tail" in Figure 4.27a. When grain-boundary migration occurs, the near-surface concentrations increase and the *ln C* vs. $y^{6/5}$ plot shows another linear region (with a steeper slope) at intermediate depths where diffusion along moving grain boundaries is prevalent (Figure 4.27b).[106]

To analyze the effects of the initial Nb microstructure on Ni diffusion, *ln C* vs. $y^{6/5}$ plots of EPMA data were generated for the interlayers containing the as-received (Figures 4.28a and b), recrystallized (Figures 4.28c and d), and as-rolled (Figures 4.28e and f) Nb core layers. Each plot contains two sets of data representing the Ni concentrations in each half of the interlayer. In the as-received Nb, each of the data set appears to fit a single line, indicating that lattice diffusion dominated throughout. This is expected since the interlayers were ≈120 μm thick and therefore, the half-thickness is close to $(3 \text{ to } 4)\times\sqrt{D_l t}$ ($\sqrt{D_l t} \approx 13$ μm for 5-min and $\sqrt{D_l t} \approx 15$ μm for 30-min bonds). If the interlayer had been thicker, the concentration profile may have contained sharp changes in the slope near the center of the interlayer where grain-boundary diffusion would prevail. In contrast, the Ni concentration profiles in the recrystallized and as-rolled Nb appear to have two distinct slopes. Within $(3 \text{ to } 4)\times\sqrt{D_l t}$ from the interface, the concentration profile has a steeper slope, indicating that lattice diffusion dominated. Since the Nb grain size increased by an order of magnitude, it is likely that there was negligible contribution from Ni diffusion along stationary grain boundaries. Therefore, in the regions far from the interlayer, $>(3 \text{ to } 4)\times\sqrt{D_l t}$, where the concentration gradient is much smaller, diffusion along migrating grain boundaries likely dominated (similar to the schematic in Figure 4.27b without the stationary-grain-boundary diffusion "tail"). It should be emphasized here that these transitions in the concentration gradients are only visible in the as-rolled and recrystallized Nb layers largely because the interlayers were ≈156 μm thick, and thus, the half-thickness of the interlayer exceeded $(3 \text{ to } 4)\times\sqrt{D_l t}$.

There appears to be significant scatter in the grain-boundary-diffusion-dominated regions in both the recrystallized and as-rolled Nb layers. This is somewhat expected because the Ni sources were on both sides of the Nb core layer, significant overlaps in the Ni concentrations are expected in the middle of the interlayers. Some measurement errors are also expected because the EPMA scans can only sample a 3-μm-wide area per each data point, which is significantly smaller than the average grain size. In typical diffusion coefficient measurements, serial sectioning technique is used to measure the tracer activity over a much larger area at a particular depth. Thus, to obtain the apparent diffusivity as a function of Nb microstructure, an experiment with a single Ni source diffusing into a much thicker Nb sink should be conducted.

Based on these observations, the current processing-time calculations may be improved by adding another solution for grain-boundary diffusion, such as Whipple's solution.[106,143] In the current model, the total processing time is partitioned into isothermal-solidification and homogenization times, which are solved in sequence. Following this recipe, a solution for grain-boundary diffusion can

perhaps precede the isothermal-solidification solution in the "initial" stages of joining. However, grain-boundary diffusion must still be active for diffusion distances $>(3 \text{ to } 4)\times\sqrt{D_l t}$ until the half-thickness of the interlayer becomes $\approx(3 \text{ to } 4)\times\sqrt{D_l t}$. In other words, a moving boundary that is $\left(3 \text{ to} 4\right)\times\sqrt{D_l t}$ from the interface must be included to distinguish grain-boundary- and lattice-diffusion-dominated regimes. A numerical method that can simultaneously solve the expressions for both grain-boundary and lattice diffusion may be a more accurate way of predicting isothermal-solidification times. However, in the limiting case where the half-thickness of the interlayer is $\approx(3 \text{ to } 4)\times\sqrt{D_l t}$ within a relatively short processing time (i.e., a relatively thin core layer), the current model can provide a much simpler and reasonably accurate means of calculating the processing times.

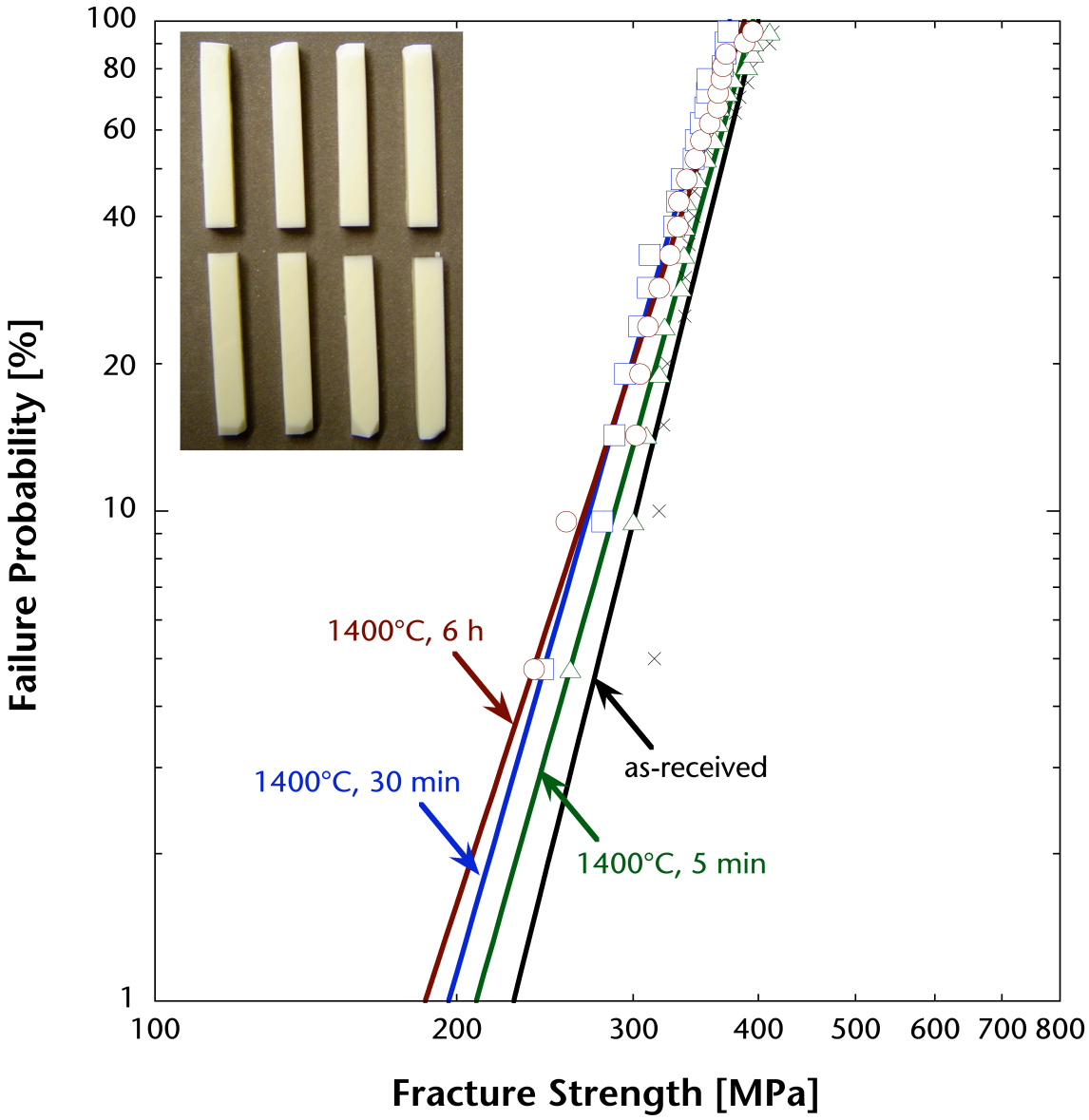

FIGURE 4.1A Fracture probability vs. fracture strength relationships for as-received and annealed SSA-999W Al_2O_3. The insert shows four-point-bend-test samples that have been fractured.

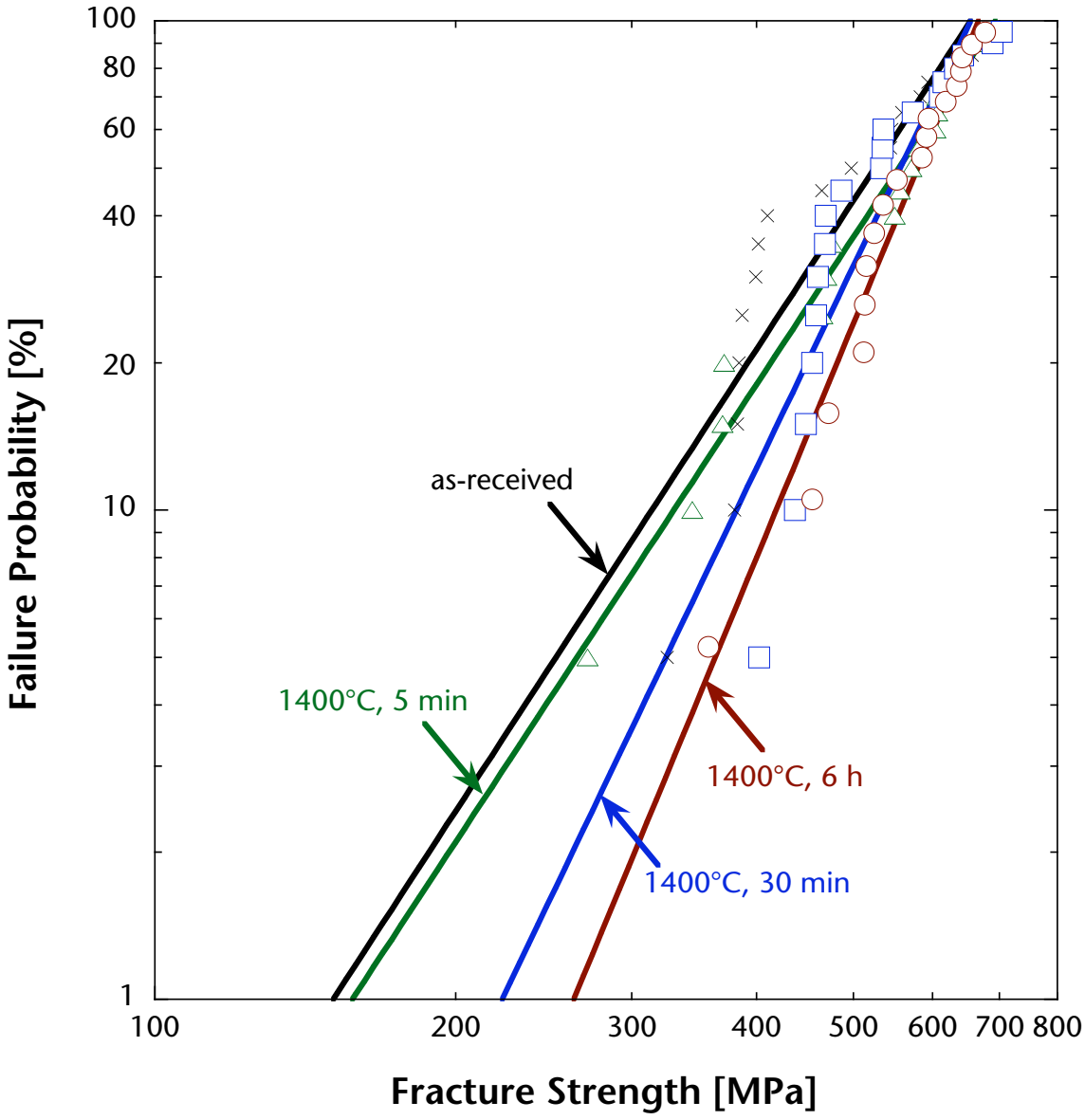

FIGURE 4.1B Fracture probability vs. fracture strength relationships for as-received and annealed SSA-999S Al_2O_3.

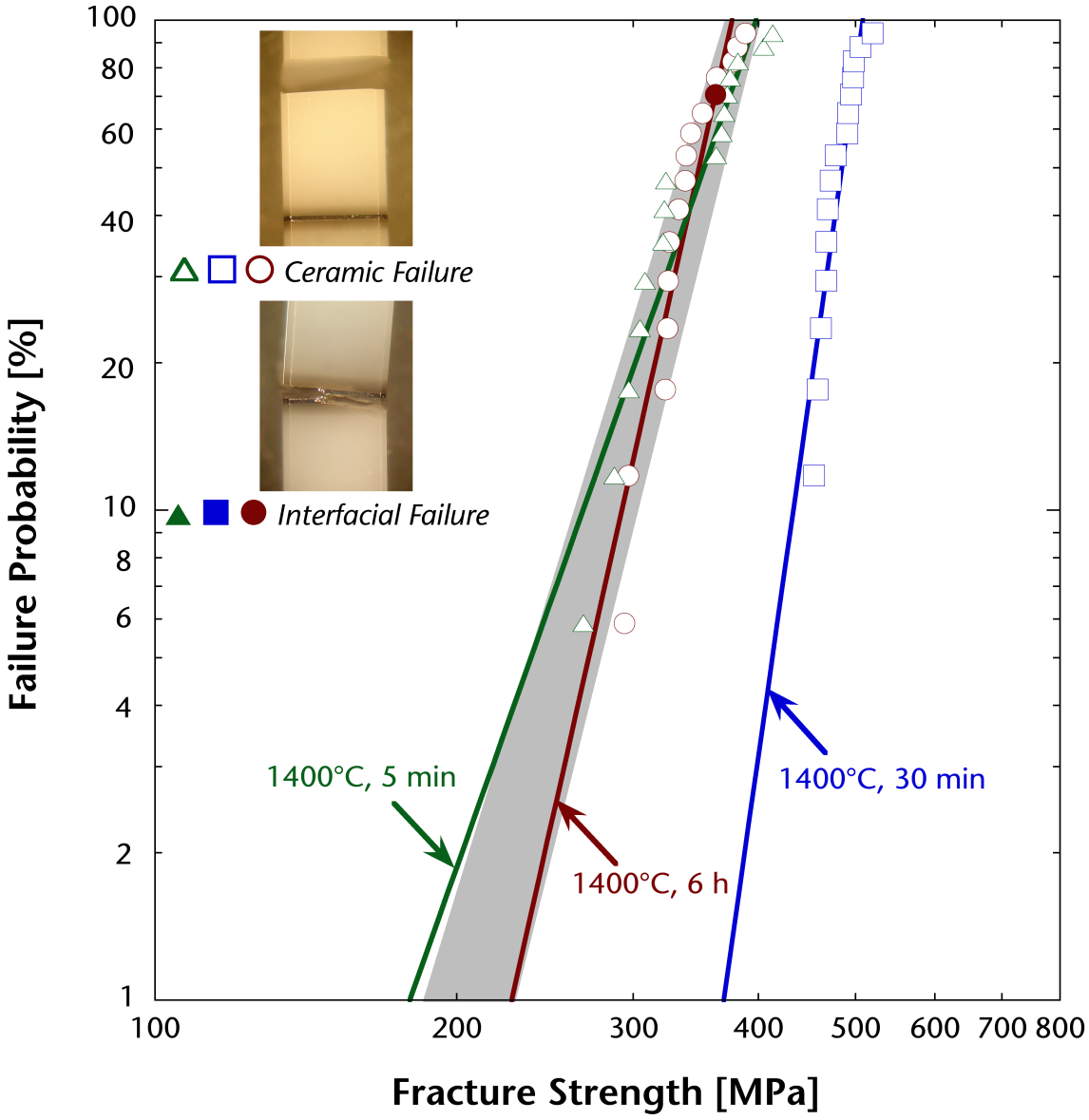

FIGURE 4.2A Fracture probability vs. fracture strength relationships for Al_2O_3/Ni/Nb/Ni/Al_2O_3 joints bonded at 1400°C with 2.4 MPa bonding pressure. The joints were produced using SSA-999W Al_2O_3. The open data points indicate beams that failed in the ceramic, while the filled points represent those that failed in the interface. The gray section represents the compiled fracture strengths of the as-received and annealed bulk SSA-999W Al_2O_3.

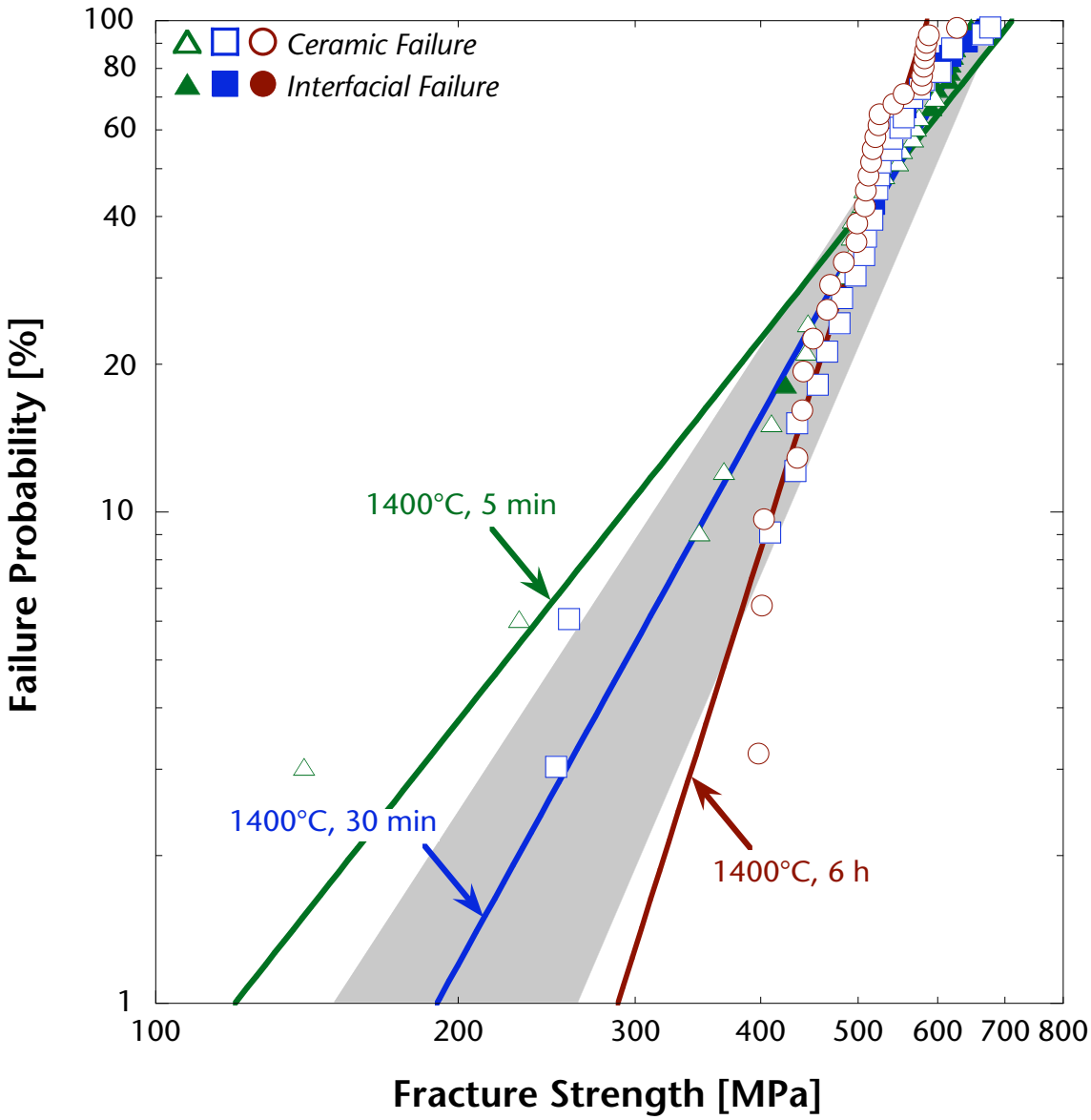

FIGURE 4.2B Fracture probability vs. fracture strength relationships for Al_2O_3/Ni/Nb/Ni/Al_2O_3 joints produced using SSA-999S Al_2O_3. The gray section represents the compiled fracture strengths of the as-received and annealed bulk SSA-999S Al_2O_3.

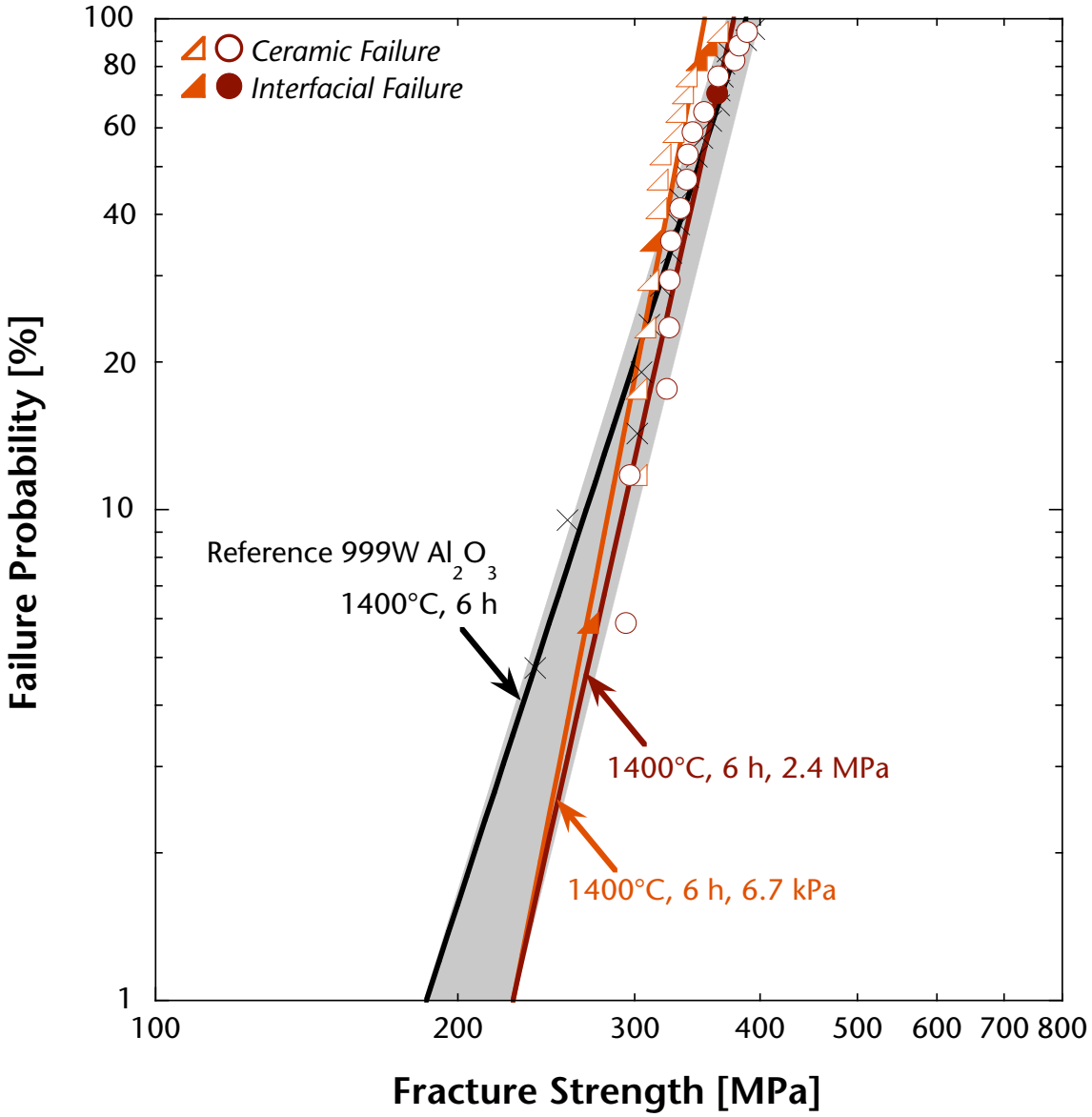

FIGURE 4.3A Fracture probability vs. fracture strength relationships for Al_2O_3/Ni/Nb/Ni/Al_2O_3 joints bonded at 1400°C for 6 h using 6.7 kPa pressure. The SSA-999W Al_2O_3 was used for this data set. Fracture strengths of the samples bonded using a 2.4 MPa bonding pressure, as well as those of the monolithic SSA-999W Al_2O_3 annealed 1400°C for 6 h, are also plotted for comparison.

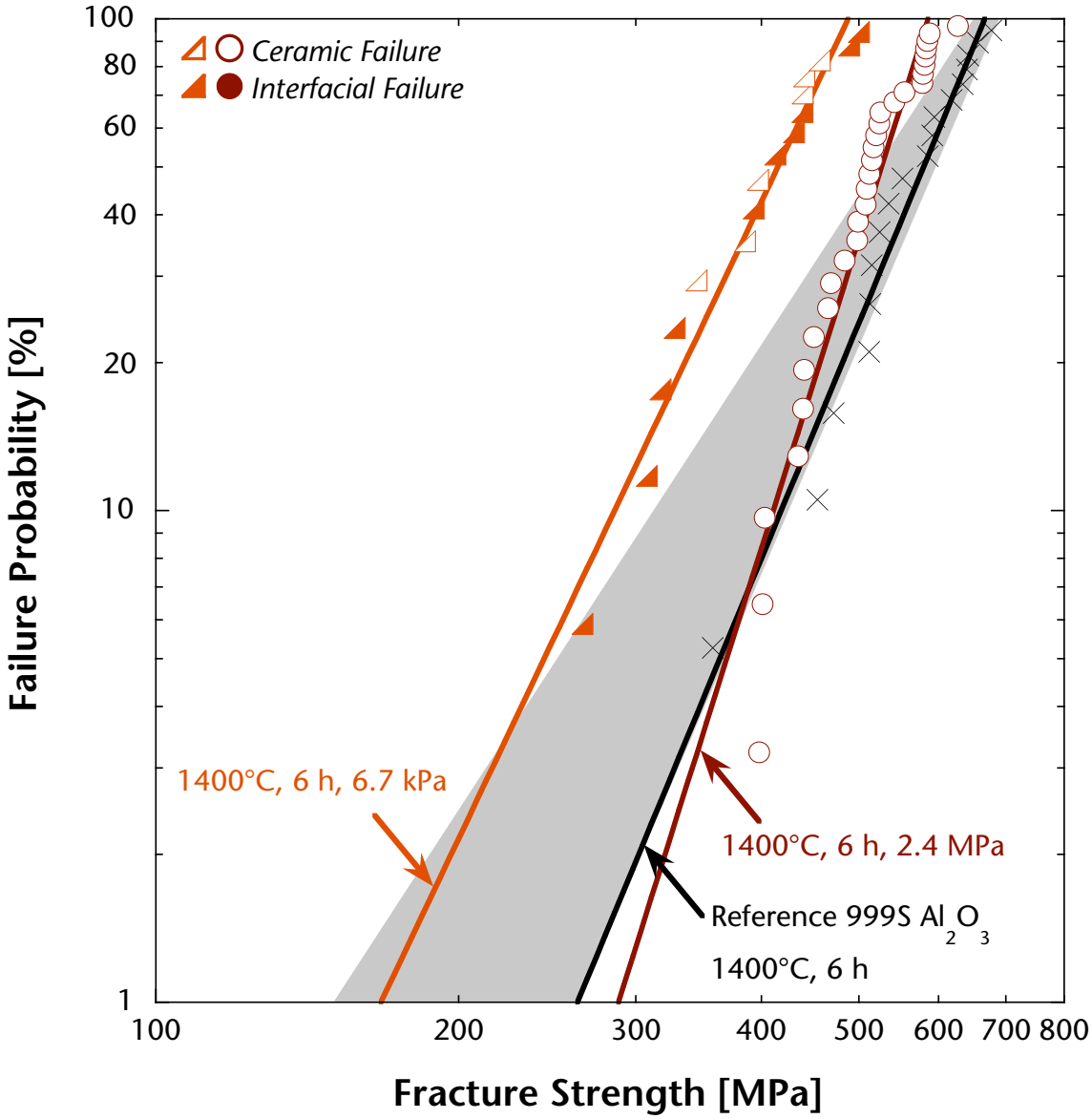

FIGURE 4.3B Fracture probability vs. fracture strength relationships for Al_2O_3/Ni/Nb/Ni/Al_2O_3 joints bonded at 1400°C for 6 h using 6.7 kPa pressure. The SSA-999S Al_2O_3 was used for this data set. Fracture strengths of the samples bonded using a 2.4 MPa bonding pressure, as well as those of the monolithic SSA-999S Al_2O_3 annealed 1400°C for 6 h, are also plotted for comparison.

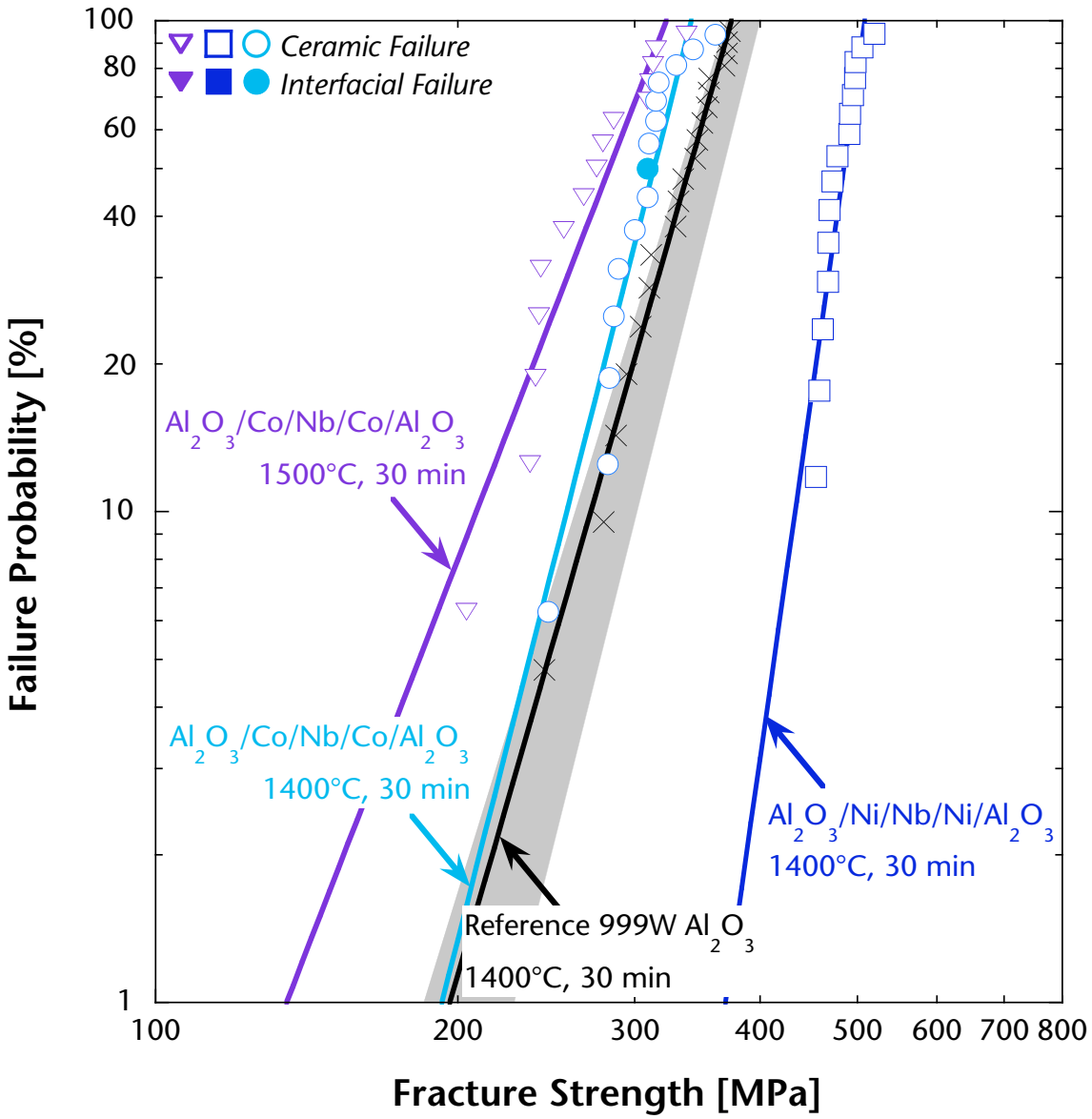

FIGURE 4.4 Fracture probability vs. fracture strength relationships for Al_2O_3/Co/Nb/Co/Al_2O_3 joints bonded at 1400°C for 30 min using 2.4 MPa pressure. The SSA-999W Al_2O_3 was used for this data set. Fracture strengths of the Al_2O_3/Ni/Nb/Ni/Al_2O_3 bonded for 30 min, as well as those of the monolithic SSA-999W Al_2O_3 annealed 1400°C for 30 min, are also plotted for comparison.

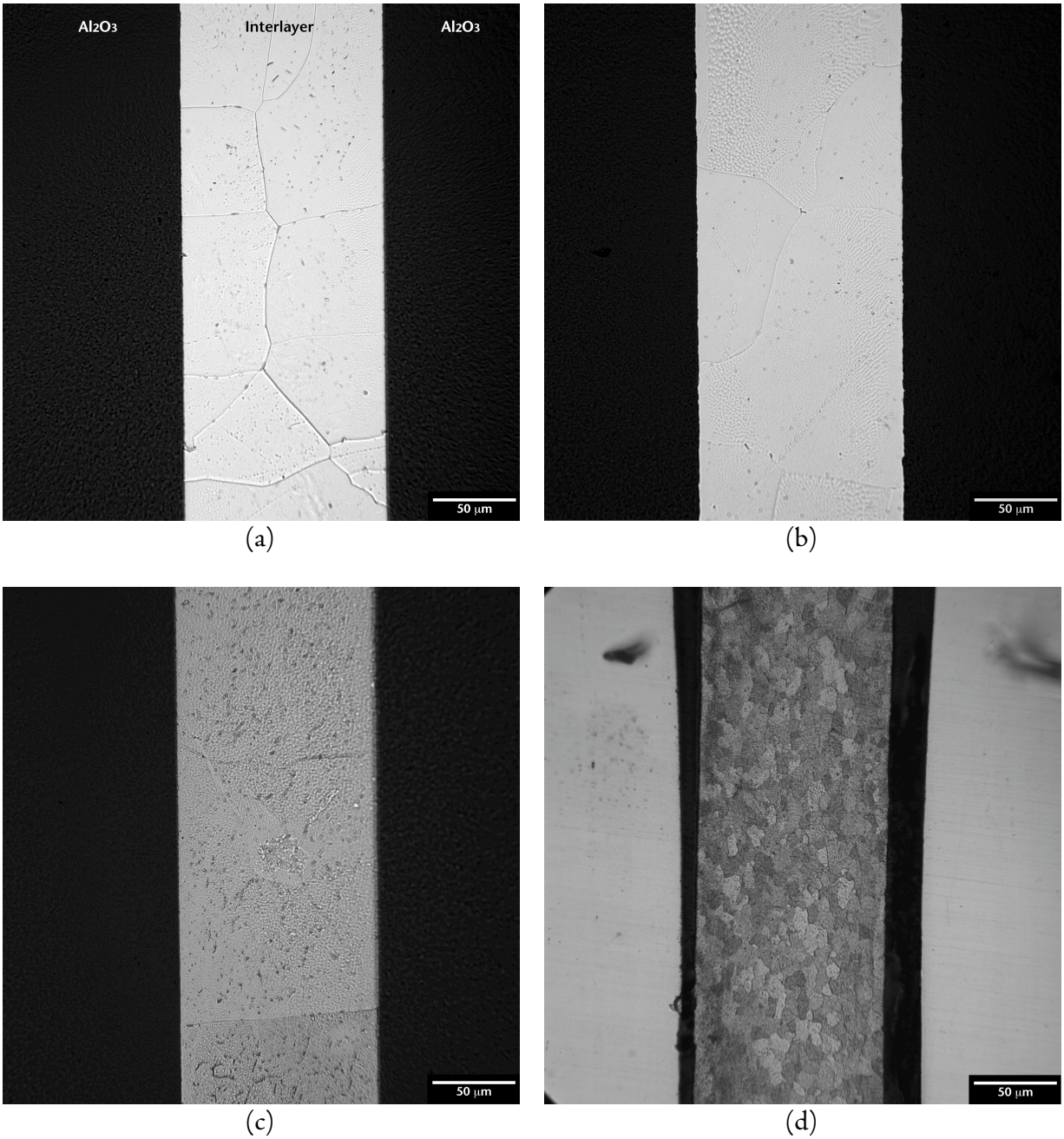

FIGURE 4.5 Optical micrographs of Ni/Nb/Ni interlayers bonded at 1400°C for (a) 5 min, (b) 30 min, and (c) 6 h, using 2.4 MPa bonding pressure. (d) Optical micrograph of as-received Nb. The samples were etched to reveal the grain boundaries.

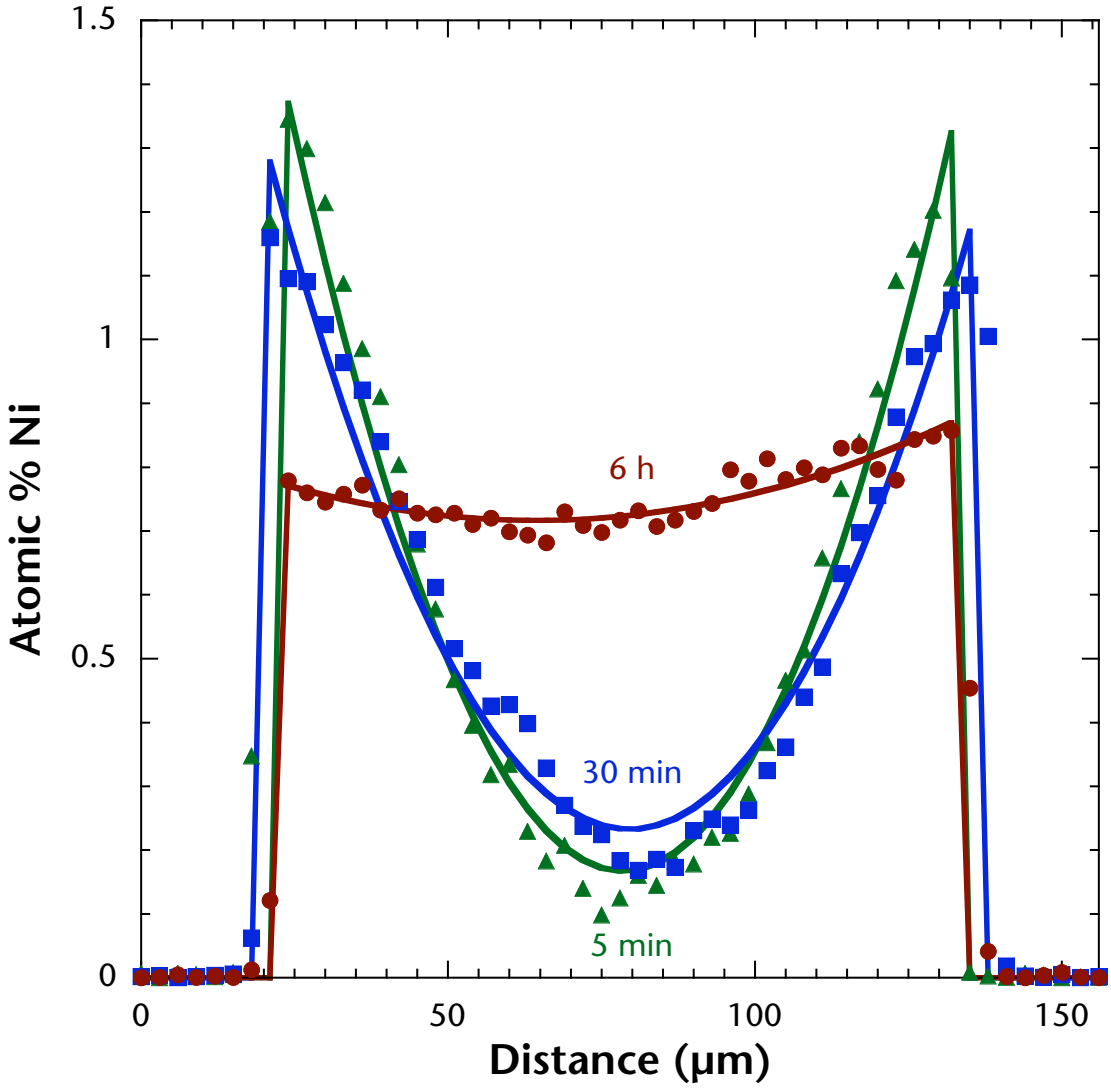

FIGURE 4.6 Ni concentrations in Ni/Nb/Ni interlayers bonded at 1400°C with 2.4 MPa pressure obtained through an EPMA. Each sample was subjected to two separate line scans across the interlayer, and the data points shown are the averages of each pair of scans.

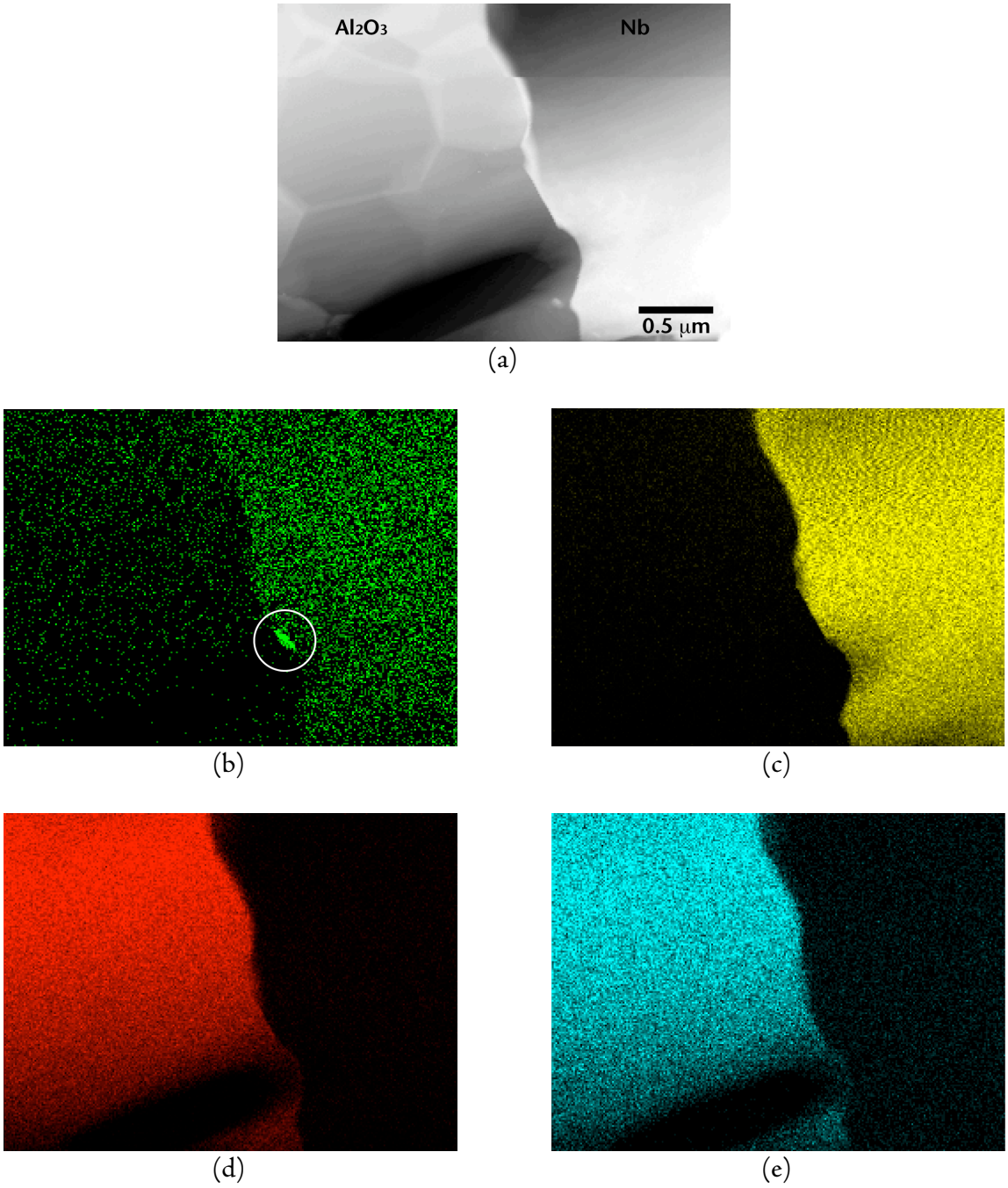

FIGURE 4.7 (a) Transmission electron micrograph of the metal-ceramic interface in a 1400°C, 30 min bond. Qualitative concentration maps of (b) Ni, (c) Nb, (d) Al, and (e) O from an EDS are also shown. The circled region in (b) indicates a possible Ni-rich phase.

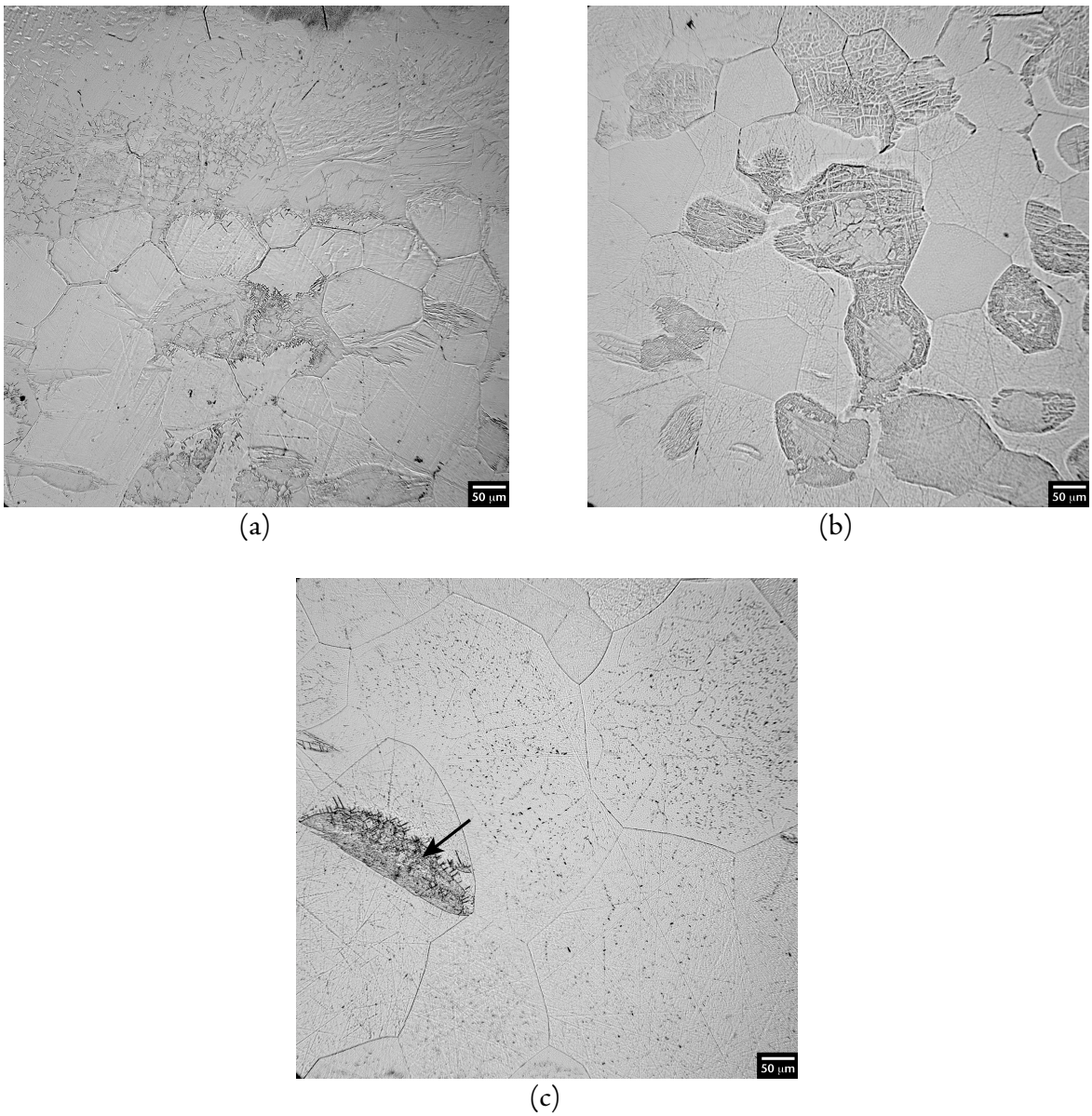

(a) (b)

(c)

FIGURE 4.8 Plan view optical micrographs of Ni/Nb/Ni interlayers that have been bonded at 1400°C for (a) 5 min, (b) 30 min, and (c) 6 h (See schematic in Figure 3.3). These micrographs show that the actual grain sizes of the Nb after bonding grew to be larger than the thickness of the foil (125 μm), particularly after a 6 h isothermal holding time. The faceted regions, such as the one highlighted by the arrow in (c), appear to be dislocations formed to compensate for any lattice misfit.

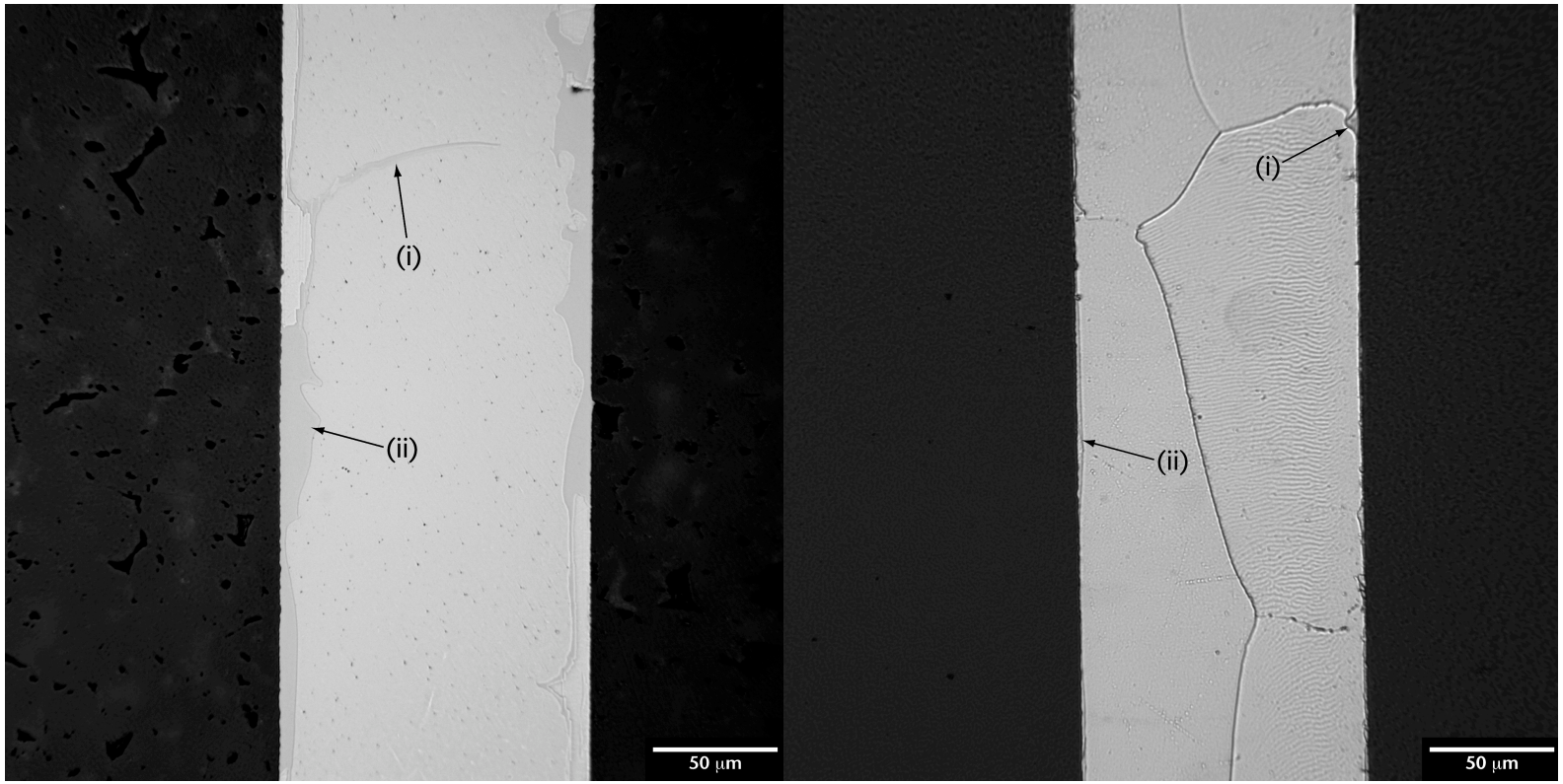

FIGURE 4.9 Optical micrographs of Ni/Nb/Ni interlayers of samples bonded at 1400°C for 6 h using a 6.7 kPa bonding pressure. (a) Shows a region near the sample edge and (b) near the center of the sample. Both images show liquid penetration along grain boundaries (i) and formation of intermetallic layers along the interfaces (ii). In (a), excess liquid was present due to wider interfacial gaps compared to (b).

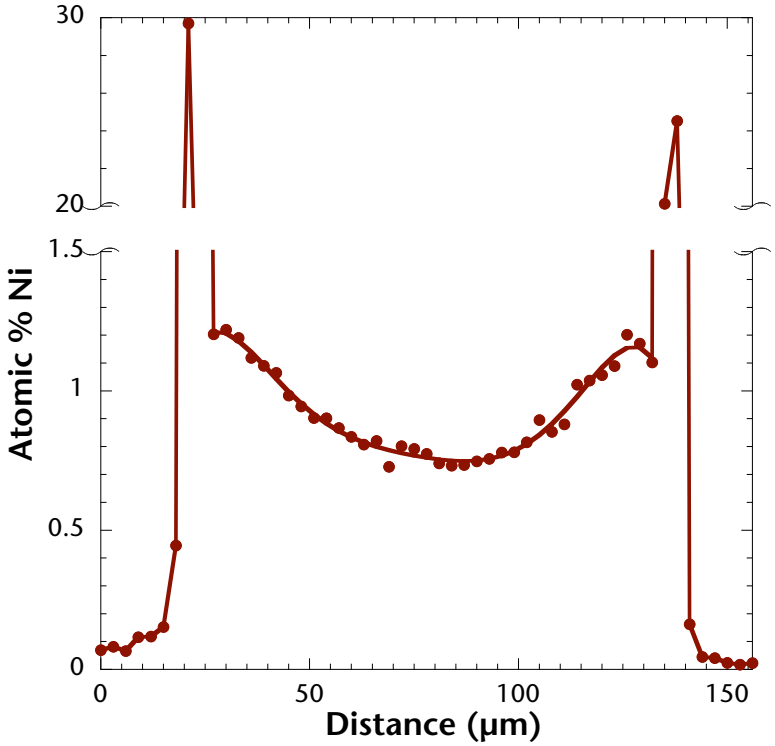

(a)

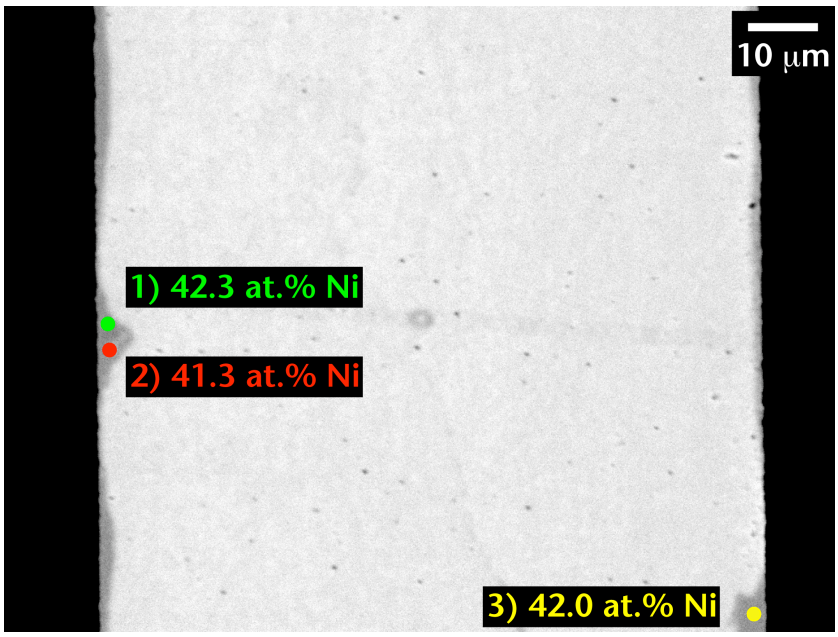

(b)

FIGURE 4.10 (a) Ni concentration profile of Ni/Nb/Ni interlayer processed at 1400°C for 6 h with a 6.7 kPa bonding pressure. (b) Backscatter electron micrograph of the Ni/Nb/Ni interlayer with Ni concentrations measured using spot scan.

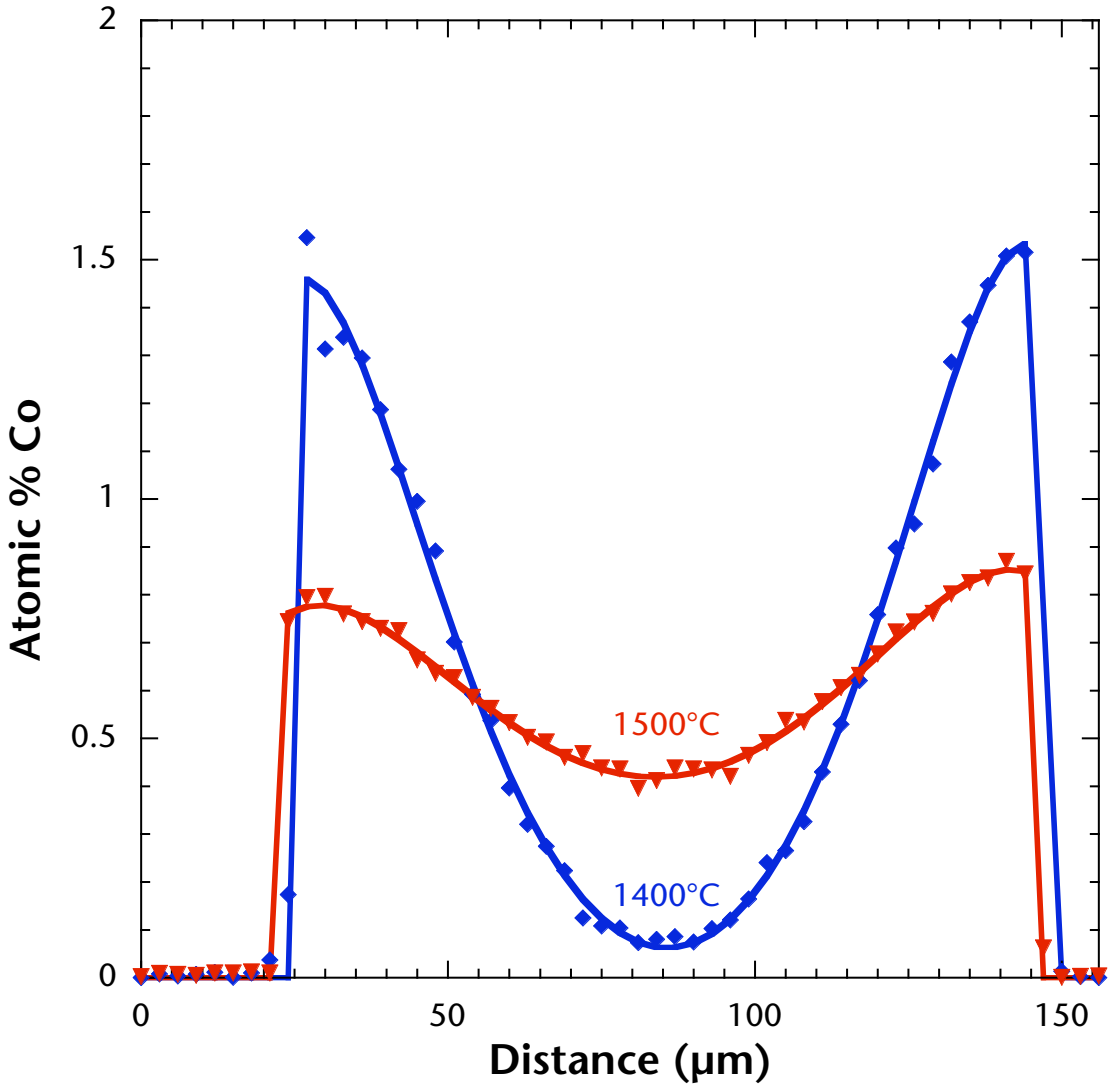

FIGURE 4.11 Co concentrations in Co/Nb/Co interlayers after bonding at 1400°C and 1500°C for 30 min.

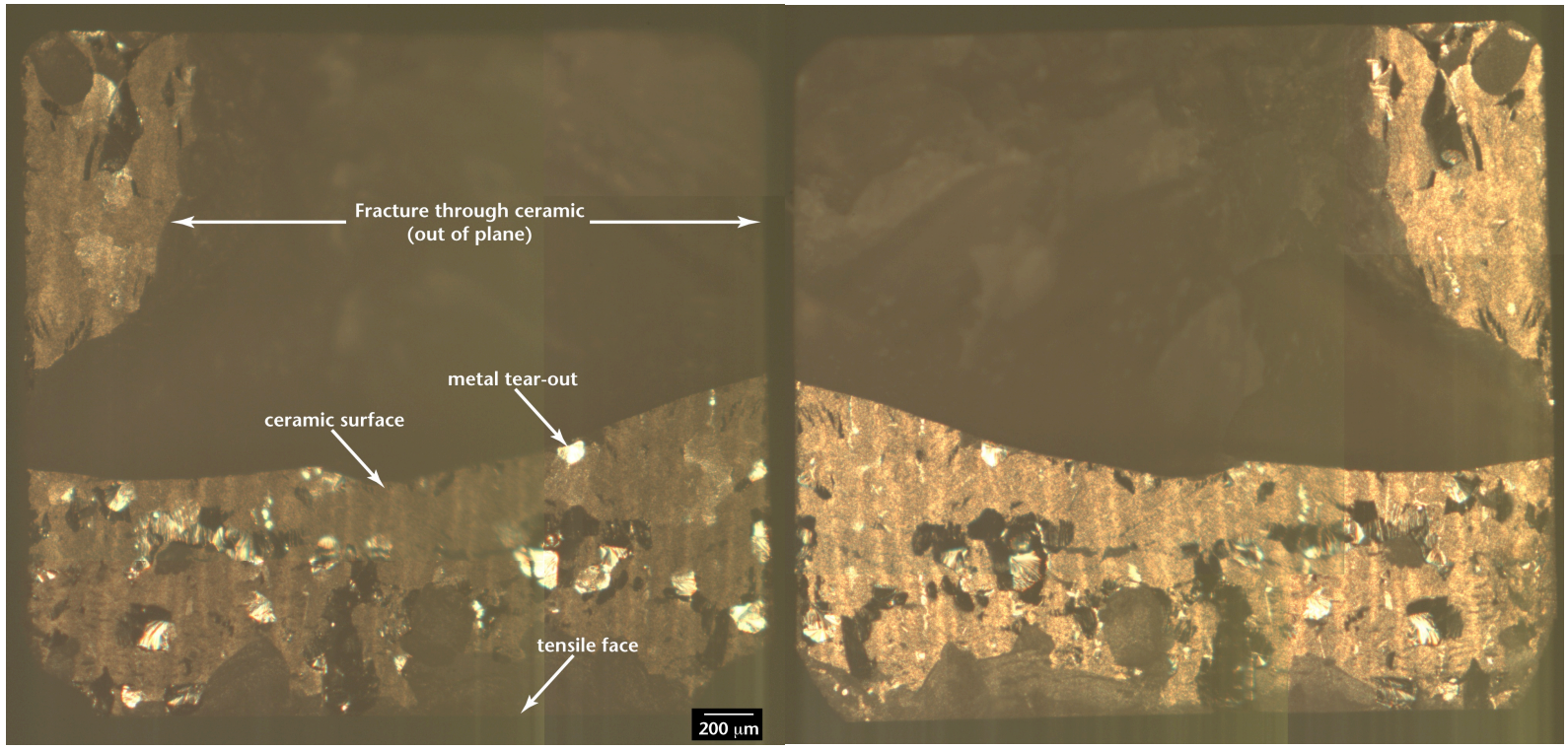

FIGURE 4.12 Fracture surfaces of a SSA-999S Al_2O_3/Ni/Nb/Ni/SSA-999S Al_2O_3 beam bonded at 1400°C, 5 min with a 2.4-MPa bonding load. (a) Ceramic side and (b) metal side of the fracture surfaces reveal that the crack initiated near the interface at the tensile surface, but propagated into the ceramic, resulting in a large ceramic fragment remaining on the metal side. The ceramic side also shows some metal tear-outs.

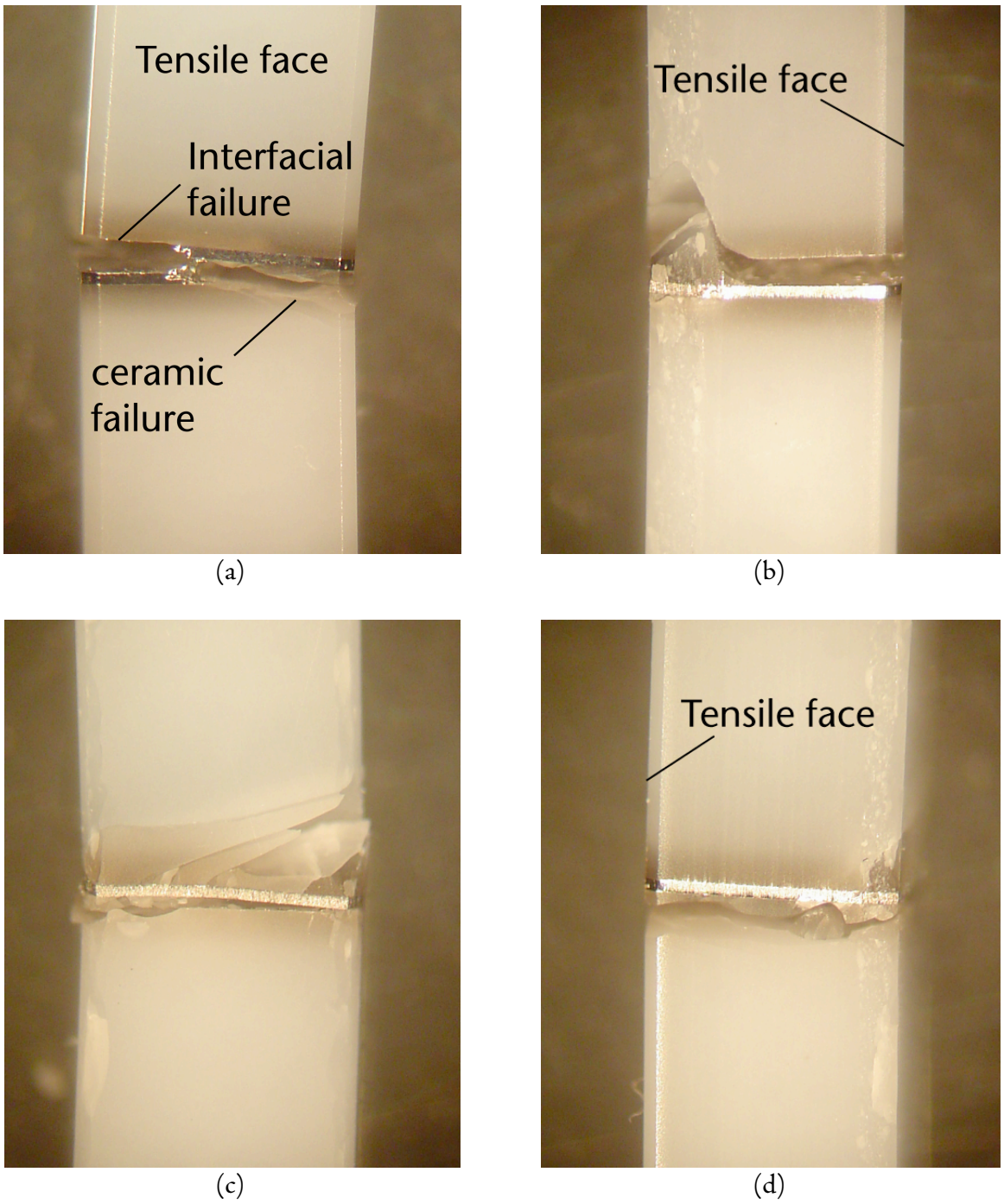

FIGURE 4.13 Macroscopic view of a SSA-999S Al_2O_3/Ni/Nb/Ni/ SSA-999S Al_2O_3 beam bonded at 1400°C for 5 min with a 2.4 MPa load after fracture test. Each image represents each faces of the beam, where (a) is the tensile surface, and (b), (c), and (d) represent the faces revealed by subsequently rotating the beam 90°, respectively. (a) shows that the crack initiated on either side of the interlayer, resulting in the metal layer tearing and the crack arresting.

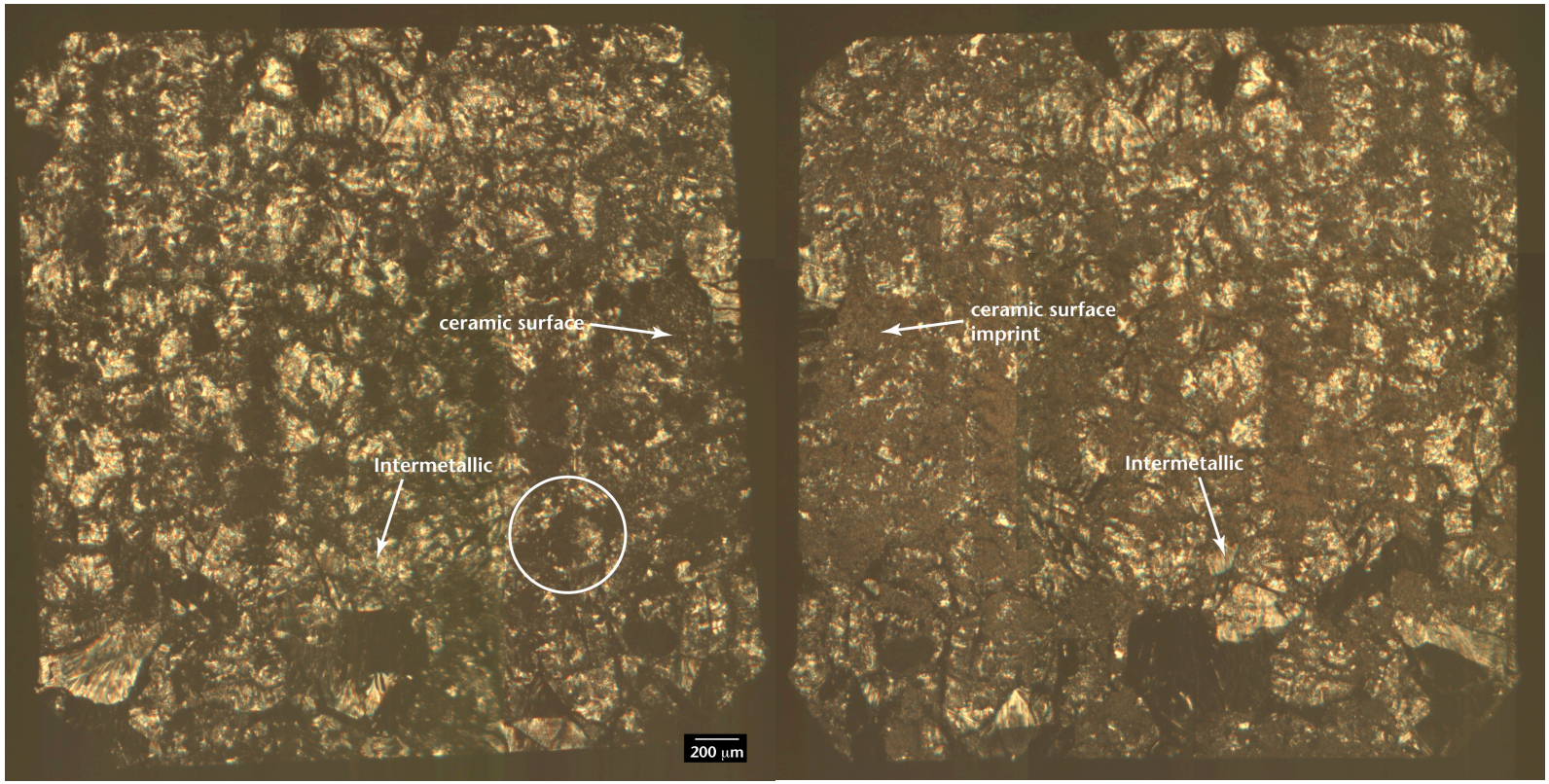

(a) (b)

FIGURE 4.14 Fracture surfaces of a SSA-999S Al_2O_3/Ni/Nb/Ni/SSA-999S Al_2O_3 beam bonded at 1400°C, 30 min with a 6.7-kPa bonding load. (a) Ceramic side and (b) metal side of the fracture surfaces reveal that the crack propagated primarily through the intermetallic layer and the metal-ceramic interface.

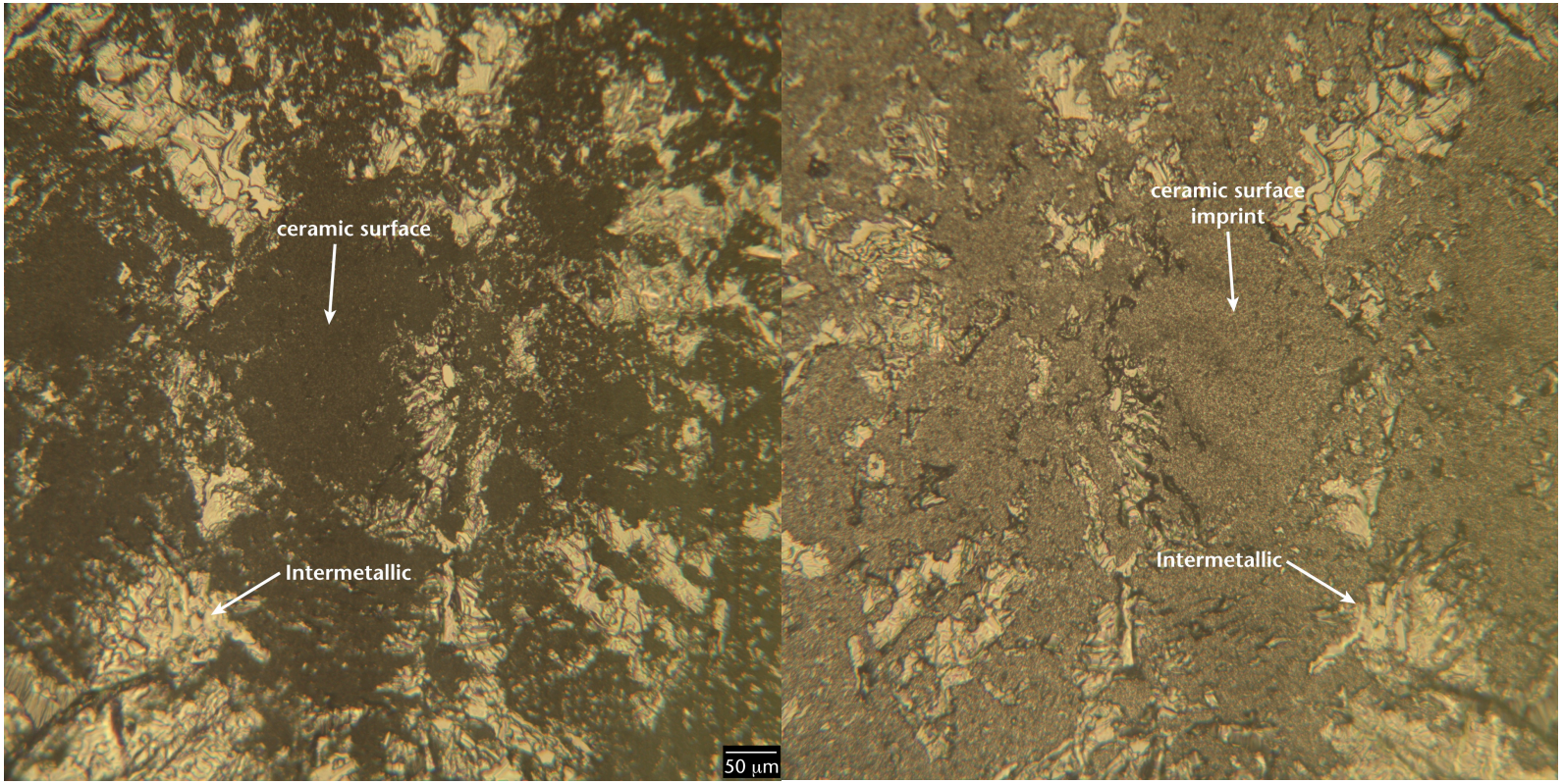

(c) (d)

FIGURE 4.14 Higher magnification optical micrographs of the (c) ceramic and (d) metal sides of the fracture surfaces corresponding to the circled region in (a). The darker regions in (c) represent the bare ceramic surface, while the bright region shows the intermetallic fracture surface.

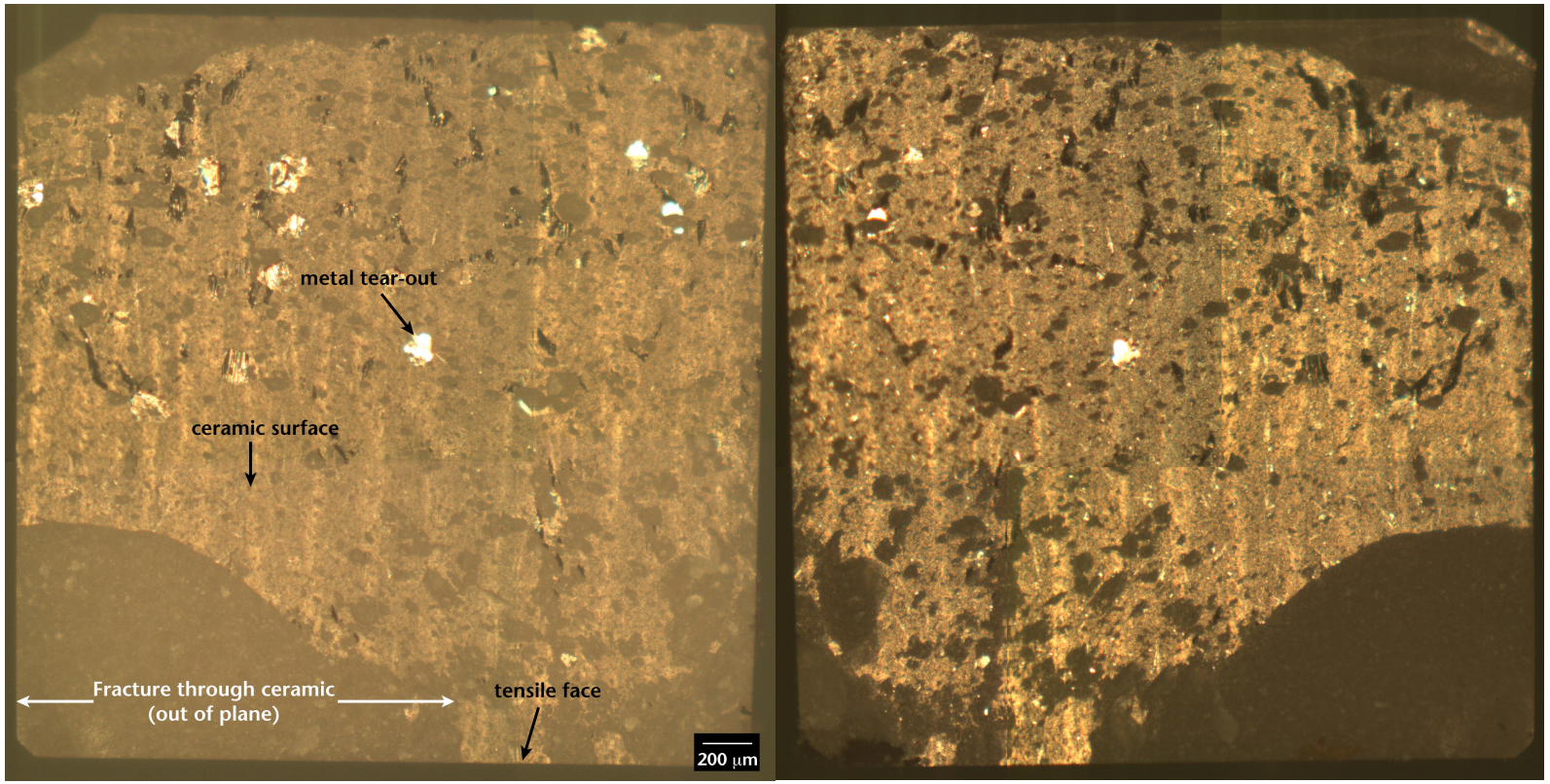

FIGURE 4.15 Fracture surfaces of a SSA-999W Al_2O_3/Co/Nb/Co/SSA-999W Al_2O_3 beam bonded at 1400°C, 30 min with a 2.4-MPa bonding load. (a) Ceramic side contains small regions of metal tear-outs. (b) The metal side of the fracture surfaces contains large Al_2O_3 fragments near the tensile surface, indicating that the crack initiated in the ceramic, but propagated through the interface.

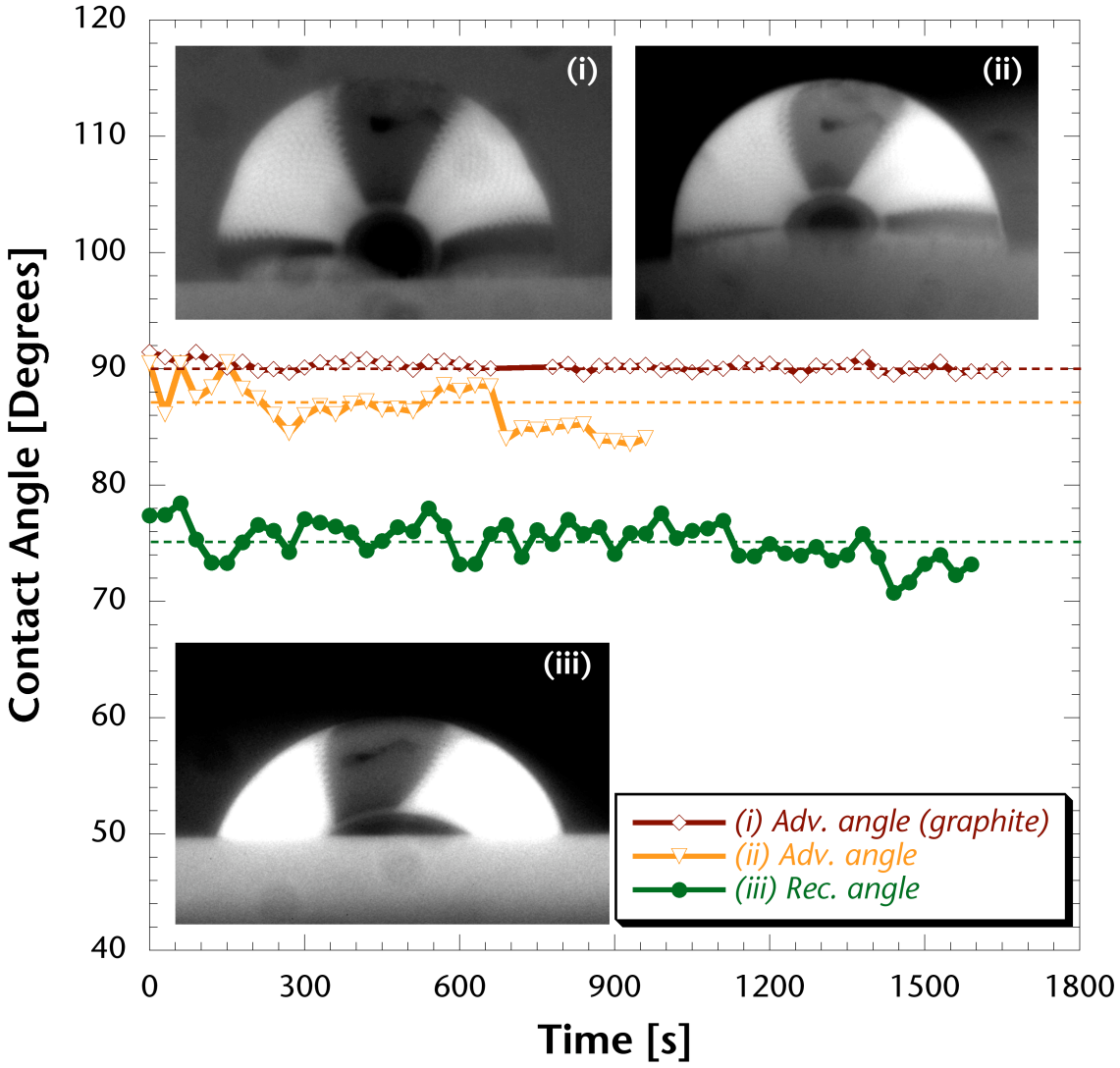

(a)

FIGURE 4.16A Plot of advancing and receding contact angles of 50:50 NiNb liquid on SSA-999W Al_2O_3 at 1400°C vs. time. Insets (i), (ii), and (iii) represent photographs of the Ni-Nb liquid droplets on the Al_2O_3 substrates. In (i), a graphite block was placed in the furnace to simulate the environment (P_{O2}) of the graphite hot press used to join samples. Note in (ii) that the substrate surface is very difficult to distinguish due to the reflection of the substrate surface on the droplet, which made it very difficult to accurately measure the contact angle.

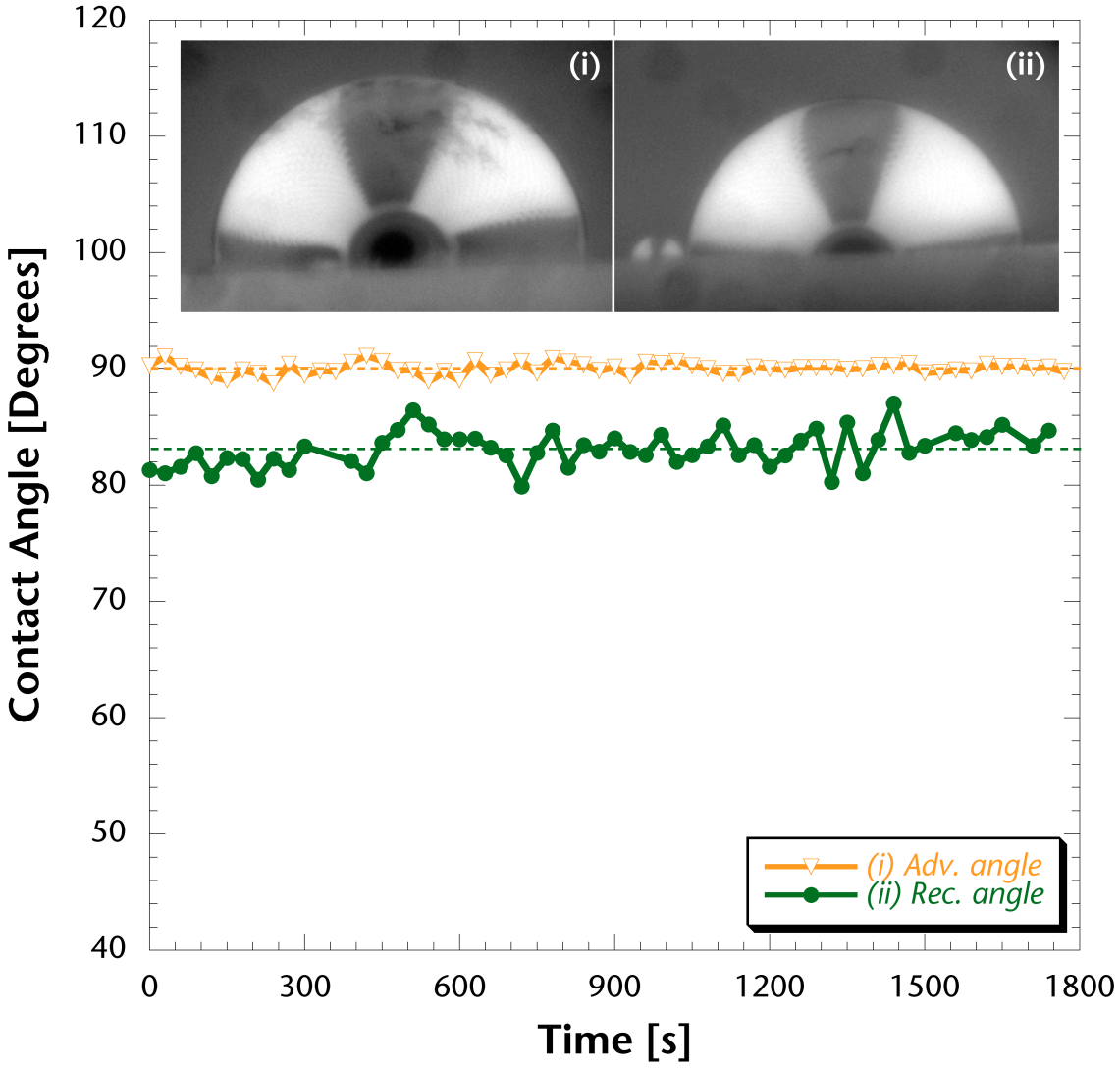

(b)

FIGURE 4.16B Plot of advancing and receding contact angles of 50:50 NiNb liquid on c-plane sapphire at 1400°C vs. time. Insets (i) and (ii) represent photographs of the Ni-Nb liquid droplets on the sapphire substrates. In (ii), a smaller droplet (on the left) detached from the larger droplet as it was receding.

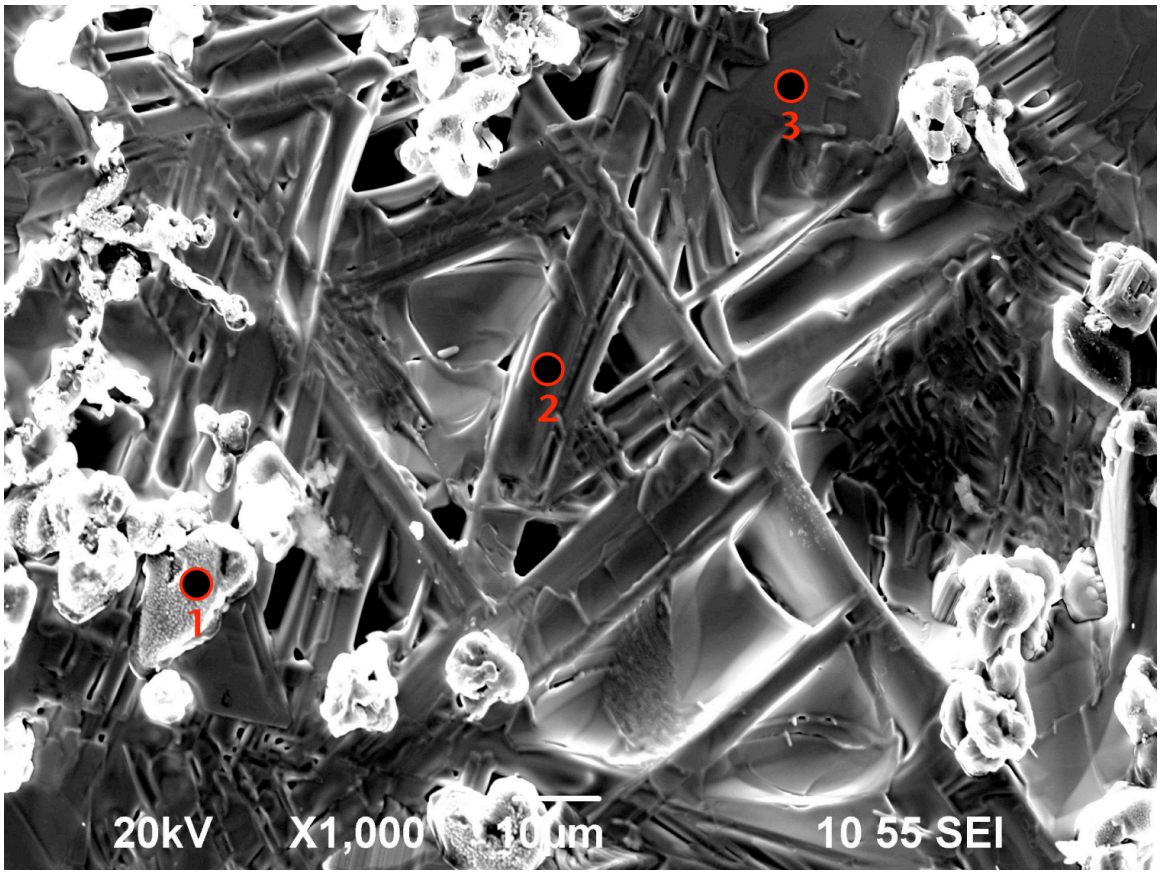

FIGURE 4.17A SEM image of the surface of a solidified NiNb droplet on sapphire. Compositions measured at points 1, 2, and 3 are shown in Table 4.1.

Elements	Overall		Point 1		Point 2		Point 3	
	wt.%	at.%	wt.%	at.%	wt.%	at.%	wt.%	at.%
Al	7.5	14.3	46.7	35.0				
Nb	43.9	24.3			43.0	32.3	59.0	52.4
Ni	33.9	29.6			57.0	67.7	41.0	47.6
O	9.5	30.3	51.2	64.7				
W	5.2	1.5	2.1	0.2				

TABLE 4.1 Compositions of the entire area and points 1, 2, and 3 in Figure 4.17a.

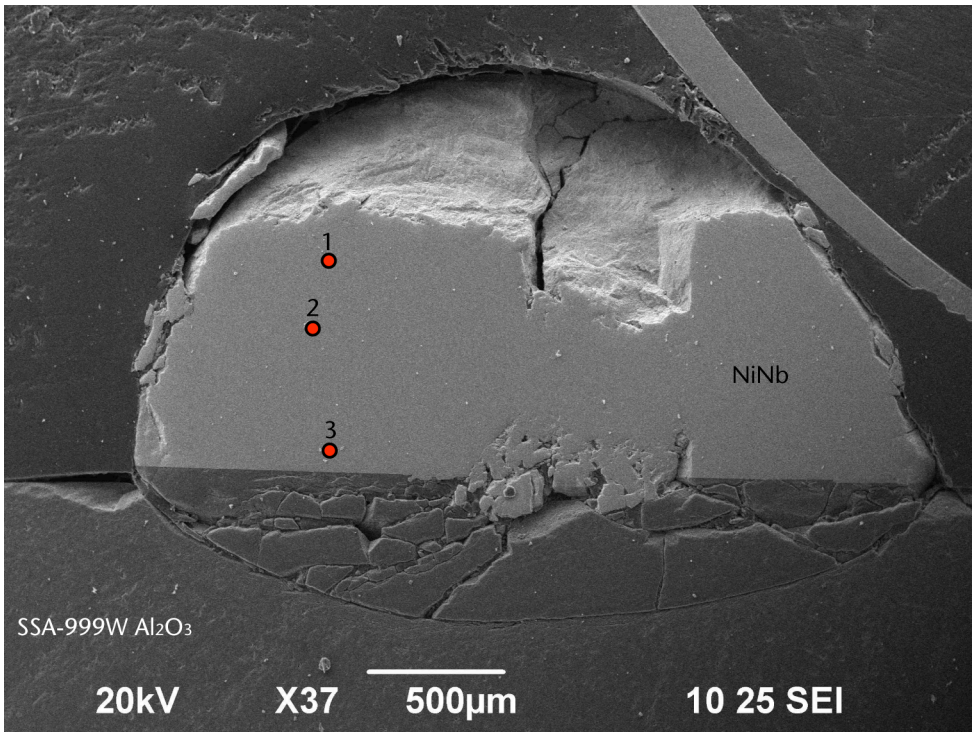

FIGURE 4.17B SEM image of the cross-sectioned "receding" 50:50 NiNb droplet on SSA-999W Al_2O_3. Compositions measured at points 1, 2, and 3 were virtually identical at 39 wt.% Ni and 61 wt.% Nb. The lower Ni concentration compared to the initial alloy may be due to preferential evaporation of Ni during the experiment.

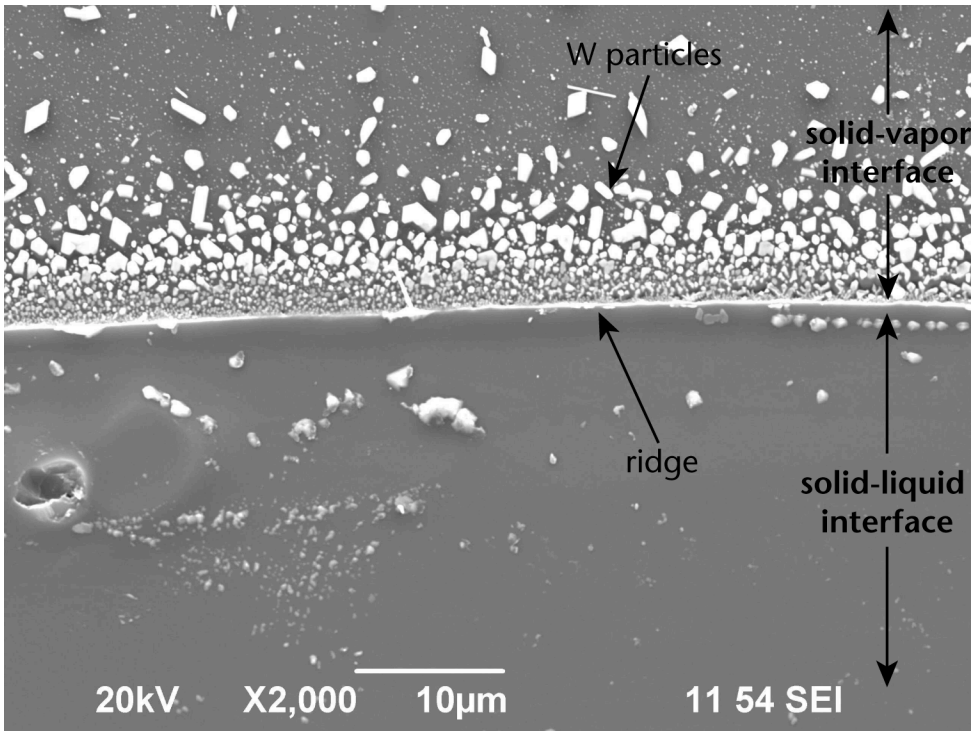

FIGURE 4.18 SEM image of sapphire surface after the NiNb droplet was detached. Image was taken with a 17° tilt to help distinguish the ridge. Note the small W-rich particles that nucleated on the outer perimeter of the ridge.

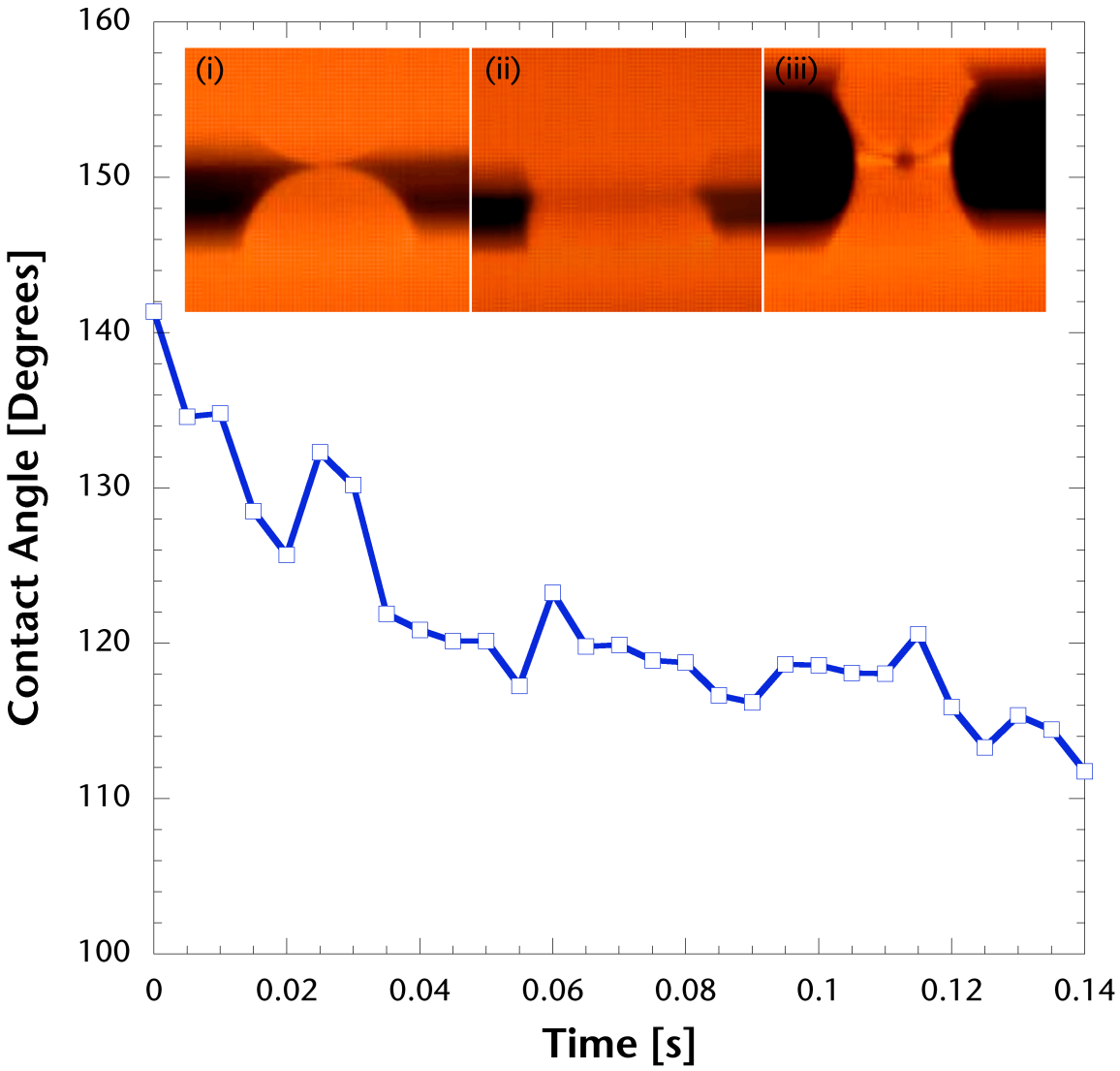

FIGURE 4.19 Advancing contact angles of 50:50 NiNb alloy on SSA-999W Al_2O_3 vs. time measured using the drop transfer method. (i) The droplet prior to the top substrate making contact. (ii) After the top substrate has contacted the droplet, the liquid spread on the surface and formed advancing contact angles. (iii) The top substrate was raised from the contact position, which allowed the liquid to retract and form a receding contact angle.

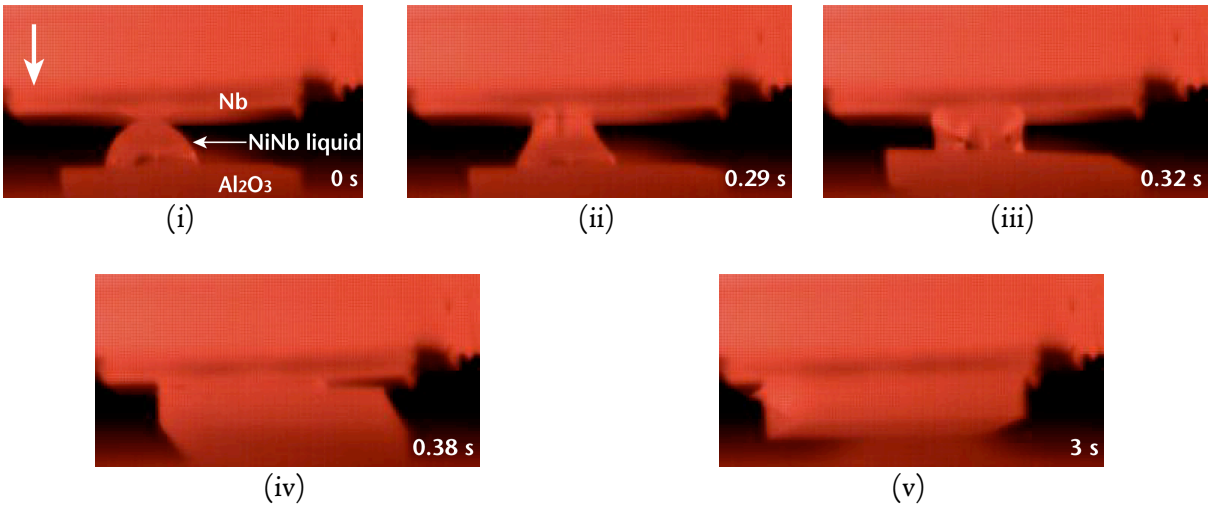

FIGURE 4.20A Video stills of drop-transfer experiment using 50:50 NiNb liquid between SSA-999W Al_2O_3 and Nb substrates. Within 0.5 s of the Nb substrate making contact with the liquid droplet, the liquid filled the gap between the two surfaces and drew the Al_2O_3 substrate in contact with the Nb (iv and v).

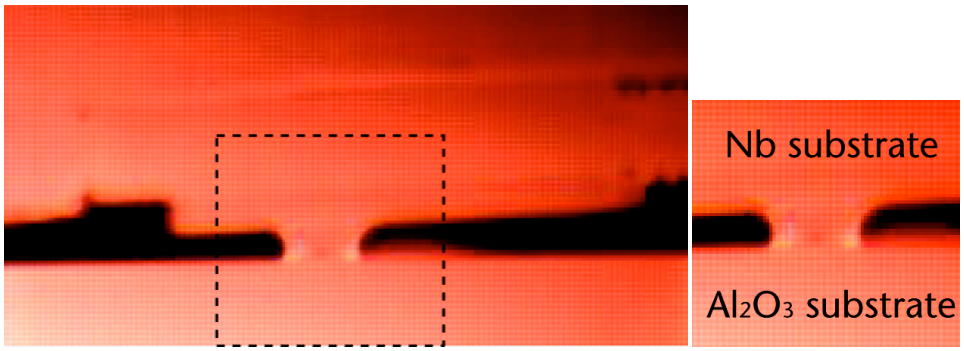

FIGURE 4.20B Video still of drop-transfer experiment using 50:50 NiNb liquid between SSA-999W Al_2O_3 and Nb substrates. The image was taken several seconds after the top Nb substrate made contact with the droplet, when the liquid remained stationary.

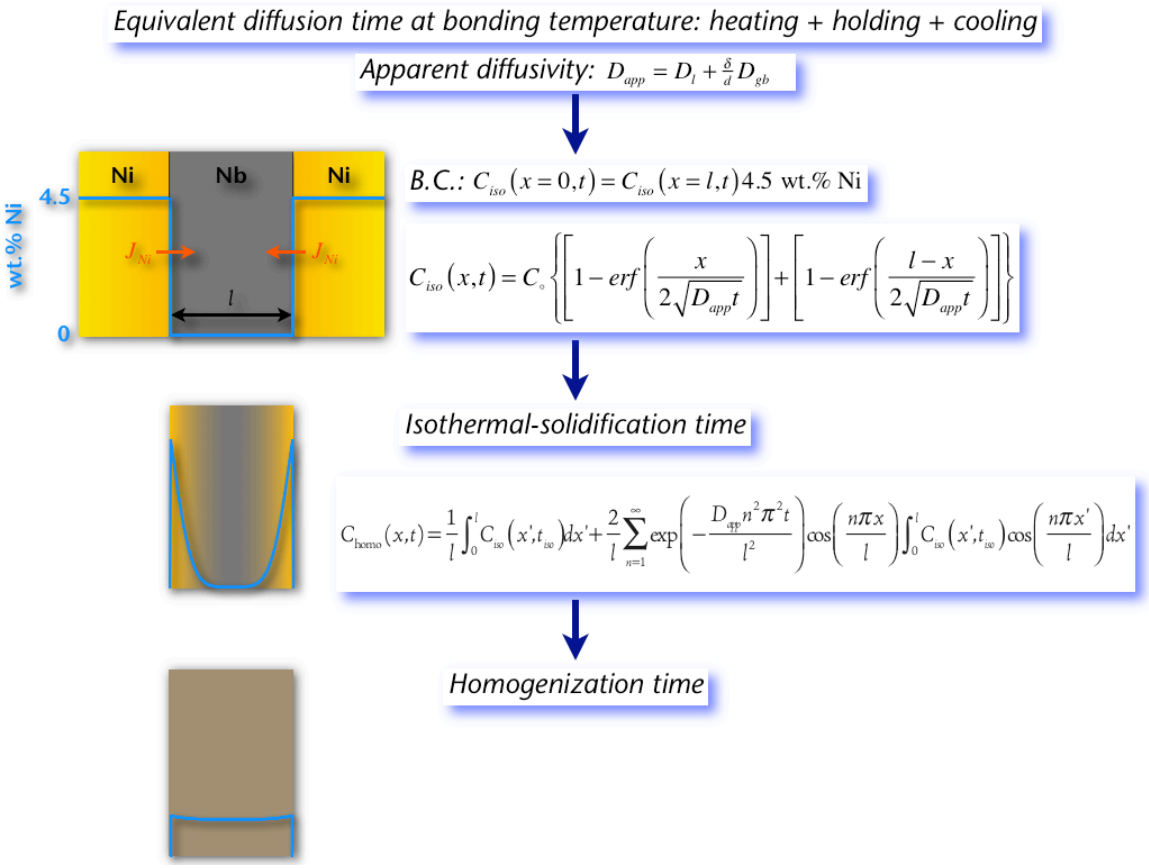

FIGURE 4.21 Schematic of isothermal-solidification and homogenization time calculations.

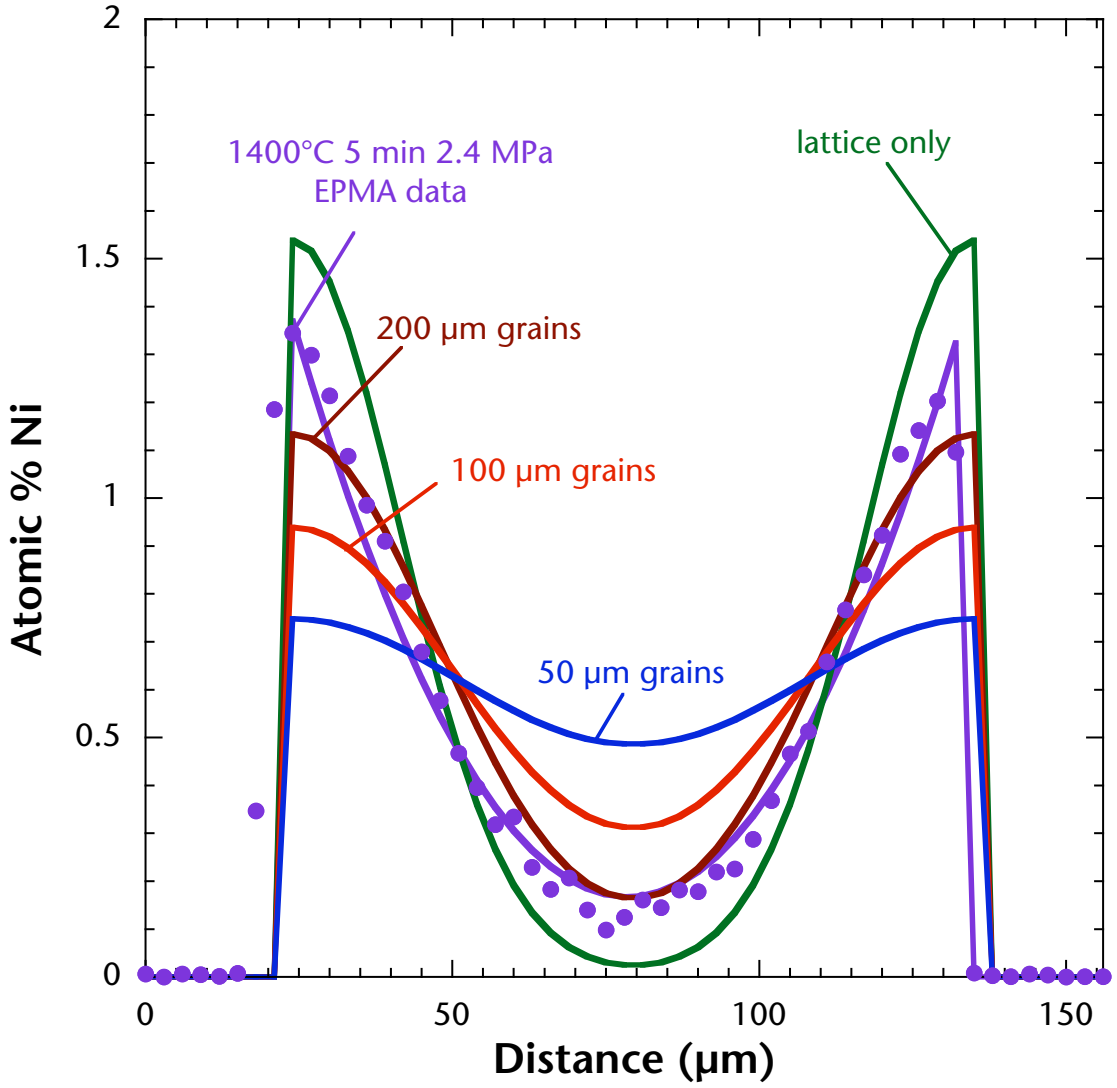

FIGURE 4.22A Comparison between the measured and calculated Ni-concentration profiles for a 5-min isothermal-holding time at 1400°C. Apparent diffusivities of Ni in polycrystalline Nb (50-, 100-, and 200-μm Nb grain sizes) and single-crystalline Nb were used to calculate the profiles.

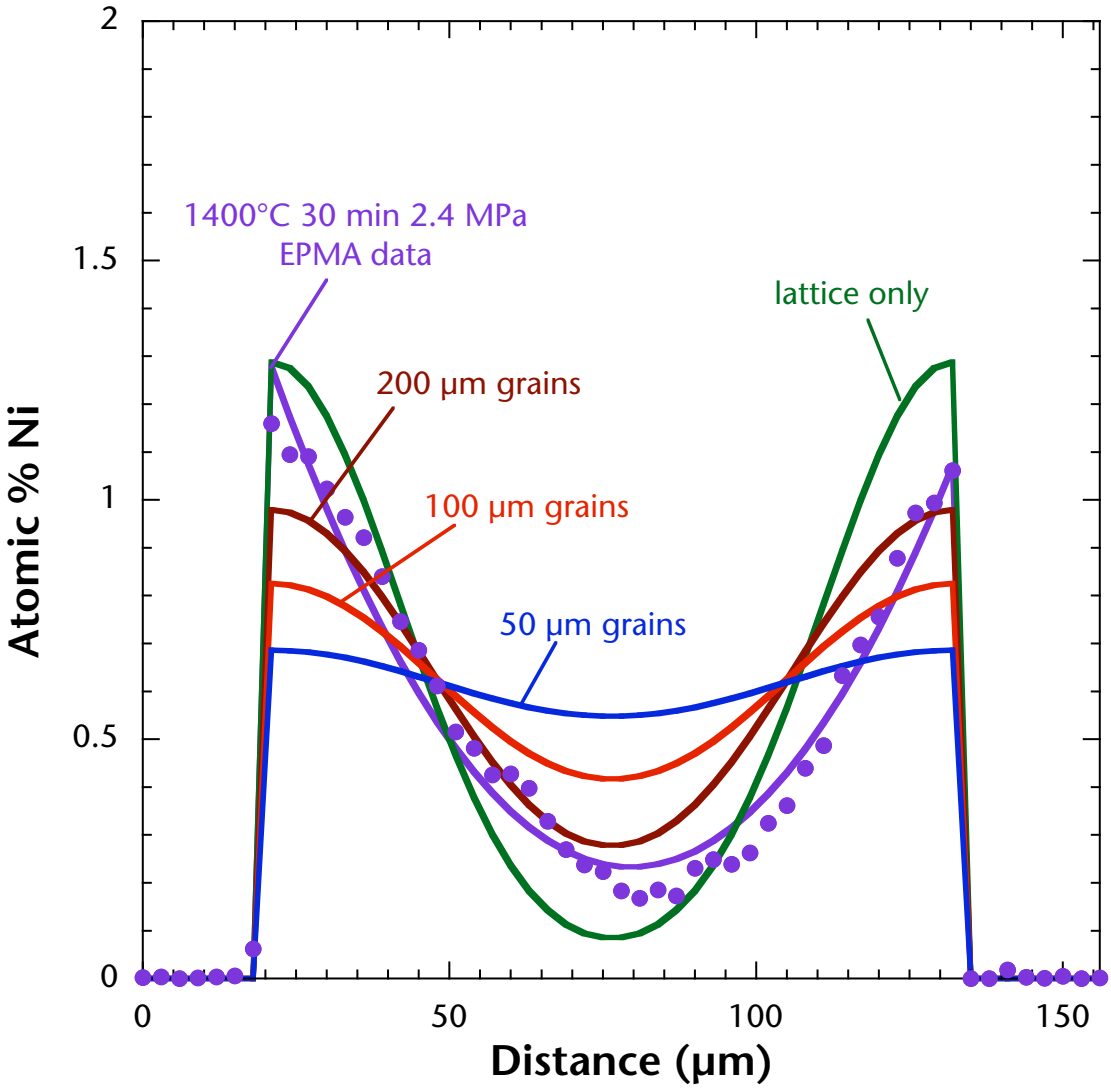

FIGURE 4.22B Comparison between the measured and calculated Ni-concentration profiles for a 30-min isothermal-holding time at 1400°C.

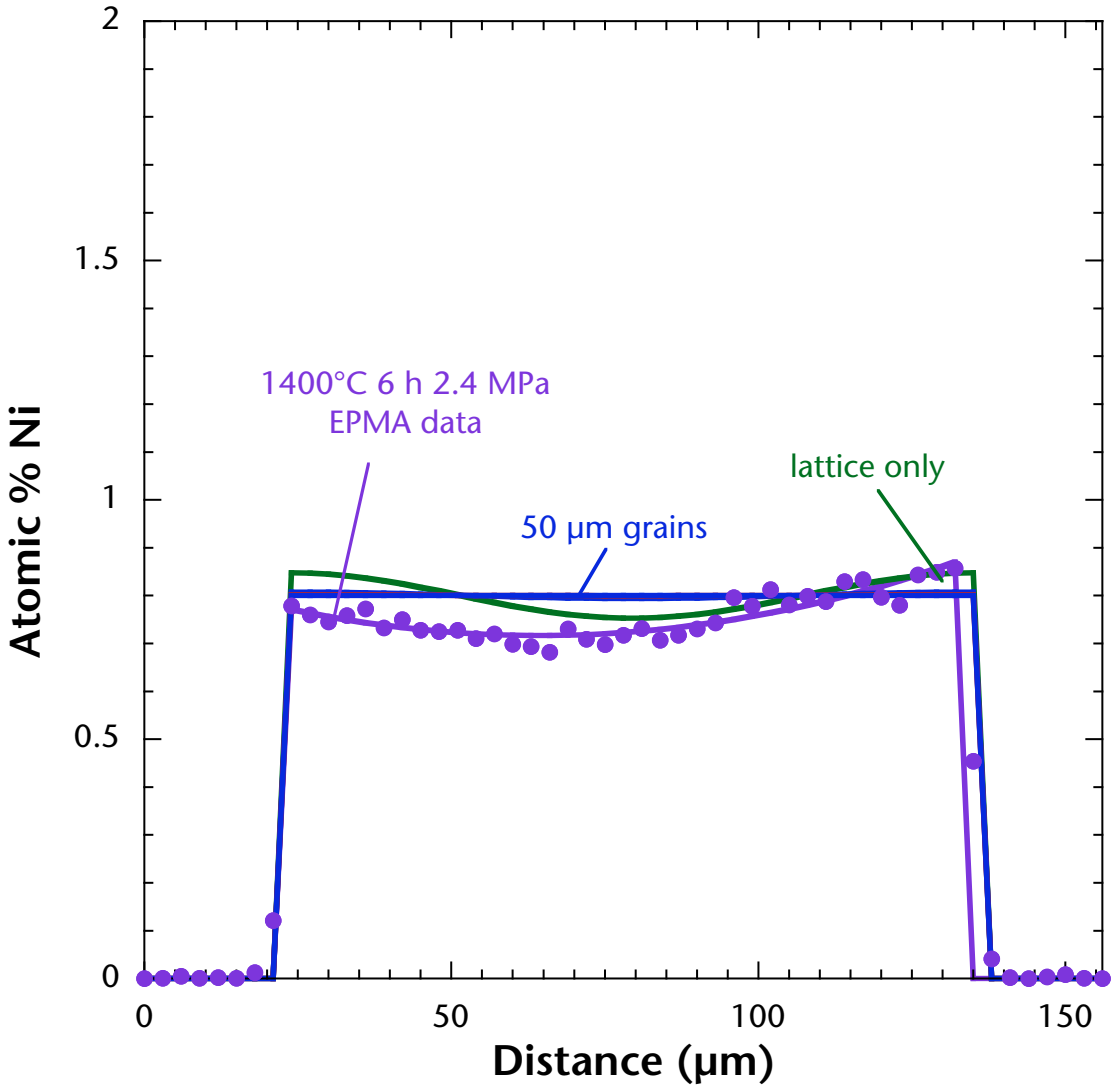

FIGURE 4.22c Comparison between the measured and calculated Ni-concentration profiles for a 6-h isothermal-holding time at 1400°C.

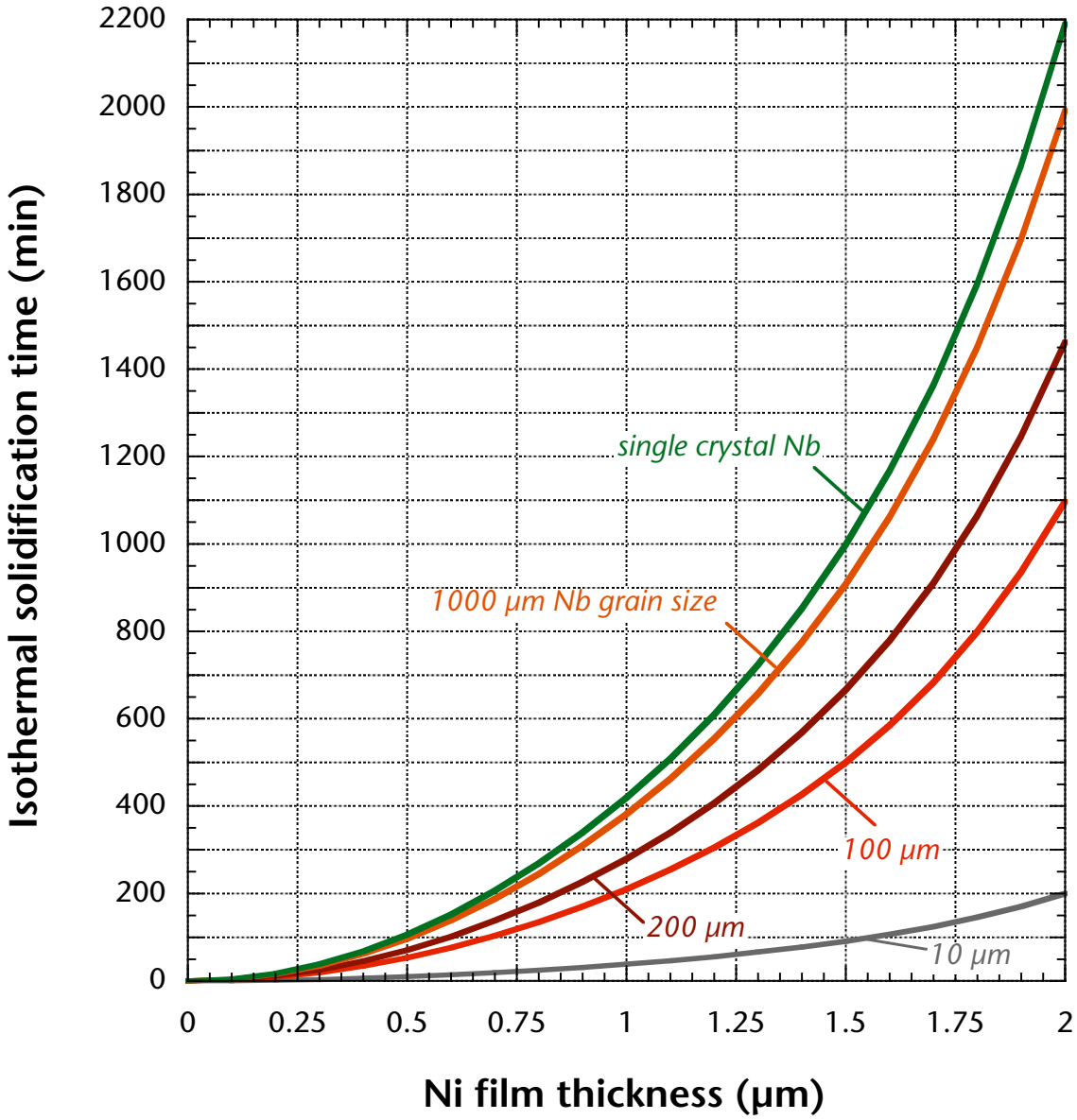

FIGURE 4.23 Plot of isothermal-solidification time vs. the initial Ni cladding layer thickness for single-crystal Nb and polycrystalline Nb with 1000-, 200-, 100-, and 10-μm average grain sizes.

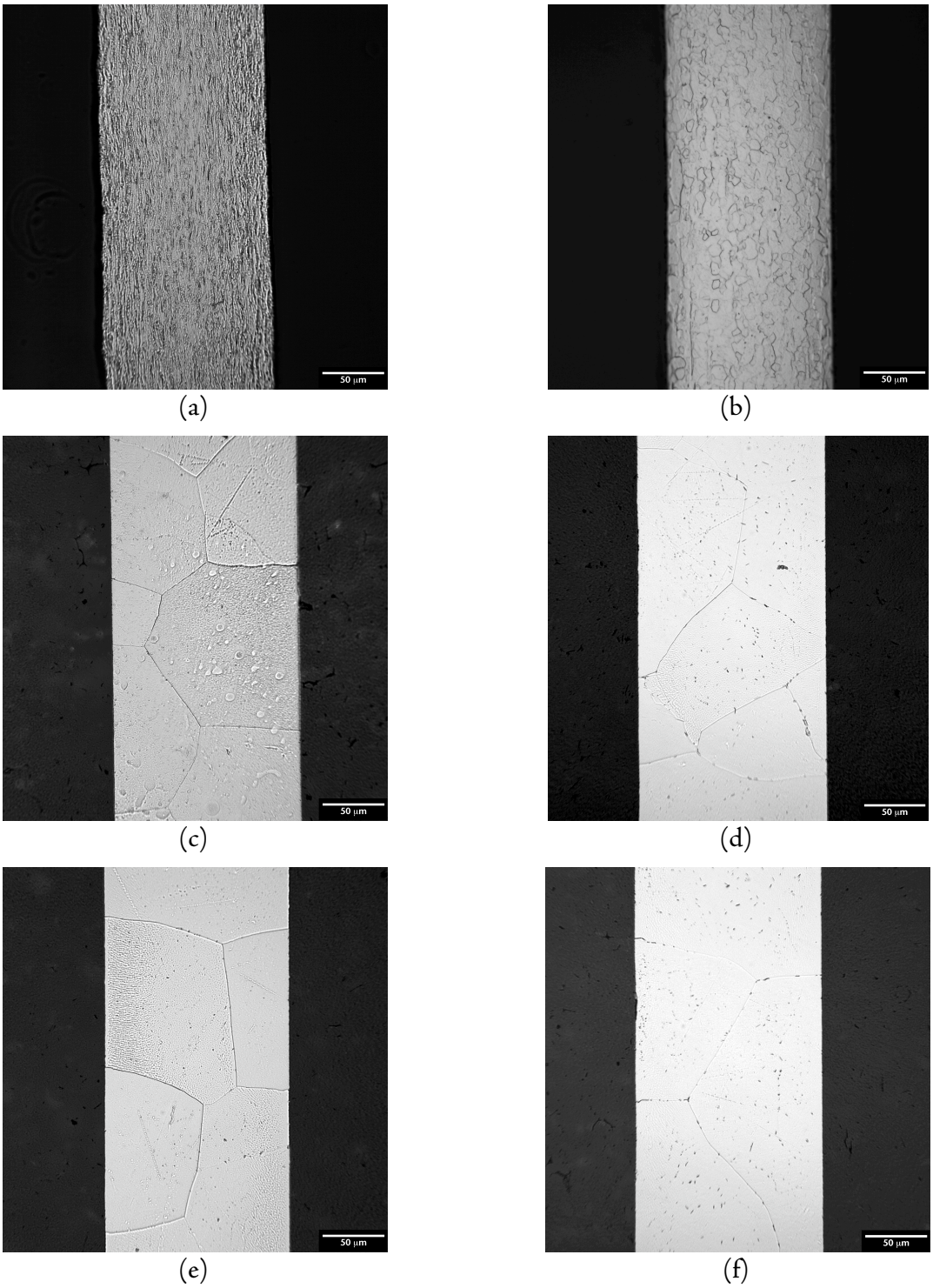

FIGURE 4.24 Optical micrographs of cross-sectioned Nb foils before and after joining. As-rolled (a) and recrystallized (rolled and annealed at 1000°C for 1 h) (b) Nb foils. Joined interlayers consisting of the as-rolled Nb bonded at 1400°C for 5 min (c) and 30 min (e). Interlayers consisting of the recrystallized Nb bonded at 1400°C for 5 min (d) and 30 min (f).

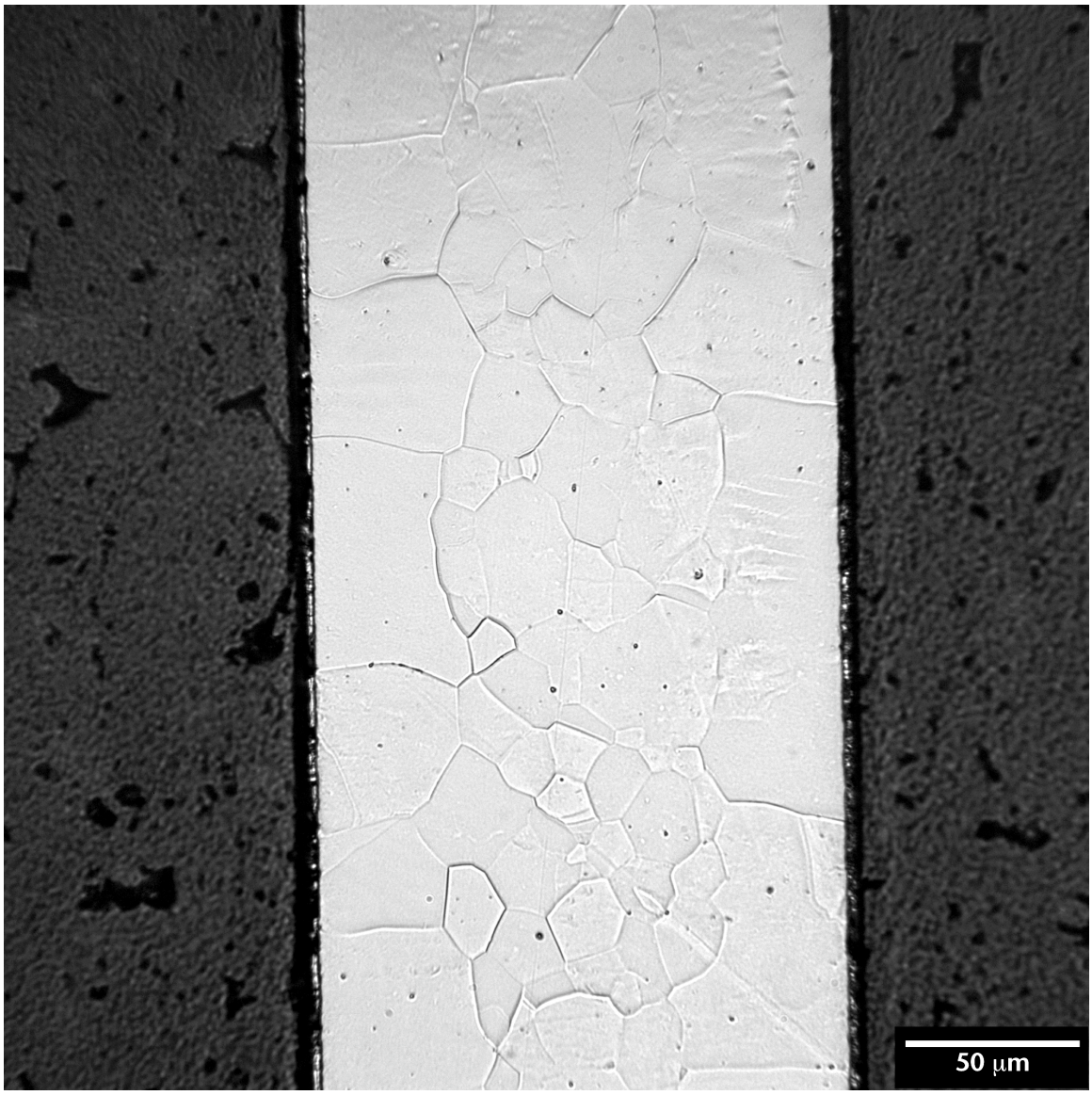

FIGURE 4.25 Optical micrograph of Ni/recrystallized-Nb/Ni interlayer after joining at ≈1000°C for 5 min. Since bonding took place below the eutectic temperature (1178°C), intermetallic layers formed along the metal-ceramic interfaces. The Nb core layer consists of larger grains (≈110 μm) near the interfaces and smaller grains in the center (≈33 μm), indicating that diffusion-induced grain-boundary migration occurs during bonding. Similar microstructures were observed when as-rolled and as-received Nb core layers were employed.

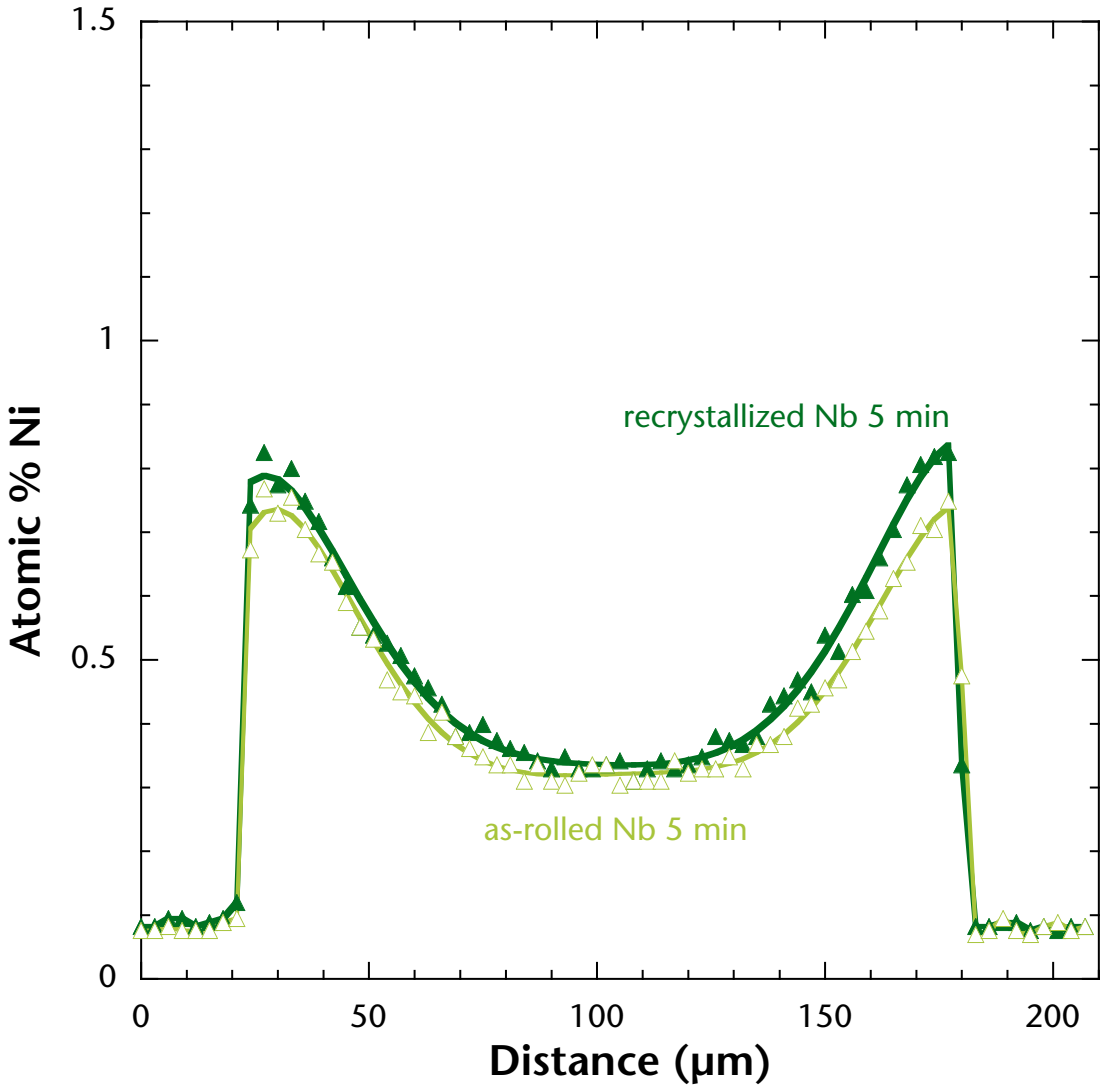

FIGURE 4.26A Ni concentration profiles obtained through EPMA. The filled data points represent the Ni concentrations in the recrystallized Nb, while the unfilled points represent the Ni concentrations in the as-rolled Nb after joining at 1400°C for 5 min.

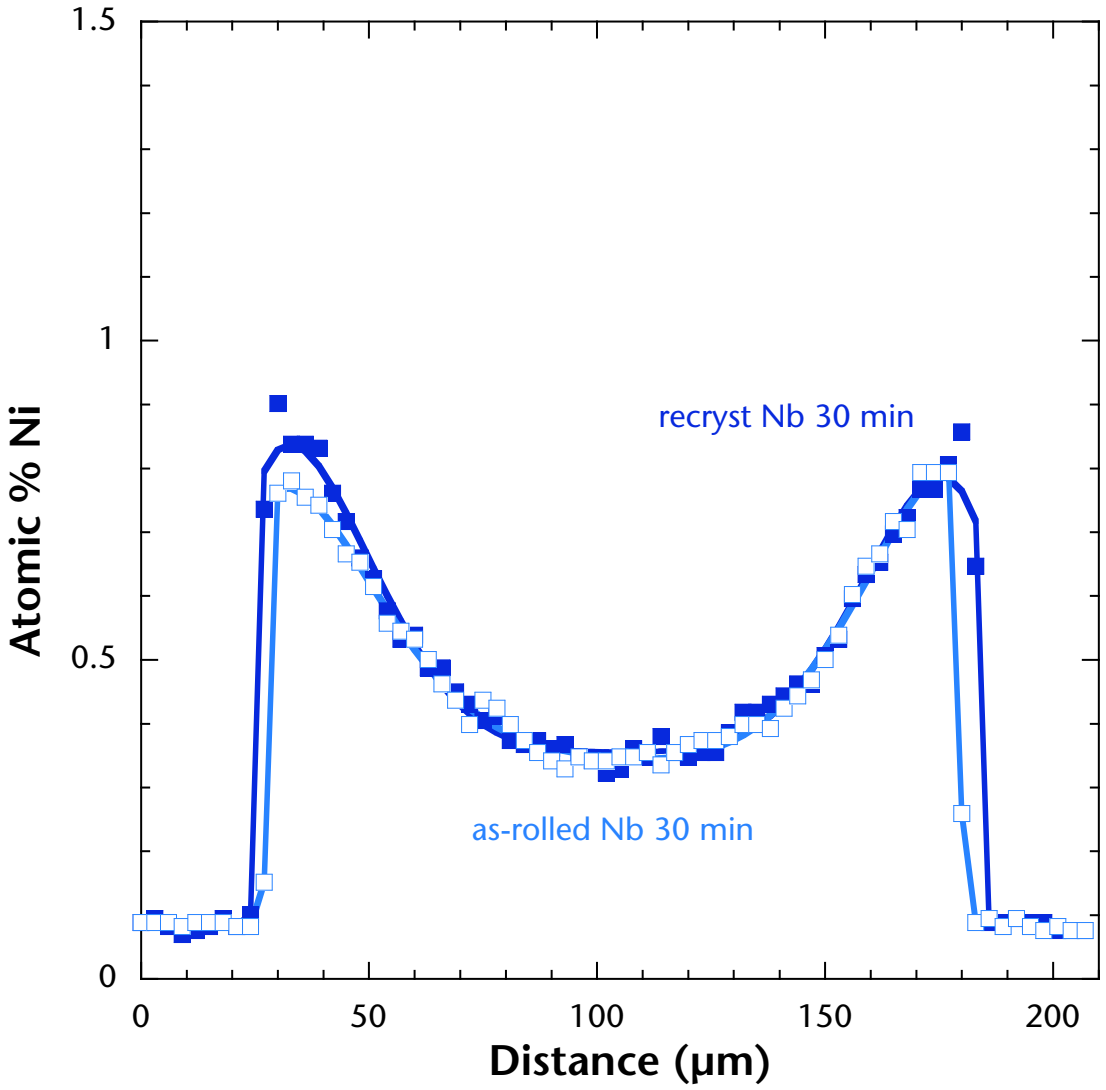

FIGURE 4.26B Ni concentration profiles obtained through EPMA. The filled data points represent the Ni concentrations in the recrystallized Nb, while the unfilled points represent the Ni concentrations in the as-rolled Nb after joining at 1400°C for 30 min.

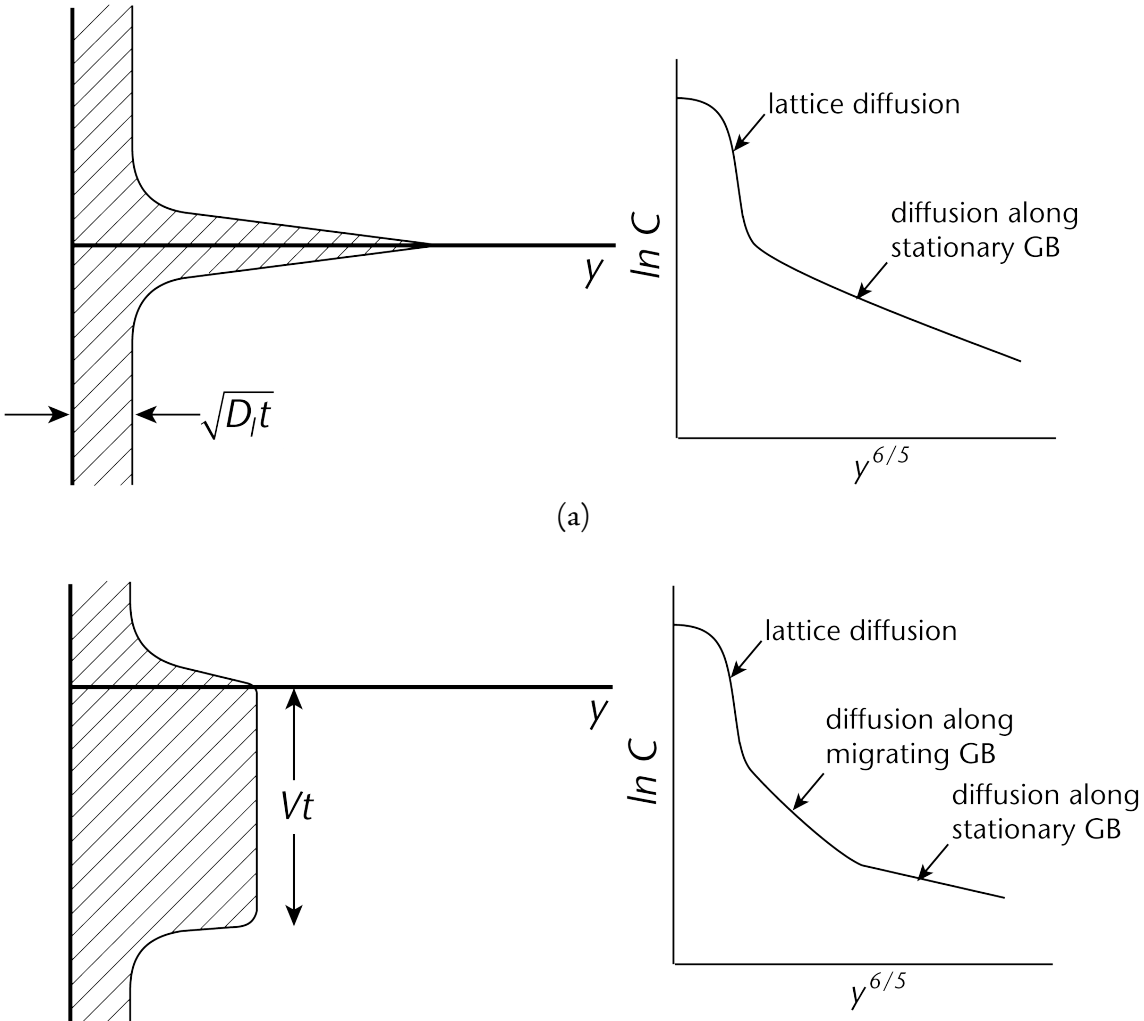

FIGURE 4.27 Schematic of the effects of (a) stationary and (b) migrating grain boundaries on the solute concentration and the corresponding *ln C* vs. $y^{6/5}$ plots, after Mishin.[106]

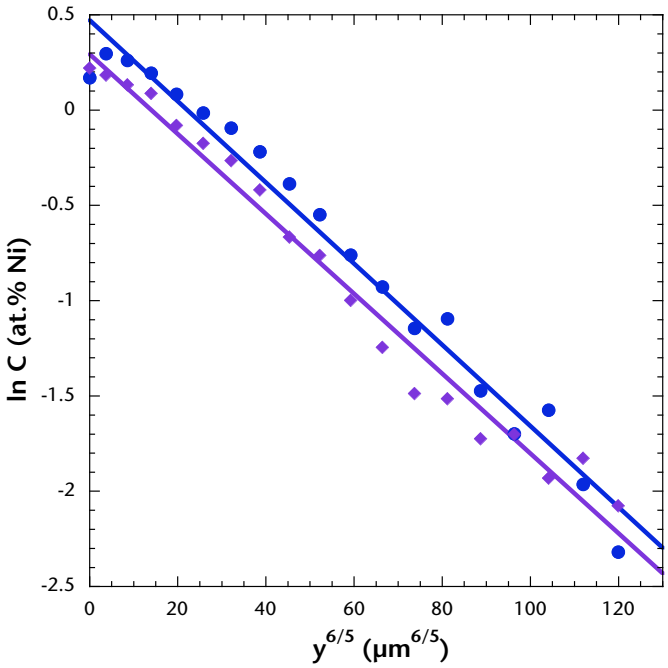

(a)

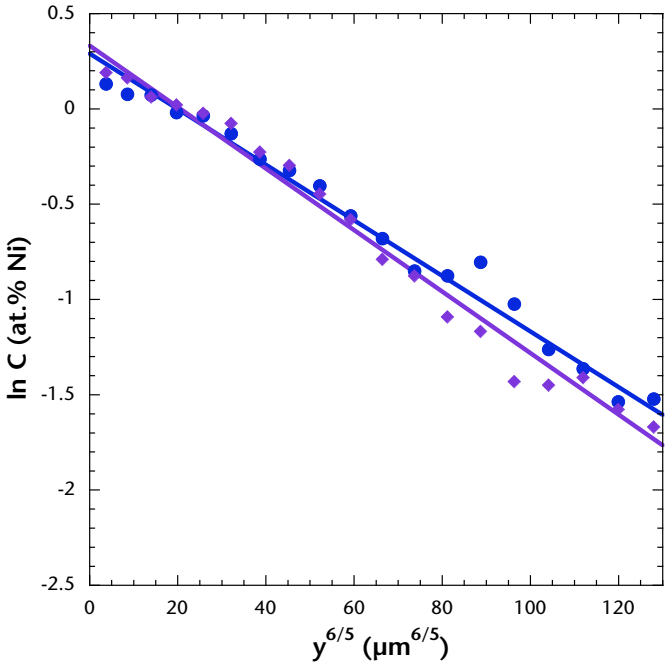

(b)

FIGURE 4.28 *ln* C vs. $y^{6/5}$ plots for the Ni/Nb/Ni interlayers containing as-received Nb core layer bonded at 1400°C with 5-min (a) and 30-min (b) holding times and 2.4-MPa bonding pressure. The ● and ◆ data points represent Ni concentrations from each half of the interlayers.

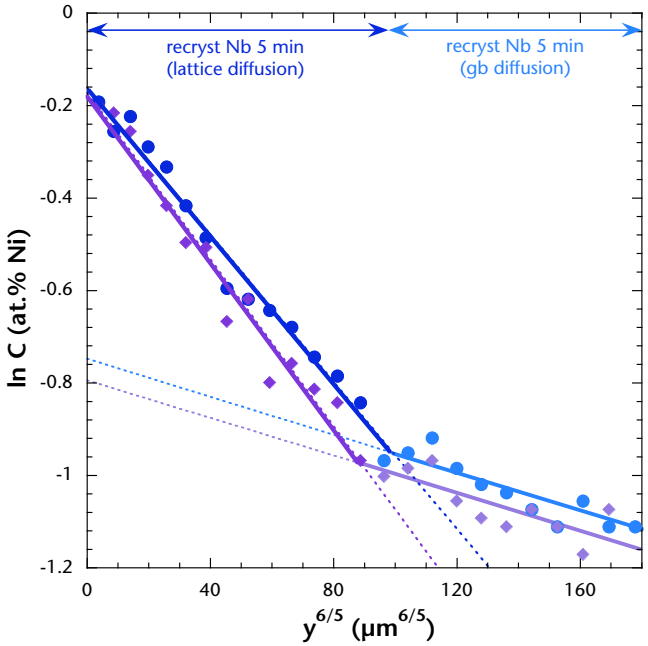

(c)

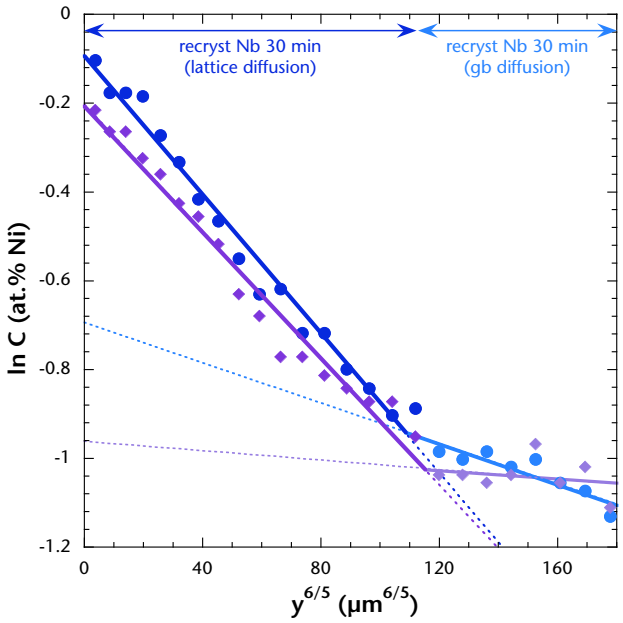

(d)

FIGURE 4.28 *ln* C vs. $y^{6/5}$ plots for the Ni/Nb/Ni interlayers containing recrystallized Nb core layers, bonded at 1400°C with 5-min (c) and 30-min (d) holding times. There appears to be two distinct regions where lattice and grain-boundary diffusion dominated.

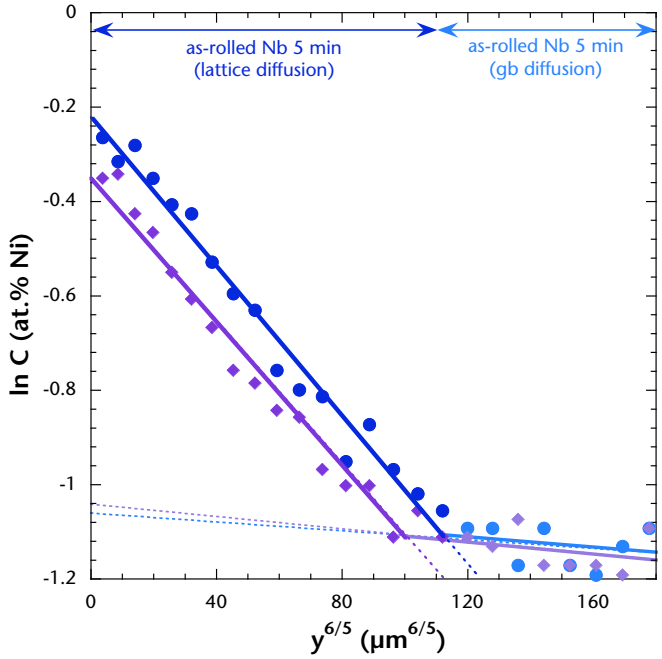

(e)

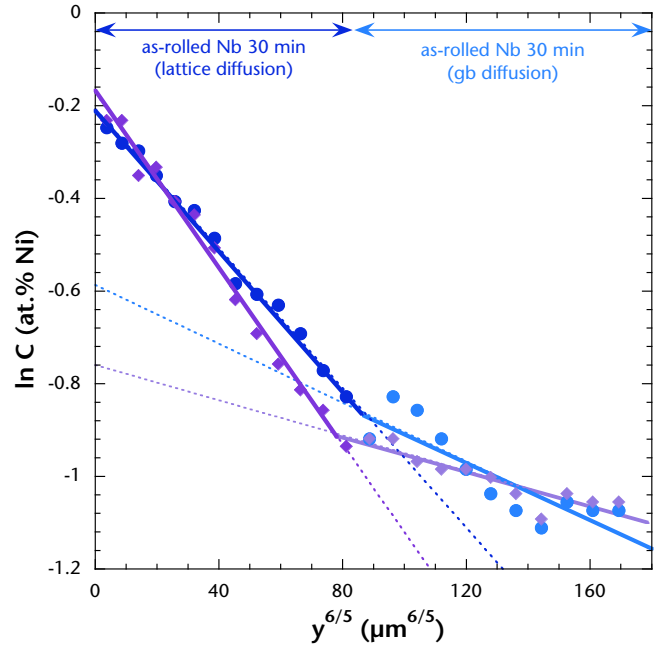

(f)

FIGURE 4.28C *ln* C vs. $y^{6/5}$ plots for the Ni/Nb/Ni interlayers containing as-rolled Nb core layers, bonded at 1400°C with 5-min (e) and 30-min (f) holding Similar to the concentrations in the recrystallized Nb, the concentration slopes change $(3 \text{ to } 4)\times\sqrt{D_l t}$ from the interface.

5. Conclusion

Conventional ceramic joining methods, such as brazing and solid-state diffusion bonding, have characteristic advantages and disadvantages. Brazing is a fast, cost-effective joining process because it simply involves melting and solidifying a braze layer to form a permanent bond between the parts being joined. Metallization prior to brazing, or active-metal brazing promote good wetting behavior on ceramics and are widely used to produce reliable ceramic joints. However, metallization requires multiple high-temperature processes, while active-metal brazes tend to form brittle reaction layers that can limit joint strengths. It is difficult to produce high-temperature brazed joints because the service temperatures are typically well below the bonding temperatures. In contrast, solid-state diffusion bonding has the potential to produce high-strength, high-temperature joints, but requires significantly longer bonding times, higher bonding pressures, and smoother surface finishes. TLP bonding with multilayer interlayers is a viable alternative to these methods as it can produce high-temperature joints using reduced bonding temperatures and short bonding times.

In this study, model multilayer Ni/Nb/Ni and Co/Nb/Co interlayers were used to join high-strength, high-purity Al_2O_3. These interlayer materials combinations were chosen based on their relatively modest eutectic temperatures, high Nb solubility limits in the liquid, high MPD diffusivity-solubility products, and high re-melt (solidus) temperatures. Since Nb nearly matches the coefficient of thermal expansion of Al_2O_3 over a wide temperature range, residual stresses due to thermal contraction were minimized. When SSA-999S Al_2O_3 was joined using Ni/Nb/Ni interlayer at 1400°C, fracture strengths >500 MPa were obtained, with most of the samples failing in the ceramic, even when joined using isothermal-holding times as short as 5 min. No other previously studied TLP interlayers have produced Al_2O_3 joints with such high fracture strengths in combination with short bonding times.

The minimum bonding time in TLP bonding is typically determined by the isothermal-solidification time, which is a function of the solid-state diffusion rate of the MPD (Ni or Co) in the core layer (Nb). While Ni and Co are anomalously fast diffusers in Nb, one of the most effective methods of decreasing the solidification time is to reduce the amount of liquid retained in the joint. Provided that the liquid can sufficiently wet the joining surfaces, the minimum liquid volume is determined by the interfacial gap volume, which is a function of bonding pressure and joining-surface roughness. When a 2.4-MPa bonding pressure was used, excess liquid extruded out of the joint, substantially decreasing the amount of Ni that must diffuse into the Nb for complete isothermal solidification to occur. As a result, a 5-min holding time at 1400°C was sufficient to produce strong, reliable joints. In contrast, when a 6.7-kPa bonding pressure was used, most of the liquid was retained in the joint, resulting in the formation of intermetallic layers due to solidification during cooling, even after a 6-h isothermal hold. The fracture surfaces of these joints showed failures occurred along the intermetallic layers, but the average fracture strengths were still comparable that of the bulk SSA-999W Al_2O_3.

In any liquid-based joining processes, the liquid must fill interfacial gaps, as well as any local asperities on the joining surfaces to produce essentially flaw-free interfaces. A liquid can spontaneously flow into a gap between two rigid, parallel surfaces when the sum of the two contact angles is <180°. In TLP bonding, the liquid forms in contact with both the ceramic and the core-layer metallic surfaces, which enables most non-reactive liquid metals to satisfy this condition. However, in practice, it has been found that the liquid must form lower contact angles on the ceramic surfaces to avoid

formation of local flaws. For instance, a pure liquid Ni would form a contact angle sum <180° between Nb and Al_2O_3 surfaces, but because it forms an obtuse contact angle (≈120°) on Al_2O_3, any local asperities on the Al_2O_3 surface would not be filled and remain as interfacial flaws. However, because the liquid film that forms between the Nb core and the Al_2O_3 also contains a significant amount of Nb, a different wetting behavior was anticipated. Sessile-drop experiments revealed that a 50:50 NiNb liquid forms an ≈90° equilibrium contact angle on SSA-999W Al_2O_3 in high vacuum. It appears that the addition of Nb may increase the amount of Al_2O_3 dissolved in the liquid. The dissolved Al atoms or Nb-O clusters may adsorb onto the liquid-solid interface, thereby decreasing the interfacial energies and further promote liquid spreading. The relatively good wetting behavior of the Ni-Nb TLP on Al_2O_3 resulted in the liquid filling surface asperities and eliminating interfacial flaws to produce robust metal-ceramic interfaces.

Once the liquid forms and fills the interfacial gaps and voids, it must isothermally solidify rapidly to minimize bonding time. The isothermal-solidification time is often difficult to predict, as evidenced by previous efforts to model metal-metal TLP bonding, and thus, has been found through empirical studies, which can be tedious and time-consuming. An effective method of estimating the processing conditions would greatly facilitate future interlayer designs and joining processes. In the current study, analytical solutions to Fick's law were used to calculate the Ni-diffusion profiles, which were quantitatively compared with the measured profiles. Although the current model lacks the ability to properly account for the effects of Nb-grain growth on the diffusion rates, it provided Ni concentrations that were relatively close to the measured quantities when assuming an average grain size of 200 μm, which was similar to the grain sizes of the joined interlayers. The calculations also revealed that the isothermal-solidification time becomes a weak function of the average Nb-grain size when the amount of Ni (or the liquid) retained in the joint is minimized (which was the case when a 2.4-MPa bonding pressure was used). Similar conclusions were drawn experimentally when fine-grained Nb core layers were joined to study the effects of core-layer microstructure on the Ni-concentration profiles. Although the concentrations were slightly more homogenized in the interlayers with the initially fine-grained Nb, the differences in the concentration profiles were minimal, suggesting that the effective decrease in the isothermal-solidification time was relatively small (in the order of minutes). Any increase in Ni-diffusion distance due to the initial finer core-layer grain structure during heating was essentially negligible and the only indication of increased diffusion rate was the higher Ni concentrations in the center of the interlayer ($>(3 \text{ to } 4)\sqrt{D_l t}$ from the interfaces), where grain-boundary diffusion was dominant. It appears that regardless of the core-layer microstructure, the current model can yield a reasonable estimate of the bonding times when thin TLP layers are retained in the joints.

5.1 Future Work

This study used the Ni/Nb/Ni interlayer system to better understand the interrelationships between processing conditions, interlayer microstructure, and materials properties. To promote the widespread use of TLP bonding in various ceramic systems, the Ni-Nb pair may be used as a model system to facilitate future interlayer designs. In contrast to interlayer systems used in previous studies, where the TLP layers were typically MPD-rich, both the Ni/Nb/Ni and Co/Nb/Co interlayers formed liquids that have high Nb content. The high Nb concentration in the TLP enables the interlayers to form relatively thick liquid layers that can fill wide interfacial gaps. The incorporation of Nb, which has a relatively high affinity for O, in the liquid improved wetting on the ceramic surfaces

compared to pure Ni liquid. Preliminary joining experiments using Ni/Mo/Ni interlayer showed that all joints failed at the interfaces, likely due to poor wetting on the Al_2O_3 surfaces.[144] Indeed, sessile-drop experiments of Ni-Mo liquid on SSA-999W Al_2O_3 resulted in a contact angle of ≈120° at 1400°C. While capillary flow considerations alone suggest that non-reactive liquids may be used in TLP bonding, the formation of TLP layers that wet the ceramic appears to be crucial in forming strong, flaw-free interfaces.

One way to improve the wetting behavior on ceramics is to use an active-metal addition in the interlayer. In active-metal brazing, Ti and Zr is typically used to promote wetting and adhesion between the braze and the ceramic, but typically results in the formation of brittle reaction layers. Previous studies have found, however, that optimum bond strengths can be obtained when only small amounts of reactive metals are used to limit the reaction-layer thickness. As discussed previously, in TLP bonding, a non-reactive liquid has a higher driving force to fill interfacial gaps than in conventional brazing because it is in contact with both the metallic core layer and the ceramic, as opposed to just being in contact with two ceramic surfaces. Therefore, either minute amounts of highly reactive metals, such as Ti and Zr, or larger amounts of less reactive metals, such as Nb, may be incorporated into the cladding layers. Ideally, the active-metal additions would lower the contact angle on the ceramic, then diffuse into the core layer before reacting with the ceramic. For instance, Ti forms complete solid solutions with refractory metals, such as Mo,[145] Ta,[146] and V.[147] The Ni-Ti phase diagram[126] shows that a eutectic liquid can form at 942°C. If a (Ti, Ni)/Mo/(Ti, Ni) interlayer was used to join Al_2O_3, the (Ti, Ni) cladding layers can form a liquid that wets the Al_2O_3. The liquid can then isothermally solidify as Ti and Ni diffuses into Mo before the Ti reacts with the Al_2O_3. A similar interlayer design consisting of (Nb, Ni) cladding layers has been proposed to join Al_2O_3.

This was also the first wetting study of high-Nb content liquid on Al_2O_3. No detectable NbO_x layers were found in the joined samples and sessile-drop samples, but the 50:50 Ni-Nb alloy still formed a contact angle significantly lower than typical non-reactive metals. Sessile-drop and drop-transfer experiments involving other refractory-metal-rich liquids, such as Ni-Mo and Ni-V are currently being conducted. Wetting behavior of ternary alloy liquids, such as Ti-Ni-Mo, and Ni-Nb-Mo, are also of interest in the standpoint of interlayer design.

The Ni-Nb and Co-Nb systems also benefitted from the high Ni and Co diffusivities in Nb, enabling rapid isothermal solidification. Under specific processing conditions, the current analytical calculation model can effectively predict isothermal-solidification times. However, there are several considerations that are currently lacking in the model presented in this work. These include effects of core-layer microstructure evolution on diffusion and prediction of the amount of liquid/MPD retained in the joints. Diffusion during heating is also difficult to predict because analytical solutions to diffusion along stationary and migrating grain boundaries are difficult to solve and phase-equilibrium relationships (e.g., solubility limits and intermetallic formation) change with temperature. Of these factors, the amount of MPD diffused in the core perhaps has the biggest impact on the isothermal-solidification time predictions. As shown in Figures 4.9 and 4.23, the isothermal-solidification time can vary from tens to, potentially, thousands of minutes when the overall Ni concentration increases by a few atomic %. Currently, another researcher in the group is conducting a separate study on developing more accurate methods of characterizing surface roughness, as well as its effects on the liquid redistribution during bonding. Once this method is established, it is trivial to include it in the analytical model from this study, since it does not fundamentally change the boundary conditions that may affect the solutions to Fick's equation.

The effects of microstructure are significantly more challenging to implement in the current model. As demonstrated experimentally, the initial Nb-core-layer microstructure appears to have some impact on diffusion rate, but at the bonding temperature used (1400°C) and the low Ni content, it appears that the change in the processing time with the core-layer microstructure is minimal. A series of joining experiments using a lower bonding pressure and core layers with varying microstructures may show greater differences in the Ni concentration profiles and the isothermal-solidification times. In cases where microstructural effects are expected to be significant (i.e., when relatively thick TLP layers form), an analytical model may no longer be sufficient to account for diffusion along both stationary and migrating grain boundaries. Numerical models can be used to simultaneously solve multiple equations to account for diffusion along different paths, but, as evidenced by previous efforts to model metal-metal TLP bonding, it remains difficult to execute because there are no mathematical solutions to describe grain-boundary diffusion in a bulk polycrystalline material.

Based on the characteristics of the Ni/Nb/Ni and Co/Nb/Co interlayers, a family of refractory interlayer systems ranging in chemical compositions and thermal expansion coefficients may be designed to join a wide range of ceramics. Wetting studies and diffusion-based processing-time calculations, in combination with phase diagrams and thermal-expansion-coefficient data, will be used to identify interlayer materials combinations, predict the mechanical behavior of the resulting joints, and the ideal bonding temperature, time, and pressure combinations.

References

1. Canonico DA, Cole NC, Slaughter GM. *Direct Brazing of Ceramics, Graphite, and Refractory-Metals*. Welding Journal, vol. 56, no. 8 (1977) p.31-8.
2. Naidich YV, Zhuravle VS, Kostyuk BD. *Brazing Alumina Ceramics for Seals Working at 1300°C*. Welding Production, vol. 17, no. 7 (1970) p.52-3.
3. Nicholas M. Joining Processes: Introduction to Brazing and Diffusion Bonding. Dordrecht, The Netherlands: Kluwer Academic Publishers; 1998
4. Iino Y. *Partial Transient Liquid-Phase Metals Layer Technique of Ceramic-Metal Bonding*. Journal of Materials Science Letters, vol. 10, no. 2 (1991) p.104-6.
5. Shalz ML, Dalgleish BJ, Tomsia AP, Glaeser AM. *Ceramic Joining: Part I Partial Transient Liquid-Phase Bonding of Alumina via Cu/Pt Interlayers*. Journal of Materials Science, vol. 28, no. 6 (1993) p.1673-84.
6. McDonald JE, Eberhart JG. *Adhesion in Aluminum Oxide-Metal Systems*. Transactions of the Metallurgical Society of AIME, vol. 233, no. 3 (1965) p.512-7.
7. Crispin RM, Nicholas MG. *The Wetting and Bonding Behavior of Some Nickel Alloy-Alumina Systems*. Journal of Materials Science, vol. 47, no. 15 (1976) p.4209-20.
8. Nicholas M. *The Strength of Metal/Alumina Interfaces*. Journal of Materials Science, vol. 3, no. 6 (1968) p.571-6.
9. Dalgleish BJ, Saiz E, Tomsia AP, Cannon RM, Ritchie RO. *Interface Formation and Strength in Ceramic-Metal Systems*. Scripta Metallurgica et Materialia, vol. 31, no. 8 (1994) p.1109-14.
10. Nicholas M, Forgan RRD, Poole DM. *The Adhesion of Metal/Alumina Interfaces*. Journal of Materials Science, vol. 3, no. 1 (1968) p.9-14.
11. Saiz E, Tomsia AP, Cannon RM. *Triple Line Ridging and Attachment in High-Temperature Wetting*. Scripta Materialia, vol. 44, no. 1 (2001) p.159-64.
12. Garandet JP, Drevet B, Eustathopoulos N. *On the Validity of Young's Equation in the Presence of Gravitational and Other External Force Fields*. Scripta Materialia, vol. 38, no. 9 (1998) p.1391-7.
13. Saiz E, Tomsia AP, Cannon RM. *Ridging Effects on Wetting and Spreading of Liquids on Solids*. Acta Materialia, vol. 46, no. 7 (1998) p.2349-61.
14. Eustathopoulos N, Nicholas M, Drevet B. Wettability at High Temperatures. Kidlington, UK: Elsevier Science Ltd.; 1999
15. Wenzel RN. *Resistance of Solid Surfaces to Wetting by Water*. Industrial and Engineering Chemistry, vol. 28 (1936) p.988-94.
16. Wenzel RN. *Surface Roughness and Contact Angle*. Journal of Physical and Colloid Chemistry, vol. 53, no. 9 (1949) p.1466-7.
17. Nakae H, Inui R, Hirata Y, Saito H. *Effects of Surface Roughness on Wettability*. Acta Materialia, vol. 46, no. 7 (1998) p.2313-8.
18. Wolansky G, Marmur A. *Apparent Contact Angles on Rough Surfaces: The Wenzel Equation Revisited*. Colloids and Surfaces A, vol. 156, no. (1999) p.381-8.
19. Cassie ABD, Baxter S. *Wettability of Porous Surfaces*. Transactions of the Faraday Society, vol. 40 (1944) p.546-50.
20. Shuttleworth R, Bailey GLJ. *The Spreading of a Liquid over a Rough Solid*. Discussions of the Faraday Society, vol. 3 (1948) p.16-22.

21. Nogi K, Oishi K, Ogino K. *Wettability of Solid Oxides by Liquid Pure Metals*. Materials Transactions, vol. 30, no. 2 (1989) p.137-45.
22. Wan C, Kritsalis P, Drevet B, Eustathopoulos N. *Optimization of Wettability and Adhesion in Reactive Nickel-Based Alloys/Alumina Systems by a Thermodynamic Approach*. Materials Science and Engineering A-Structural Materials Properties Microstructure and Processing, vol. 207, no. 2 (1996) p.181-7.
23. Xue XM, Sui ZT, Wang JT. *Effect of Zirconium on Wettability of Alumina and Zirconia by Silver-Indium Base Alloy*. Journal of Materials Science Letters, vol. 11, no. 22 (1992) p.1514-17.
24. Nicholas MG, Valentine TM, Waite MJ. *The Wetting of Alumina by Copper Alloyed with Titanium and Other Elements*. Journal of Materials Science, vol. 15, no. 9 (1980) p.2197-206.
25. Matsumoto H, Locatelli MR, Nakashima K, Glaeser AM, Mori K. *Wettability of Al_2O_3 by Liquid Cu as Influenced by Additives and Partial Transient Liquid-Phase Bonding of Al_2O_3*. Materials Transactions JIM, vol. 36, no. 4 (1995) p.555-64.
26. Zhang JX, Chandel RS, Seow HP. *A Study of Chromuim on Wettability of Liquid Copper on Alumina Ceramics*. International Journal of Modern Physics B, vol. 16, no. 1 & 2 (2002) p.50-6.
27. Nakashima K, Matsumoto H, Mori K. *Effect of Additional Elements Ni and Cr on Wetting Characteristics of Liquid Cu on Zirconia Ceramics*. Acta Materialia, vol. 48, no. 18-19 (2000) p.4677-81.
28. Kritsalis P, Merlin V, Coudurier L, Eustathopoulos N. *Effect of Cr on Interfacial Interaction and Wetting Mechanisms in Ni-Alloy Alumina Systems*. Acta Metallurgica et Materialia, vol. 40, no. 6 (1992) p.1167-75.
29. Eustathopoulos N, Drevet B. *Determination of the Nature of Metal-Oxide Interfacial Interactions from Sessile Drop Data*. Materials Science and Engineering A-Structural Materials Properties Microstructure and Processing, vol. 249, no. 1-2 (1998) p.176-83.
30. Mehrotra SP, Chaklader ACD. *Interfacial Phenomena between Molten Metals and Sapphire Substrate*. Metallurgical Transactions B-Process Metallurgy, vol. 16, no. 3 (1985) p.567-75.
31. Ownby PD, Liu J. *Surface Energy of Liquid Copper and Single Crystal Sapphire and the Wetting Behavior of Copper on Sapphire*. Journal of Adhesion Science and Technology, vol. 2, no. 4 (1988) p.255-69.
32. Ghetta V, Fouletier J, Chatain D. *Oxygen Adsorption Isotherms at the Surfaces of Liquid Cu and Au-Cu Alloys and Their Interfaces with Al_2O_3 Detected by Wetting Experiments*. Acta Materialia, vol. 44, no. 5 (1996) p.1927-36.
33. Beraud C, Courbiere M, Esnouf C, Juve D, Treheux D. *Study of Copper-Alumina Bonding*. Journal of Materials Science, vol. 24, no. 12 (1989) p.4545-54.
34. Espe W, Hix P, Kejhar J. *A High-Vacuum Tight Reliable Brazed Joint between Ceramic and Metal 2*. Vacuum, vol. 16, no. 2 (1966) p.61-5.
35. Espe W, Hix P, Kejhar J. *A High-Vacuum Tight Reliable Brazed Joint between Ceramic and Metal I*. Vacuum, vol. 16, no. 1 (1966) p.1-8.
36. Hammond JP, David SA, Santella ML. *Brazing Ceramic Oxides to Metals at Low-Temperatures*. Welding Journal, vol. 67, no. 10 (1988) p.S227-S32.
37. Mizuhara H, Mally K. *Ceramic-to-Metal Joining with Active Brazing Filler Metal*. Welding Journal, vol. 64, no. 10 (1985) p.27-32.

38. Elssner G, Petzow G. *Metal Ceramic Joining*. ISIJ International, vol. 30, no. 12 (1990) p.1011-32.
39. Hosking FM, Cadden CH, Yang NYC, et al. *Microstructural and Mechanical Characterization of Actively Brazed Alumina Tensile Specimens*. Welding Journal, vol. 79, no. 8 (2000) p.222S-30S.
40. Loehman RE, Tomsia AP. *Joining of Ceramics*. Ceramic Bulletin, vol. 67, no. 2 (1988) p.375-80.
41. Moorhead AJ. *Direct Brazing of Alumina Ceramics*. Advanced Ceramic Materials, vol. 2, no. 2 (1987) p.159-66.
42. Loehman RE, Tomsia AP. *Wetting and Joining of Mullite Ceramics by Active-Metal Braze Alloys*. Journal of the American Ceramic Society, vol. 77, no. 1 (1994) p.271-4.
43. Standing R, Nicholas M. *Wetting of Alumina and Vitreous Carbon by Copper-Tin-Titanium Alloys*. Journal of Materials Science, vol. 13, no. 7 (1978) p.1509-14.
44. Gremillard L, Saiz E, Chevalier J, Tomsia AP. *Wetting and Strength in the Tin-Silver-Titanium/Sapphire System*. International Journal of Materials Research and Advanced Techniques, vol. 95, no. 4 (2004) p.261-5.
45. Hao HQ, Jin ZH, Wang XT. *The Influence of Brazing Conditions on Joint Strength in Al_2O_3/Al_2O_3 Bonding*. Journal of Materials Science, vol. 29, no. 19 (1994) p.5041-6.
46. Kapoor RR, Eagar TW. *Brazing Alloy Design for Metal/Ceramic Joints*. Proceedings of the International Forum on Structural Ceramics Joining. Pittsburgh, PA: The American Ceramic Society, Inc., vol. 10 (1987) p. 1613-30.
47. Ning HL, Geng ZT, Ma JS, Huang FX, Qian ZY, Han ZD. *Joining of Sapphire and Hot Pressed Al_2O_3 Using Ag70.5-Cu27.5-Ti2 Brazing Filler Metal*. Ceramics International, vol. 29, no. 6 (2003) p.689-94.
48. Nicholas M. *Active Metal Brazing*. In: Nicholas M (ed). Joining of Ceramics. New York, NY: Chapman and Hall, 1990 p. 73-92.
49. Mizuhara H, Huebel E, Oyama T. *High Reliability Joining of Ceramic to Metal*. American Ceramic Society Bulletin, vol. 68, no. 9 (1989) p.1591-9.
50. Iseki T, Nicholas MG. *Elevated-Temperature Strengths of Alumina-Aluminum and Magnesium-Aluminum Samples*. Journal of Materials Science, vol. 14, no. 3 (1979) p.687-92.
51. Suganuma K, Okamoto T, Koizumi M, Kamachi K. *Influence of Shape and Size on Residual-Stress in Ceramic Metal Joining*. Journal of Materials Science, vol. 22, no. 10 (1987) p.3561-5.
52. Gibbesch B, Elssner G. *Ultra High Vacuum Diffusion Bonded Nb-Al_2O_3 and Cu-Al_2O_3 Joints-the Role of Welding Temperature and Sputter Cleaning*. Acta Metallurgica et Materialia, vol. 40, no. supplement issue (1992) p.S59-66.
53. Bailey FP, Black KJT. *Effect of Ambient Atmosphere on Gold-to-Alumina Solid-State Reaction Bond*. Journal of Materials Science, vol. 13, no. 7 (1978) p.1606-8.
54. Bailey FP, Black KJT. *Gold-to-Alumina Solid-State Reaction Bonding*. Journal of Materials Science, vol. 13, no. 5 (1978) p.1045-52.
55. Allen RV, Borbidge WE. *Solid-State Metal Ceramic Bonding of Platinum to Alumina*. Journal of Materials Science, vol. 18, no. 9 (1983) p.2835-43.
56. Serier B, Berroug A, Juve D, Treheux D, Moya EG. *Silver Alumina Solid-State Bonding – Study of Diffusion and Toughness Close to the Interface*. Journal of the European Ceramic Society, vol. 12, no. 5 (1993) p.385-90.

57. Serier B, Bouiadjra BB, Treheux D. *Mechanism of Adhesion at Solid State Bonding Ceramic-Metal: Case of Silver-Alumina Couple*. Euro Ceramics VIII, Pts 1-3. Volume 264-268. Zurich-Uetikon: Trans Tech Publications LTD., 2004 p. 667-70.
58. Nicholas MG, Crispin RM. *Diffusion Bonding Ceramics with Ductile Interlayers*. In: Taylor D (ed). Science of Ceramics 14 Inst Ceramics. Stoke-on-Trent, UK, (1988) p. 539-44.
59. Derby B. *Diffusion Bonding*. In: Nicholas M (ed). Joining of Ceramics. New York, NY: Chapman and Hall, 1990 p. 94-110.
60. Klomp JT, Vandeven AJC. *Parameters in Solid-State Bonding of Metals to Oxide Materials and the Adherence of Bonds*. Journal of Materials Science, vol. 15, no. 10 (1980) p.2483-8.
61. Hamilton CH. *Pressure Requirements for Diffusion Bonding Titanium*. In: Jaffee RI, Burte HM (eds). Titanium Science and Technology. Cambridge, MA: Plenum Press, vol. 1 (1972) p. 625-48.
62. Garmong G, Paton NE, Argon AS. *Attainment of Full Interfacial Contact During Diffusion Bonding*. Metallurgical Transactions A-Physical Metallurgy and Materials Science, vol. 6, no. 6 (1975) p.1269-79.
63. Derby B, Wallach ER. *Theoretical-Model for Diffusion Bonding*. Metal Science, vol. 16, no. 1 (1982) p.49-56.
64. Derby B, Wallach ER. *Diffusion Bonding - Development of Theoretical Model*. Metal Science, vol. 18, no. 9 (1984) p.427-31.
65. Reimanis IE. *Pore Removal During Diffusion Bonding of Nb-Al_2O_3 Interfaces*. Acta Metallurgica, vol. 40, no. S1 (1992) p.S67-S74.
66. Nicholas MG, Crispin RM. *Diffusion Bonding Stainless-Steel to Alumina Using Aluminum Interlayers*. Journal of Materials Science, vol. 17, no. 11 (1982) p.3347-60.
67. Das S, Tiwari AN, Kulkarni AR. *Thermo-Compression Bonding of Alumina Ceramics to Metal*. Journal of Materials Science, vol. 39, no. 10 (2004) p.3345-55.
68. Urena A, Gomez de Salazar JM, Quinones J. *Diffusion Bonding of Alumina to Steel Using Soft Copper Interlayer*. Journal of Materials Science, vol. 27, no. 3 (1992) p.599-606.
69. Wang HF, Gerberich WW, Angelo JE. *Interfacial Reactions and Adhesion Strength of Metal/Ceramic Composites*. Journal of Materials Research, vol. 10, no. 9 (1995) p.2367-73.
70. Travessa D, Ferrante M. *The Al_2O_3-Titanium Adhesion in the View of the Diffusion Bonding Process*. Journal of Materials Science, vol. 37, no. 20 (2002) p.4385-90.
71. Zalar A, Baretzky BMM, Hofmann S, Rühle M, Panjan P. *Interfacial Reactions in Al_2O_3/Ti, Al_2O_3/Ti_3Al and Al_2O_3/TiAl Bilayers*. Thin Solid Films, vol. 352, no. 1-2 (1999) p.151-5.
72. Kliauga AM, Ferrante M. *Interface Compounds Formed During the Diffusion Bonding of Al_2O_3 to Ti*. Journal of Materials Science, vol. 35, no. 17 (2000) p.4243-9.
73. Gibbesch B, Elssner G, Petzow G. *Investigation of Ti/ Al_2O_3 Joints with Intermediate Tantalum and Niobium Layers*. Biomaterials, vol. 13, no. 7 (1992) p.455-61.
74. Yoshino Y, Shibata T. *Structure and Bond Strength of a Copper-Alumina Interface*. Journal of the American Ceramic Society, vol. 75, no. 10 (1992) p.2756-60.
75. Gubbels GHM, Heikinheimo LSK, Klomp JT. *A Comparison between Titanium Alumina Diffusion Bonding and Titanium Active Brazing*. Zeitschrift Fur Metallkunde, vol. 85, no. 12 (1994) p.828-32.
76. Joy T. *Ceramic-Metal Diffusion Bonding – a Case History*. In: Nicholas M (ed). Joining of Ceramics. New York, NY: Chapman and Hall, 1990 p. 194-211.

77. Gale WF, Butts DA. *Transient Liquid Phase Bonding*. Science and Technology of Welding and Joining, vol. 9, no. 4 (2004) p.283-300.
78. Macdonald WD, Eagar TW. *Transient Liquid-Phase Bonding*. Annual Review of Materials Science, vol. 22, no. (1992) p.23-46.
79. Tuah-Poku I, Dollar M, Massalski TB. *A Study of the Transient Liquid Phase Bonding Process Applied to a Ag/Cu/Ag Sandwich Joint*. Metallurgical Transactions A (Physical Metallurgy and Materials Science), vol. 19A, no. 3 (1988) p.675-86.
80. Lynch JF, Feinstein L, Huggins RA. *Brazing by Diffusion-Controlled Formation of Liquid Intermediate Phase*. Welding Journal, vol. 38, no. 2 (1959) p.85-9.
81. Tiner NA. *Metallurgical Aspects of Silver Brazing Titanium*. Welding Journal, vol. 34, no. 11 (1955) p.846-50.
82. Wu KC. *Resistance NOR-Ti-Bond Joining of Titanium Shapes*. Welding Journal, vol. 50, no. 9 (1971) p.S386-S93.
83. Wells RR. *Microstructural Control of Thin-Film Diffusion-Brazed Titanium*. Welding Journal, vol. 55, no. 1 (1976) p.S20-S7.
84. Ikawa H, Shin S, Nakao Y. *Weldability of Nickel-Base Heat Resisting Superalloy. Improvement of Hot Cracking Sensitivity of Inconel 713C and Its Mechanical Properties*. Technology Reports of the Osaka University, vol. 21, no. S995-S1026 (1971) p.461-74.
85. Ikawa H, Shin S, Nakao Y. *Weldability of Nickel-Base Heat Resisting Superalloy. Main Cause of Weld Crackings in Heat Affected Zone of Inconel 713C*. Technology Reports of the Osaka University, vol. 21, no. 973-994 (1971) p.101-20.
86. Duvall DS, Owczarsk.Wa, Paulonis DF. *TLP Bonding - New Method for Joining Heat-Resistant Alloys*. Welding Journal, vol. 53, no. 4 (1974) p.203-14.
87. Ikawa H, Nakao Y, Isai T. *Transient Liquid Phase (TLP) Diffusion Bonding of Nickel-Base Heat Resisting Alloys*. Technology Reports of the Osaka University, vol. 27, no. 1337-1363 (1977) p.121-8.
88. Gale WF, Wallach ER. *Microstructural Development in Transient Liquid-Phase Bonding*. Metallurgical Transactions A (Physical Metallurgy and Materials Science), vol. 22A, no. 10 (1991) p.2451-7.
89. Gale WF, Orel SV. *Microstructural Development in NiAl/Ni-Si-B/Ni Transient Liquid Phase Bonds*. Metallurgical and Materials Transactions A-Physical Metallurgy and Materials Science, vol. 27, no. 7 (1996) p.1925-31.
90. Gale WF, Guan Y. *Transient Liquid-Phase Bonding in the NiAl/Cu/Ni System - A Microstructural Investigation*. Metallurgical and Materials Transactions A-Physical Metallurgy and Materials Science, vol. 27, no. 11 (1996) p.3621-9.
91. Gale WF, Orel SV. *A Microstructural Investigation of NiAl/Ni-Si-B/NiAl Transient Liquid Phase Bonds*. Journal of Materials Science, vol. 31, no. 2 (1996) p.345-9.
92. Gale WF, Guan Y. *Microstructure and Mechanical Properties of Transient Liquid Phase Bonds between NiAl and a Nickel-Base Superalloy*. Journal of Materials Science, vol. 34, no. 5 (1999) p.1061-71.
93. Johnson R. *The Use of TETIG Diagrams in High-Temperature Brazing*. Welding Journal, vol. 60, no. 10 (1981) p.S185-S93.
94. Gale WF, Guan Y. *Wide Gap Transient Liquid Phase Bonding of NiAl-Hf to a Nickel Base Superalloy*. Materials Science & Technology, vol. 15, no. 4 (1999) p.464-7.

95. Kwon YS, Kim JS, Moon JS, Suk MJ. *Transient Liquid Phase Bonding Process Using Liquid Phase Sintered Alloy as an Interlayer Material.* Journal of Materials Science, vol. 35, no. 8 (2000) p.1917-24.
96. Zhou T, Gale WF. *Modeling Wide Gap TLP Bonding of Ti-48 at.% Al-2 at.% Cr-2 at.% Nb Alloys.* Materials Science and Technology, vol. 19, no. 8 (2003) p.1084-90.
97. Gale WF, Xu Y, Wen X, Abdo ZAM. *Wide-Gap Transient Liquid-Phase Bonding of Ti-48 at.% Al-2 at.% Cr-2 at.% Nb.* Metallurgical and Materials Transactions A-Physical Metallurgy and Materials Science, vol. 30, no. 10 (1999) p.2723-6.
98. Niemann JT, Garrett RA. *Eutectic Bonding of Boron-Aluminum Structural Components. 1. Evaluation of Critical Processing Parameters.* Welding Journal, vol. 53, no. 4 (1974) p.S175-S84.
99. MacDonald WD, Eagar TW. *Isothermal Solidification Kinetics of Diffusion Brazing.* Metallurgical and Materials Transactions A-Physical Metallurgy and Materials Science, vol. 29, no. 1 (1998) p.315-25.
100. Ikawa H, Nakao Y, Isai T. *Theoretical Considerations on the Metallurgical Process in T.L.P. Bonding of Nickel-Base Superalloys.* Transactions of the Japan Welding Society, vol. 10, no. 1 (1979) p.24-9.
101. Nakao Y, Nishimoto K, Shinozaki K, Kang C. *Theoretical Research on Transient Liquid Insert Metal Diffusion Bonding of Nickel Base Alloys.* Transactions of the Japan Welding Society, vol. 20, no. 1 (1989) p.60-5.
102. Mullins WW. *Theory of Thermal Grooving.* Journal of Applied Physics, vol. 28, no. 3 (1957) p.333-9.
103. Zhou Y, Gale WF, North TH. *Modelling of Transient Liquid Phase Bonding.* International Materials Reviews, vol. 40, no. 5 (1995) p.181-96.
104. Kokawa H, Lee CH, North TH. *Effect of Grain-Boundaries on Isothermal Solidification During Transient Liquid-Phase Brazing.* Metallurgical Transactions A-Physical Metallurgy and Materials Science, vol. 22, no. 7 (1991) p.1627-31.
105. Saida K, Zhou Y, North TH. *The Influence of Base-Metal Grain-Size on Isothermal Solidification During Transient Liquid-Phase Brazing of Nickel.* Journal of Materials Science, vol. 28, no. 23 (1993) p.6427-32.
106. Mishin Y, Herzig C, Bernardini J, Gust W. *Grain Boundary Diffusion: Fundamentals to Recent Developments.* International Materials Reviews, vol. 42, no. 4 (1997) p.155-78.
107. Mishin YM, Razumovskii IM. *A Model for Diffusion Along a Moving Grain Boundary.* Acta Metallurgica et Materialia, vol. 40, no. 4 (1992) p.839-45.
108. Zhou YH, North TH. *Numerical Model for the Effect of Grain Boundaries on the Total Amount Diffused.* Acta Metallurgica et Materialia, vol. 42, no. 3 (1994) p.1025-9.
109. Smidoda K, Gottschalk W, Gleiter H. *Diffusion in Migrating Interfaces.* Acta Metallurgica, vol. 26, no. 12 (1978) p.1833-6.
110. Olander DR, El-Saied UM. *The Effect of Grain-Boundary Motion on the Kinetics of Solute Penetration into a Polycrystalline Medium.* Acta Metallurgica et Materialia, vol. 40, no. 6 (1992) p.1329-36.
111. Ikeuchi K, Zhou Y, Kokawa H, North TH. *Liquid-Solid Interface Migration at Grain-Boundary Regions During Transient Liquid-Phase Brazing.* Metallurgical Transactions A-Physical Metallurgy and Materials Science, vol. 23, no. 10 (1992) p.2905-15.

112. Harrison LG. *Influence of Dislocations on Diffusion Kinetics in Solids with Particular Reference to Alkali Halides*. Transactions of the Faraday Society, vol. 57, no. 8 (1961) p.1191-9.
113. Cahn JW, Balluffi RW. *Diffusional Mass-Transport in Polycrystals Containing Stationary or Migrating Grain-Boundaries*. Scripta Metallurgica, vol. 13, no. 6 (1979) p.499-502.
114. Zhou YH, North TH. *Process Modeling and Optimized Parameter Selection During Transient Liquid Phase Bonding*. Zeitschrift Für Metallkunde, vol. 85, no. 11 (1994) p.775-80.
115. Shalz ML, Dalgleish BJ, Tomsia AP, Glaeser AM. *Ceramic Joining II. Partial Transient Liquid-Phase Bonding of Alumina Via Cu/Ni/Cu Multilayer Interlayers*. Journal of Materials Science, vol. 29, no. 12 (1994) p.3200-8.
116. Saiz E, Cannon RM, Tomsia AP. *High-Temperature Wetting and the Work of Adhesion in Metal/Oxide Systems*. Annual Review of Materials Research, vol. 38, (2008) p.197-226.
117. Hong SM. Effects of Processing Conditions on the Interlayer Microstructure and Fracture Strengths in Reduced-Temperature Transient-Liquid-Phase Bonding of Alumina [M.S.]. Berkeley, CA: University of California, Berkeley, 2006
118. Iino Y, Taguchi N. *Interdiffusion Metals Layer Technique of Ceramic-Metal Bonding*. Journal of Materials Science Letters, vol. 7, no. 9 (1988) p.981-2.
119. Marks RA, Sugar JD, Glaeser AM. *Ceramic Joining. IV. Effects of Processing Conditions on the Properties of Alumina Joined Via Cu/Nb/Cu Interlayers*. Journal of Materials Science, vol. 36, no. 23 (2001) p.5609-24.
120. Shalz ML, Dalgleish BJ, Tomsia AP, Cannon RM, Glaeser AM. *Ceramic Joining III Bonding of Alumina via Cu/Nb/Cu Interlayers*. Journal of Materials Science, vol. 29, no. 14 (1994) p.3678-90.
121. Kruzic JJ, Marks RA, Yoshiya M, Glaeser AM, Cannon RM, Ritchie RO. *Fracture and Fatigue Behavior at Ambient and Elevated Temperatures of Alumina Bonded with Copper/Niobium/Copper Interlayers*. Journal of the American Ceramic Society, vol. 85, no. 10 (2002) p.2531-41.
122. Esposito L, Bellosi A, Guicciardi S, De Portu G. *Solid State Bonding of Al_2O_3 with Cu, Ni and Fe: Characteristics and Properties*. Journal of Materials Science, vol. 33, no. 7 (1998) p.1827-36.
123. *Nb-Ni Phase Diagram*. In: Massalski TB (ed). Binary Alloy Phase Diagrams. Volume 3: ASM International, 1990 p. 2746-7.
124. *Co-Nb Phase Diagram*. In: Massalski TB (ed). Binary Alloy Phase Diagrams. Volume 2: ASM International, 1990 p. 1211-2.
125. Locatelli MR, Tomsia AP, Nakashima K, Dalgleish BJ, Glaeser AM. *New Strategies for Joining Ceramics for High-Temperature Applications*. Mechanical & Corrosion Properties, Series A. Switzerland: Trans Tech Publications, vol. 111-112 (1995) p. 157-90.
126. *Ni-Ti Phase Diagram*. In: Massalski TB (ed). Binary Alloy Phase Diagrams. Volume 3: ASM International, 1990 p. 2874-6.
127. Hong SM, Glaeser AM. *Reduced-Temperature Transient-Liquid-Phase Bonding of Alumina Using a Ag-Cu–Based Brazing Alloy*. In: Stephens JJ, Weil KS (eds). The 3rd International Brazing and Soldering Conference. San Antonio, TX: ASM International, vol. 2006) p. 181-8.
128. *Cu-Ni Phase Diagram*. In: Massalski TB (ed). Binary Alloy Phase Diagrams. Volume 2: ASM International, 1990 p. 1442-6.

129. Dalgleish BJ, Tomsia AP, Nakashima K, Locatelli MR, Glaeser AM. *Low Temperature Routes to Joining Ceramics for High-Temperature Applications*. Scripta Metallurgica et Materialia, vol. 31, no. 8 (1994) p.1043-8.
130. Voytovych R, Robaut F, Eustathopoulos N. *The Relation between Wetting and Interfacial Chemistry in the CuAgTi/Alumina System*. Acta Materialia, vol. 54, no. 8 (2006) p.2205-14.
131. Ceccone G, Nicholas MG, Peteves SD, Tomsia AP, Dalgleish BJ, Glaeser AM. *An Evaluation of the Partial Transient Liquid Phase Bonding of Si_3N_4 Using Au Coated Ni-22Cr Foils*. Acta Materialia, vol. 44, no. 2 (1996) p.657-67.
132. Wang K, Reeber RR. *The Role of Defects on Thermophysical Properties: Thermal Expansion of V, Nb, Ta, Mo and W*. Materials Science & Engineering R-Reports, vol. 23, no. 3 (1998) p.101-37.
133. Ablitzer D. *Diffusion of Niobium, Iron, Cobalt, Nickel, and Copper in Niobium*. Philosophical Magazine, vol. 35, no. 5 (1977) p.1239-56.
134. Razumovskii IM, Mishin Y, Herzig C. *Investigation of Ni-63 Diffusion Along Stationary and Moving Grain Boundaries in Nb*. Materials Science and Engineering A-Structural Materials Properties Microstructure and Processing, vol. 212, no. 1 (1996) p.45-50.
135. Crank J. *The Mathematics of Diffusion*. London, England: Oxford University Press, 1975 p. 62-4.
136. Hillert M, Purdy GR. *Chemically Induced Grain Boundary Migration*. Acta Metallurgica, vol. 26, no. 2 (1978) p.333-40.
137. Eustathopoulos N, Coudurier L. *Influence of Alloying Elements on Wettability and Adhesion in Liquid Metal-Ceramic Systems*. Abstracts of Papers of the American Chemical Society, vol. 203, no. (1992) p.1011-22.
138. Nakashima K, Takihira K, Mori K, Shinozaki N. *Wettability of Al_2O_3 Substrate by Liquid Iron - Effects of Oxygen in Liquid Iron and Purity of Al_2O_3 Substrate*. Materials Transactions JIM, vol. 33, no. 10 (1992) p.918-26.
139. Selvadura G. Ellingham Diagram Web Project (http://www.engr.sjsu.edu/ellingham/) Accessed 2009.
140. Levi G, Scheu C, Kaplan WD. *Segregation of Aluminium at Nickel-Sapphire Interfaces*. Kluwer Academic Publishing (2001) p. 213-20.
141. Chase MW. JANAF Thermochemical Tables, 1975 Supplement. Volume 4. Washington, D.C.: American Chemical Society and the American Institute of Physics for the National Bureau of Standards; 1975
142. Evans JW, Dejonghe LC. The Production of Inorganic Materials. New York, NY: Macmillan Publishing Co.; 1992
143. Whipple RTP. *Concentration Contours in Grain Boundary Diffusion*. Philosophical Magazine, vol. 45, no. 371 (1954) p.1225-36.
144. Reynolds TB. Transient Liquid Phase Bonding Using Ni/Mo/Ni Interlayer (Unpublished Work). University of California, Berkeley, 2009.
145. *Mo-Ti Phase Diagram*. In: Massalski TB (ed). Binary Alloy Phase Diagrams. Volume 3: ASM International, 1990 p. 2675-9.
146. *Ta-Ti Phase Diagram*. In: Massalski TB (ed). Binary Alloy Phase Diagrams. Volume 3: ASM International, 1990 p. 3430-3.

147. *Ti-V Phase Diagram*. In: Massalski TB (ed). Binary Alloy Phase Diagrams. Volume 3: ASM International, 1990 p. 3494-5.